MID INFRARED LHS SYSTEM PACKAGING USING FLEXIBLE WAVEGUIDES

FINAL REPORT

GRANT NO. NAG-1-407

PERIOD: OCTOBER 1, 1984 - AUGUST 15, 1987

TO

NASA LANGLEY RESEARCH CENTER
HAMPTON, VIRGINIA

SUBMITTED BY

DR. CHUNG YU

ELECTRICAL ENGINEERING DEPARTMENT

NORTH CAROLINA A & T STATE UNIVERSITY

GREENSBORO, NC 27411

PUBLICATIONS

1. C. Yu, and A. Niczad, "Field Enhancement and Increased Island Array Selectivity of the Discontinuous MIM Film Diode", Proc. 10th Intern. Conf. On Infrared and MM Waves, Lake Buena Vista, Florida (Dec. 1985), p. 135.

2. C. Yu, M. Hemmatian, and A. Yekrangian, "Mounting Improvements of the MOM Point Contact Diode", Proc. 10th Intern. Conf. on Infrared and MM Waves, Lake Buena Vista, Florida (Dec. 1985) p. 133.

3. C. Yu, M. A. Hemmatian, A. Niczad, Y. Taghipoor, and A.Yekrangian, "A Systematic Study of the Effect of Hooking Upon Contact on the Performance of Electrolytically Etched Point Contact MOM Diodes", Proc. SPIE 544, 78 (1985).

4. C. Yu, and A. Sabzali, "Guided Transmission for 10 μm Tunable Lasers", Proc. SPIE 717, 33 (1986).

5. C. Yu, and C. K. Fong, "Investigation of Stimulated Brillouin Scattering Switching in Mid IR Fibers", Proc. SPIE's O-E/Fibers'87, Symp. on Fiber Optics and Integrated Optoelectronics, San Diego, CA (Aug. 16-21, 1987).

6. C. Yu, and C. S. Tan, "Responsivity and Noise Properties of a Highly Stabilized MOM Point Contact Diode for High Power Mid IR Detection and Mixing", Accepted for presentation at the 10th Intern. Conf. on Lasers'87, Lake Tahoe, Nevada (Dec. 7-11, 1987).

7. C. Yu, and C. K. Fong, "Study of Nonlinear Optical Phenomena in Mid IR Fibers",, Accepted for presentation at the 10th Intern. Conf. on Lasers'87, Lake Tahoe, Nevada (Dec. 7-11, 1987).

8. C. Yu, C. K. Fong, and C. S. Tan, "Phonon Probe for Laser Propagation Studies in Mid IR Fibers", accepted for presentation at the 12th Intern. Conf. on Infrared and MM Waves, Orlando, Florida (Dec. 14-18, 1987).

GRADUATE STUDENTS SUPPORTED BY NAG-1-407

1. Alvernon Walker - MSEE August 1986
2. Clinton Lee - MSEE 1983 - in NCSU Ph. D. degree program
3. Donna Warren - BSEE
4. Samuel Bethea - BSEE
5. Alvin Pettiford - MSEE in progress
6. Michael Smith - MSEE Summer 1986 - in Ph. D. degree program at Univ. Of Iowa
7. Francis Flores - MSEE in progress
8. Ali Yekrangian - MSEE 1986
9. C. K. Fong - MSEE expected,December 1987

GRADUATE STUDENTS NOT FINANCIALLY SUPPORTED BY GRANT, BUT SUPPORTED BY ACQUIRED RESEARCH FACILITIES

1. A. Sabzali - MSEE June 1987
2. M. Hemmatian - MSEE in progress
3. A. Niczad - MSEE October 1986
4. C. S. Tan - MSEE in progress
5. Y. C. Chong - MSEE in progress
6. M. J. Barzgari - MSEE in progress

SUMMARY

As mid IR fiber optic systems are rapidly approaching a reality, so is the feasibility of fiber optic laser heterodyne systems. Laser heterodyne spectroscopy for high resolution monitoring of atmospheric gaseous pollutants is necessarily in the mid IR, the region in which the absorption signature of gaseous species is most prominent. It so happens that the lowest theoretical loss due to Rayleigh-Brillouin scattering also lies in the mid IR. Prospects of highly efficient laser heterodyne systems are thus very good.

Such fibers are now beginning to be commercially available, and we are in the midst of a test program of such fibers with ambient temperature ranging from cryogenic to above room, and stringest mechanical flexibility requirements. Preliminary results are encouraging. We are now launching into a program of exploring possible mid IR fiber optic device applications, by taking advantage of this phonon rich region. The potential long interaction length in fibers coupled with predicted extremely low losses point to stimulated Brillouin scattering based devices in the mW range. The generation of back-scattered sBs at low laser powers is significant not only as an ultimate power limiting factor for laser transmission in fibers in the mid IR, but also the presence of frequency-shifted multiple order sBs Stokes and antiStokes lines will certainly have severe effect on the laser beats crucial in high resolution heterodyne spectroscopy. The capability of phase conjugation by sBs and the existence of a threshold can serve as the basis for wavefront reconstruction and optical switching.

TABLE OF CONTENTS

LIST OF TABLES

LIST OF FIGURES

CHAPTER ONE

INTRODUCTION

Infrared optical systems have found special applications that utilize the unique characteristics of this region of the spectrum. Thus, coherent or heterodyne laser systems have been in use in the field of high resolution spectroscopy in the monitoring of atmospheric and automobile exhaust gaseous pollutants; such systems are also installed as airborn laser scanning systems that require visibility under adverse weather conditions, such as fog, haze, moderate rain, smoke and dust; endoscopic laser treatment and laser surgery delivery systems, these major areas of application increasingly call upon high level of system mobility, greatly enhanced mechanical flexibility and adaptability, stability and reliability. Current systems normally incorporate IR transmissive and reflective optics such as lenses and mirrors shown in Figure 1-1 which are bulky, costly and easily disturbed by environmental factors. These systems lack flexibility, stability, reliability and portability. IR systems must therefore duplicate those in the visible through system integration and compaction. Figure 1-2 shows the laser integration system requirements.

Portability calls for donw scaling of system size through miniturization of the source, detector and the guiding medium simultaneously for component dimensional compatibility. The

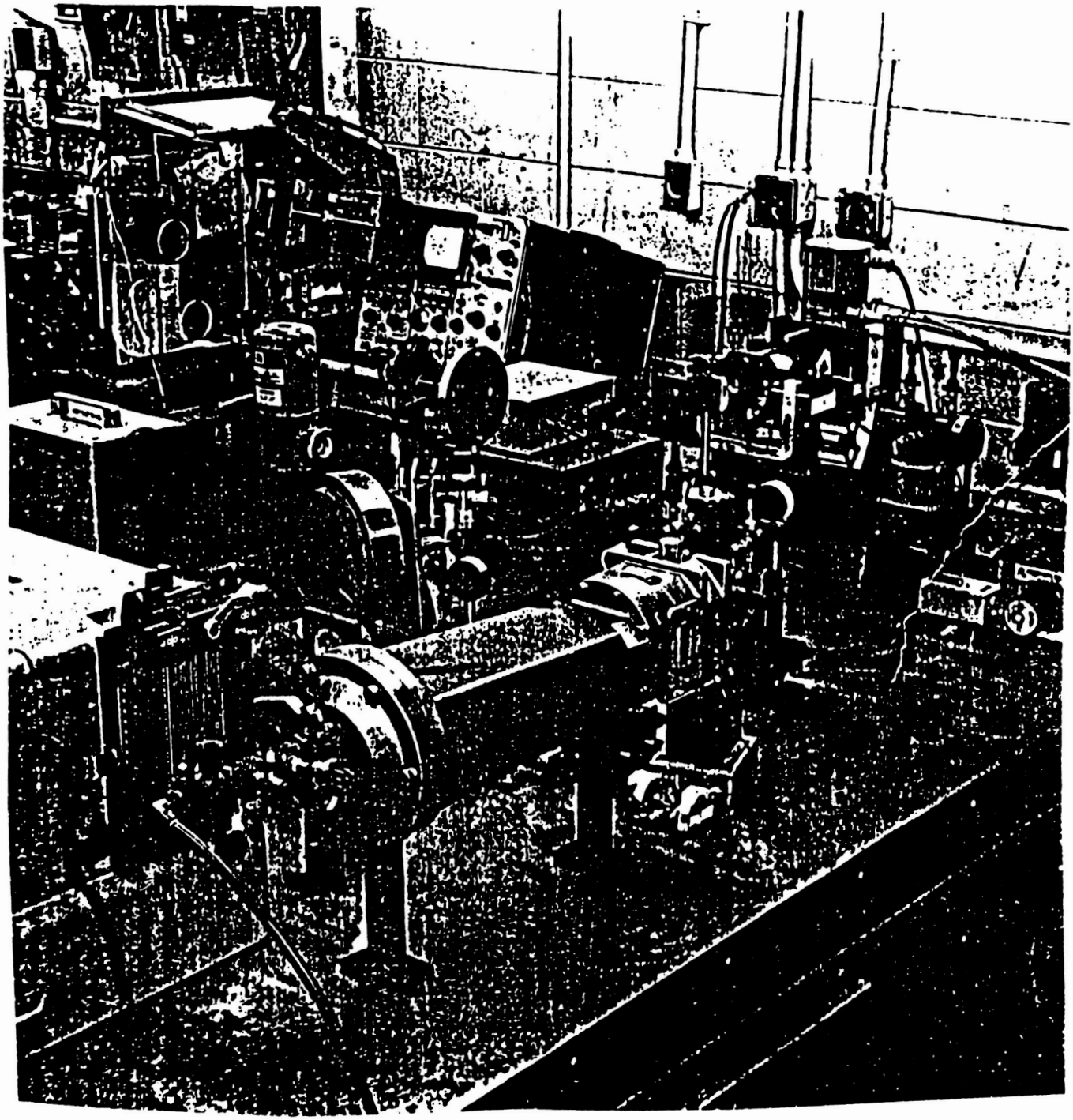

Figure 1-1. TDL and Conventional Optical Components for Beam Guiding.

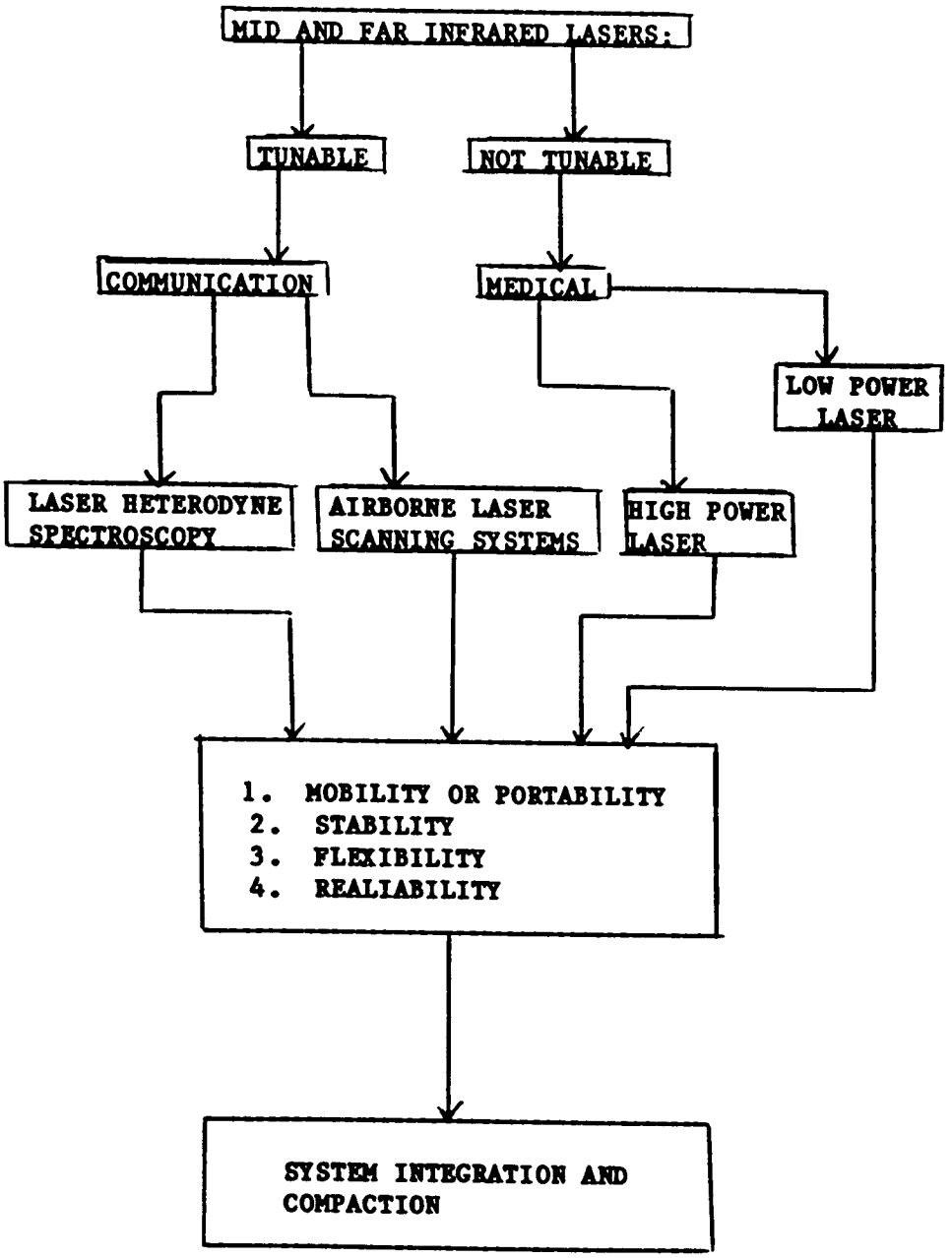

Figure 1-2. Laser Integration System requirements.

development of lead salt diode lasers as alternative and complementary sources to CO and CO_2 lasers is an important technological advance in the ultimate integration and compaction of mid and far infrared communication links. Advances in HgCdTe and metal-oxide-metal (MOM) thin film detectors lend high speed to these systems. The broadening market has brought about portable high-power CO and Co_2 lasers (Appendix A). The guiding media of hollow metallic pipes and fibers are maturing at a frantic pace, leading to rapidly decreasing fiber attenuation with anticipated figures in the Rayleigh scatteing limit of 0.01 dB/Km. The introduction of such guiding media will eliminate conventional lenses and mirrors and similar accessories, resulting in totally integrated and compacted infrared optoelectronic systems.

The idea of IR system integration and compaction via the fiber guiding medium was conceived by us in the late seventies [1]. However, due to the lack of IR fibers at that time, one of the alternatives was extending the microwave technique by using small, hollow metallic waveguides to gain flexibility. Even at present, such metallic piping is competitive with IR fibers in numerous system characteristics. The room temperature MOM diodes [2] being developed by us and HgCdTe detector that also operate at room temperature and being developed by the manufacturers (Appendix B) have the advantage of the elimination of the dreaded cryogenic enviornment, that is required by other types of detectors. Such an environment is a significant obstacle to system integration and compaction.

Figure 1-3 shows the integrated system package. This system consists of either CO_2 laser + metallic piping or fiber and detector systrem or a TDL + fiber and detector system.

The CO_2 + metallic piping and detector system are very important in medical use, where the CO_2 laser is used for burning tissues of human bodies and recently used to remove brain tumors in surgical operations. The latest non-toxic flexible CO_2 laser beam guide with metal and polymer hollow tube which provides validity and safety for CO_2 laser beam were developed by Kubo and Hashishin [3] is shown in Figure 1-4. The CO_2 laser beam through this guide is focused by using a cylindrical lens and convex lens, perhaps Zinc Selenide is desirable for infrared applications.

The TDL + fiber and detector combination performs an excellent communication system, where this package performs the complete requirements for such a field due to the tremendous advances in IR fiber optics and systems technology, where single mode fibers are of interest. Currently available room temperature detectors in the market also eliminate the dreaded cryogenic environment which is a great disadvantage in the field of communication.

In addition to laser heterodyning scanning this integrated system can be used as a standard set up for testing infrared fibers. Since such laser diodes can provide source areas of 25 microns diameter or less and are inherently high speed devices with very high photometric accuracies, fiber parameters such as dispersion and attenuation can be easily measured using these sources.

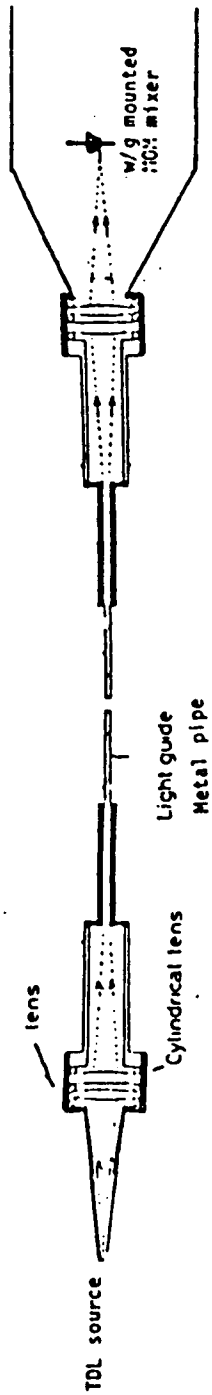

Figure 1-3. laser Integration System Requirements

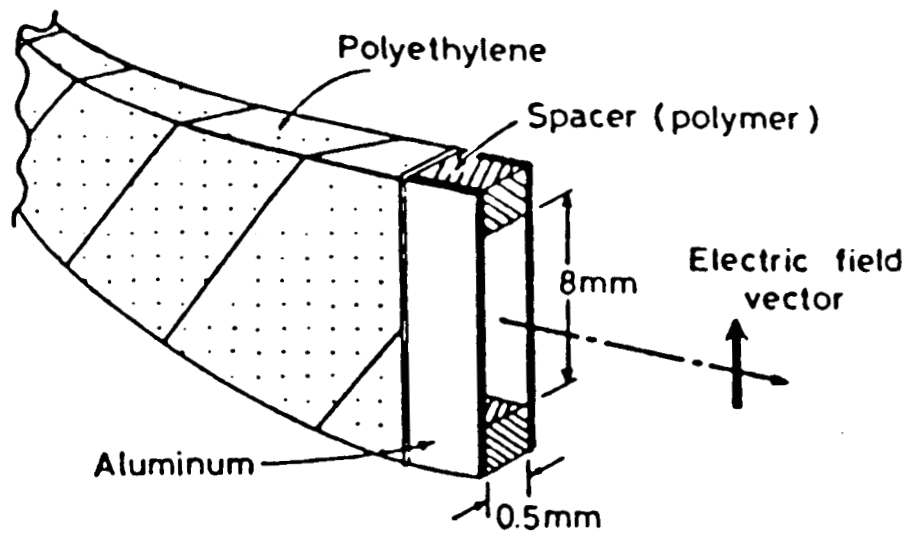

Figure 1-4. Structure of Guide Tube.

1.1 MID IR Fibers as a Guiding Medium:

The successful development of mid-infrared fiber optics will provide improved or extended capabilities beyond those of present day fiber systems and will expand new application areas. For example, MIR fibers potentially offer lower intrinsic losses than do silicate-based fibers. Therefore, MIR fibers have a variety of applications such as medical (4-7) (losses are not important), where they have been used in surgery and in couterization and photocoagulation, also as IR diagnostics, imaging and finally for internal tomography. Infrared fibers along with powerful lasers can be used for micro-welding and cutting. In addition to the applications mentioned, IR fibers can also be used in nonlinear optics for optical computation and phase conjugation measurements. Probably the most critical application is communication, where IR fibers are used as a communication link because of the high bit rate and wide branwidth of this region of the spectrum where also losses are very low.

Optical fibers are recently developed for MIR, where they offer the potential of lower losses and greater tolerance to nuclear radiation than current silicate based fibers.

In shorter optical link applications, such as infrared optics, they are already at the stage of commercial usage. Although a wide array of potentially highly transmissive MIR materials are available in bulk form, most are not suitable for fiber fabrication.

There are several types of materials for MIR fibers: single crystal, polycrstalline and virteous. Crystalline materials are useful due to their potentially broad transmission band (30 microns and beyond with some alkali halides) and low intrinsic loss.

Recently, a new class of multicomponent glasses based on the flourides of heavy metals have come into the use with potentially superior MIR performance.

Virtually all heavy metal flouride glass fibers drawn to date have been ZrF_4 based type. Althougb, it was verified that bulk flourozirconate glasses display a Rayleigh scattering loss dependence. Flouride glass fibers drawn from preforms have shown lowest optical losses compared with other type of IR fibers available now. Flourozirconate glasses are susceptible to moisture attack, and also corrosion has been reported to occur in flouride glass fibers resulting in significant reduction in strength. Nevertheless, total losses of < 10 dB/Km, low scattering, and good uniformity control have been reported.

A class of infrared glasses of interest are the chalcogenide of single component glasses such as As_2S_3, and GeS_2, and multicomponent glasses containing As, Sb, Te and/or S. The main feature of these glasses is the broad infrared transparency band to 12 microns and beyond. However, poor near IR to visible transparency makes transmission system testing and alignment more difficult. Other disadvantages include toxicity of As containing glasses, relatively poor mechanical characteristics, and extreme difficulty in the elimination of hydrogen impurities.

Heavy metal oxide glasses possess extended IR transmission ranges relative to silicate and should therefore access lower minimum losses. Typical glasses could be based on GeO_2, Sb_2O_3, TeO_2, or La_2O_3; calcium aluminate glasses are another possiblity. while the heaviest glasses should possess the lowest minimum losses (approximately 0.01 dB/Km for TeO_2, assuming the same scattering loss as fused silica), they are the most difficult to stablilze and possess the highest refractive indices and poorest mechanical properties. For this reason, fiber studies have been limited primarily to GeO_2 based systems.

Silver halide fibers have been fabricated by extrusion. Pure AgCl, AgBr and alloys of AgCl and AgBro crystals were extruded through diamond dies. These fibers are either unclad or used in a loose sleeve for cladding. All measurements at present have to be carried out under red light to prevent darkening of the fibers since such fibers are sensitive to UV. Losses in the fibers are found to be about 0.7 dB/m at 10.6 micron (8). These fibers are quite flexible.

The present status of MIR fibers points to the use of KRS-5 polycrystalline extruded fibers with a loss around 0.1 dB/m at 10.6 micron (9) and capacity of withstanding high power CO_2 laser radiation. But these fibers are too toxic and brittle. The polycrystalline AgCl or AgBr and single crystal CSI fibers appear very promising for operation up to 10.6 microns.

There are many crystalling materials aw well as glasses that possess the necessary intrinsic characteristics for achieving both ultralow losses (o.01 dB/Km and lower) and low pulse dispersions. The principal advantages and disadvantages of various fiber materials/designs are summarized in Table 1-1.

Fiber types	Advantages	Disadvantages
Glasses	Potential losses less than 10^{-2} dB/km Core-clad and graded-index possible Copositional flexibility Can be drawn into long lengths from preforms or directly from melt Can be fusion-spliced	Some compositions are susceptible to devitrification and/or chemical corrosion
Polychrystalline materials	Potential for lower losses than glasses Very broad transparency range	Large scattering from bulk and surface defects Difficult to clad or grade index Inferior mechanical properties Difficult to control uniformity over long lengths
Single crystal	Low loss and broad transparency as with polycrystalline materials Can be very strong Scattering can be very low	Difficult to clad & grade index Methods for frabricating long continuous lengths are uncertain
Liquid-filled hollow fibers	Potentially low scattering loss Potentially high laser damage threshold	Difficult to terminate & splice Materials suitable for untralow loss are unknown Hollow fibers tend to be weak
Hollow fibers	High power transmission may be possible	Susceptible to bending losses Attaining ultrahigh reflectivity inner surfaces is difficult Methods for fabricating long continuous lengths are unknown Uncertain pulse dispersion characteristics

Table 1-1. Advantages and Disadvantages of Various Types of IR Fibers.

CHAPTER TWO

PROPERTIES OF MID AND FAR INFRARED FIBERS

2.1 Introduction

There is no doubt the current surge of activities in the research on IR fibers is the result of prospective applications of these fibers in wide areas of medical practice, such as endoscopes and laser delivery system in surgery. These initial requirements on fibers for sufficient flexibility, power carrying capability, reasonably low loss and absence of toxicity, chemical inertness are for the purpose of replacing articulated arms and the use of natural body orifices for nonintrusive diagnostic and surgery. These can be satisfied with fibers of mm diameter and losses of fractions of dB per meter. Current fibers do satisfy these conditions. However, for future pinpoint surgery with highly localized burns, the development of much smaller diameter and even single-mode fibers is essential. Such requirements will then match those in high speed IR communication systems.

Figure 2-1 describes the estimated minimum transmission loss of various kinds of infrared fibers. In the following sections we will describe some properties of the available infrared optical fibers.

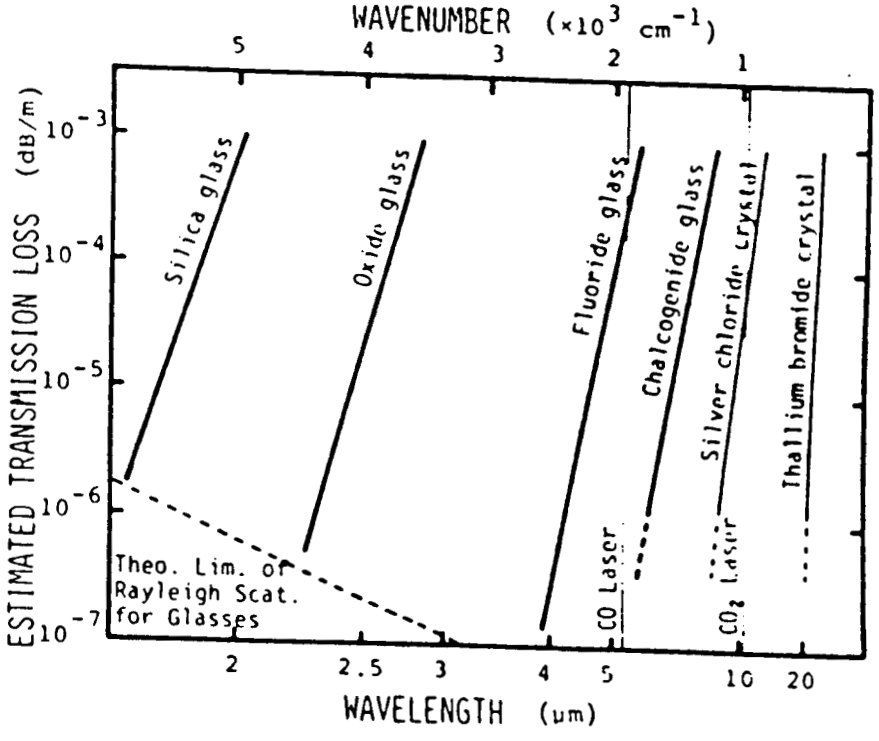

Figure 2-1. The Estimated Transmission Loss of Various Fibers in Infrared.

2.2 Silver Halide Infrared Optical Fibers

Silver halide fibers such as AgCl and AgBr are preferred among chalcogenide glass and crystalline fibers due to their nontoxicity, flexibility, and nonsolubility in water. Because of these advantages, silver halides have a unique application in radiometric measurements, thermal imaging, and delivery of high power CO_2 laser radiation in surgical and spectroscopic systems.

Figure 2-2 (a), a longitudinal cross section of the fiber, shows the structure along the axis of the fiber. An electron micrograph of the transverse cross section (Figure 2-2 (b)), shows that the fiber consists of a fine grain structure of about 1 mm in size. Annealing of the fibers following extrusion leads to grain growth. Figure 2-2 (c) shows the transverse cross sectional appearance after an anneal at 200 C. However, Figures 2-3 (a) and (b) compare the grain size of a fiber of pure AgBr with that of pure AgCl. The difference in grain size is roughly an order of magnitude.

Some recent measurements have been performed by Sa'ar, Moser, Akselrod, and Katzir [8] on silver halide fibers extruded from high-purity mixed silver halide crystals of composition $AgCl_{0.95}Br_{0.65}$ show a minimum loss of 0.7 dB/m. The fibers are unclad, flexible, and only weakly sensitive to near ultraviolet radiation. The fibers have a diameter of 0.9 mm and are up to 2 m in length. These fibers are capable of transmitting high power CO_2 laser. Figures 2-4 and 2-5 compare the x-ray transmission diffraction of an extruded AgBr fiber with that of an AgCl fiber.

(a) 200 μm

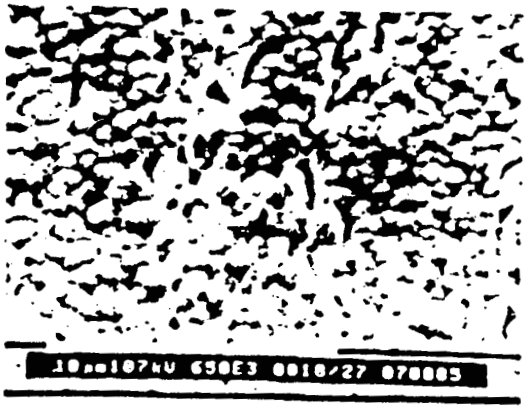

(b) 200 μm

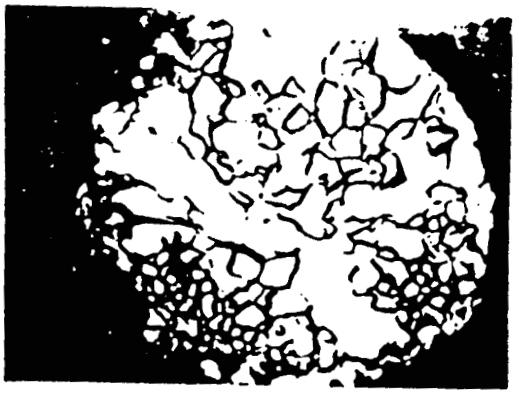

(c) 10 μm

Figure 2-2. Micrographs of Fiber Cross Section.
(a) Longitudinal Cross-section After Extrusion.
(b) The Fine Grain Structure of the Fiber
(c) After Annealing at 200°C.

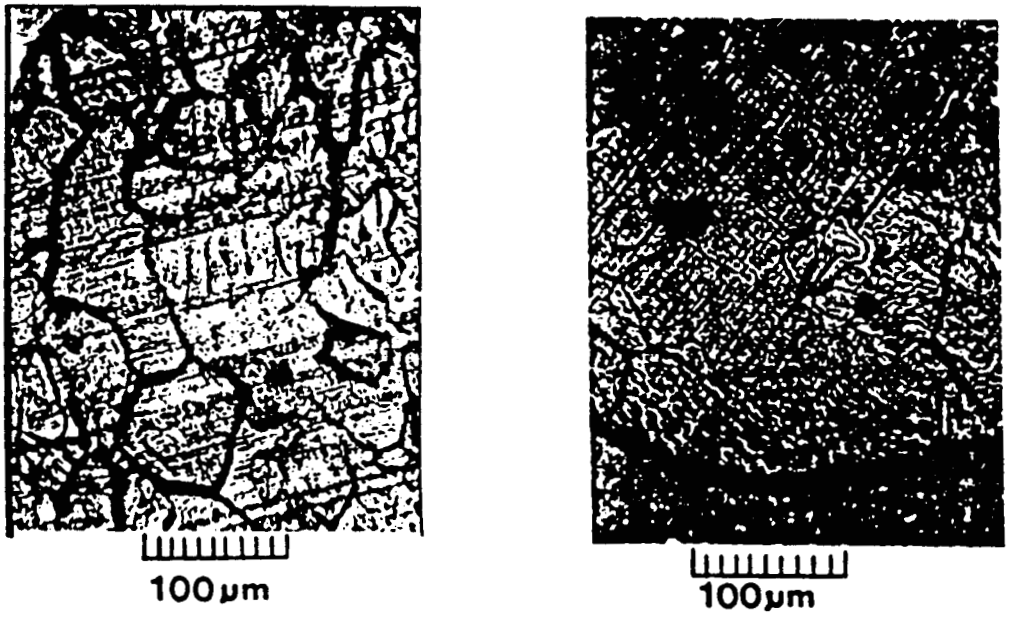

Figure 2-3. Grain Structure of Silver Halides.
(a) AgBr Grain Structure
(b) AgCl Grain Structure

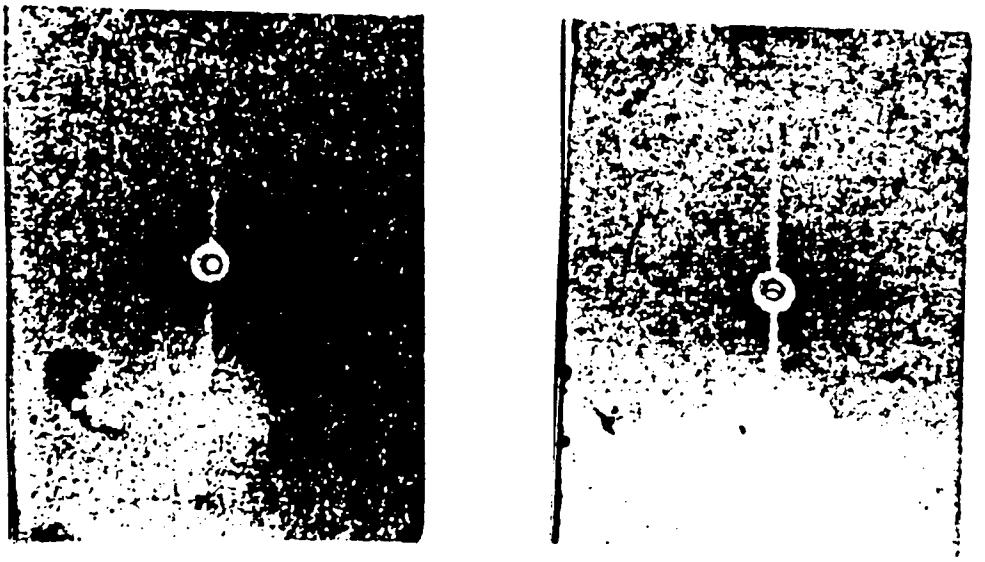

(a) (b)

Figure 2-4. Transmission X-Ray Diffraction of an Extruded AgBr Fiber.
(a) Extruded Fiber.
(b) Same Fiber After Annealing.

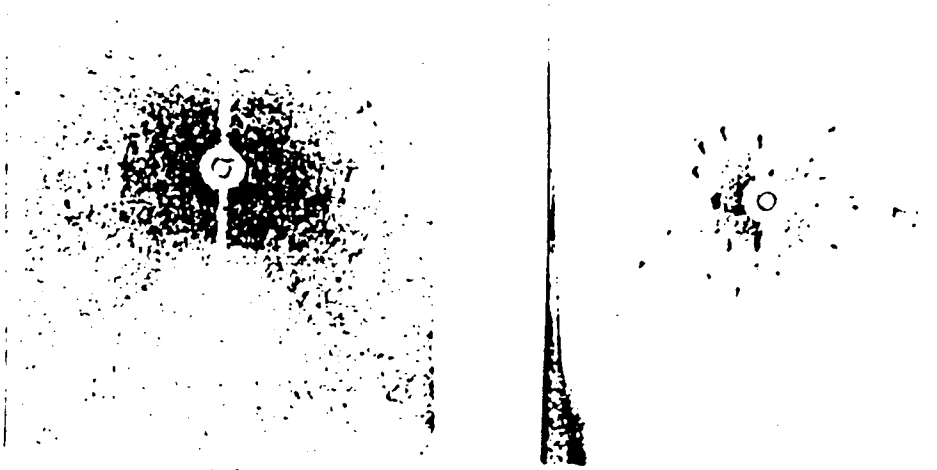

(a) (b)

Figure 2-5. Transmission X-Ray Diffraction of an Extruded AgCl Fiber.
(a) Extruded Fiber.
(b) Same Fiber After Annealing.

For small loss and negligible interference effects, the total loss in units of dB/m can be expressed by:

$$\alpha_T = [2\ln(1-r) - \ln[P(L)/P_{IN}]] \quad (10/L) \qquad (2.1)$$

where L is the length of the fiber in meters, P_{IN} and P(L) are the input and output power, respectively, and r is the reflection coefficient calculated from the known index of refraction of the silver halides.

The total attenuation coefficient was determined as a function of wavelength using Eq. (2.1). It is convenient to write the total attenuation coefficient as follows:

$$\alpha_T(\lambda) = \alpha_{BG}(\lambda) + \alpha_{IMP}(\lambda) \qquad (2.2)$$

where $\alpha_{IMP}(\lambda)$ is the absorption coefficient related to impurities in the fiber. The background term $\alpha_{BG}(\lambda)$ was related by Harrington and Sparks to large scale optically thin scatterers that lead to a spectral dependence of the form

$$\alpha_{BG}(\lambda) = A\lambda^{-2} + B \qquad (2.3)$$

Figure 2-6 shows the measured total attenuation coefficient. The background can be fit to the expression $(16.2\lambda^{-2} + 0.5)$ dB/m consistent with the scatter model of Harrington and Sparks. The

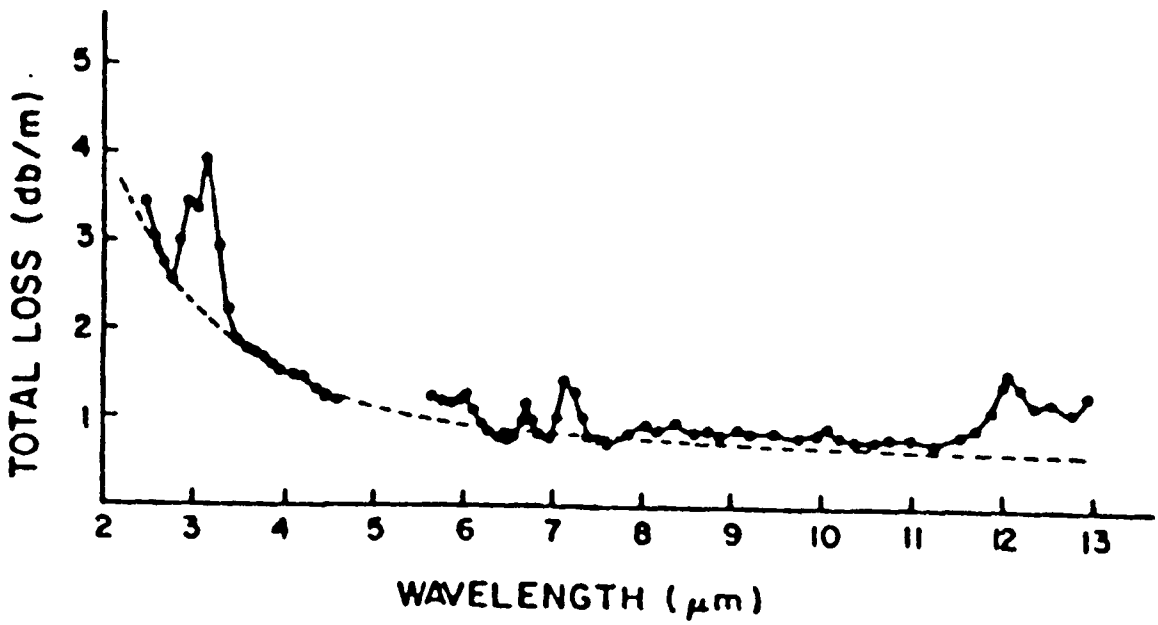

Figure 2-6. Total Loss as a Function of Wavelength (solid line). The Dashed Line is a Plot of the Scattering Term $[16.2\,\lambda^{-2} + 0.5]$ dB/m.

impurity absorption shows a strong line centered at 3-3.2 μm, weaker lines at 6.1, 6.8 and 7.1 μm, and a broad absorption feature at 12-13 μm. The bands at 3-3.2 and 6.1 μm are assigned to water. The water also gives rise to the absorption in the 12-13 μm region. The bands at 6.8 and 7.1 μm are assigned to CO_3 molecules. Mimura showed that forming fibers in a CO_2 atmosphere strongly enhanced these bands.

It is clearly shown in Figure 2-6 that the total loss of the silver halide fibers around $\lambda = 10$ m is reasonably small compared to other infrared fibers available and since the CO_2 laser wavelength is 10.6 μm, then it is very convenient to integrate the CO_2 laser with silver halide fibers in a compacted system.

2.3 KRS-5 Optical Fibers:

KRS-5 (thallium bromoiodide) is one of the materials used in CO_2 laser power transmitting fibers, and is formed by extrusion. Transmission of up to 100 W of CO_2 laser power, and transmission with a loss of 0.12 dB/m at 10.6 μm [9,10], were reported, while the theoretical limit for the material is 0.001 dB/Km at this wavelength.

KRS-5 is mostly used for radiometric sensing and communication systems. These fibers have a very broad transmission wavelength window. The typical loss spectrum of fiber fabricated by Kachi, Nakamura, Kimura, and Siroyama is shown in Figure 2-7. The lowest loss wavelength is around 20 μm, and the transmission window for this

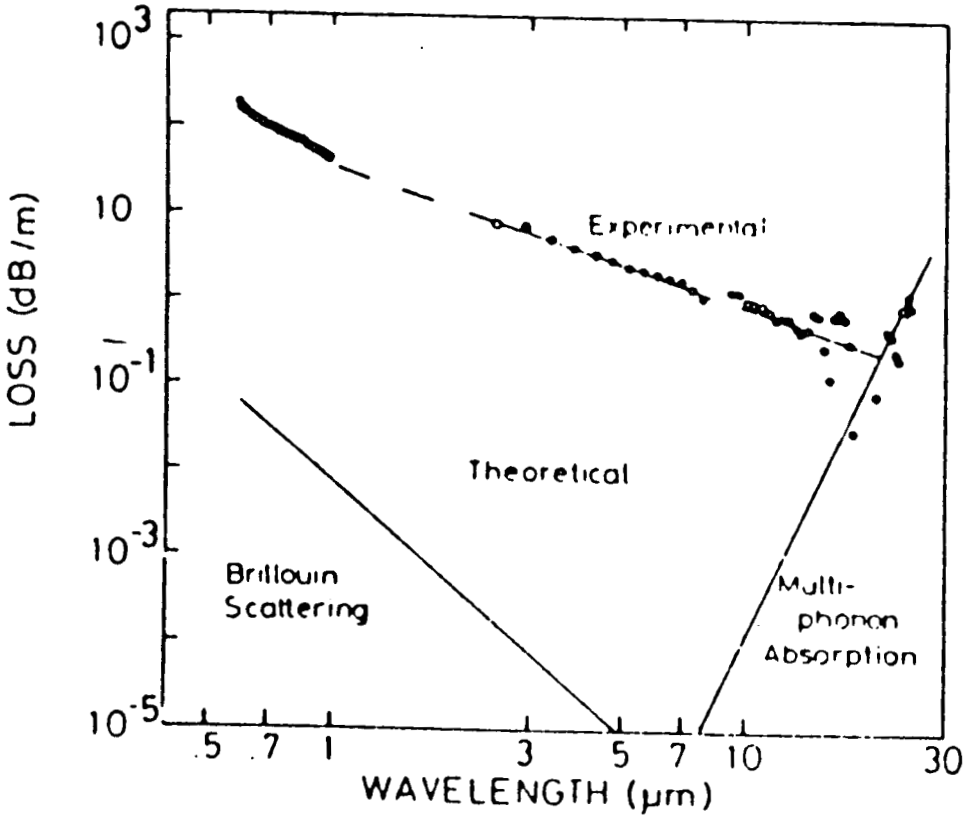

Figure 2-7. Typical Transmission Loss Spectrum of KRS-5 Fibers and Theoretically Predicted Limit of the Material.

fiber is in the 5 to 25 μm wavelength region. For lower temperatures, the intensities of longer wavelength components increase. The peak of the radiation spectrum at 300°K lies near 10 μm.

Extrinsic loss mechanisms are believed to be scattering due to crystalline imperfection and roughness of the core surface, because the crystal suffered extensive deformation during the fiber extrusion, and smoothness of the fiber surface will be influenced by the surfaces of dies. However, the scattering loss can be reduced in the 3-6 μm wavelength region by annealing. Table 2-1 shows some of the results on two samples of KRS-5 fibers before and after annealing process, also Figure 2-8 shows the dependence of the loss on an annealing time.

The lowest loss reported on this fiber is 0.12 dB/m for a fiber 1 μm in diameter and 1 m in length. However, the theoretically predicted loss for this fiber is 0.001 dB/Km.

The thallium halides have low solubility and melting points but have high indices of refraction which can present problems in finding a suitable cladding. The fiber grain size varies between 3 and 50 μm for the thallium halides. The actual grain size for a particular fiber depends on the extrusion temperature which, for these ductile materials varies from 200 to 350°C.

2.4 Heavy Metal Fluoride Optical Fibers:

Recent research into IR transmitting materials and fibers may well find applications in IR systems such as low temperature pyrometry, CO

FIBER LENGTH (cm)	BEFORE ANNEALING	AFTER ANNEALING
107.2	0.59 dB/m	0.21 dB/m
101.4	0.29 dB/m	0.12 dB/m

Figure 2-1. Reduction of the transmission Loss at 10.6 μm by Annealing.

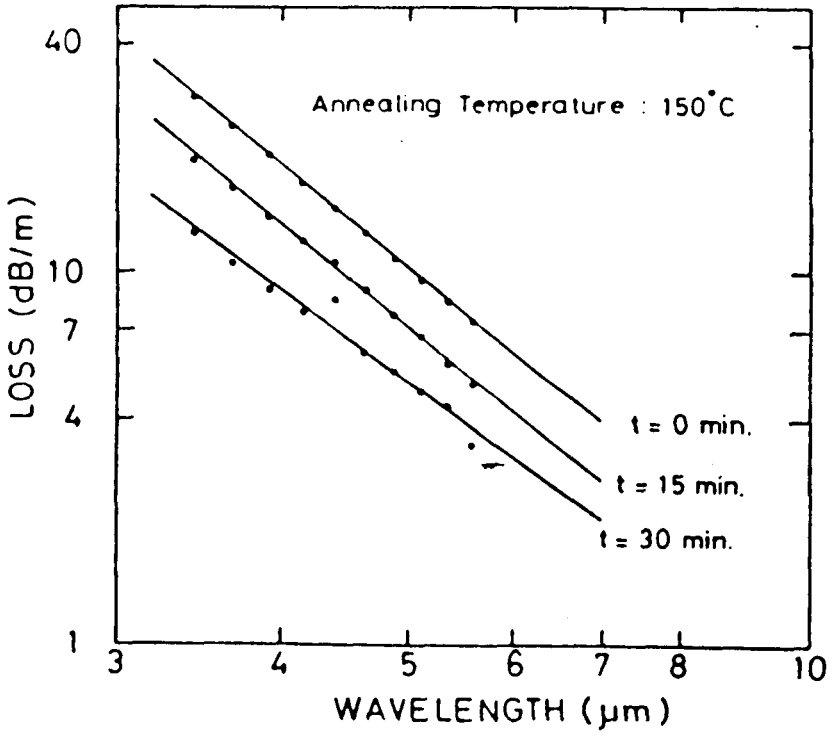

Figure 2-8. Lowering of the Loss Spectrum of KRS-5 Fiber by Annealing.

power transmission, IR spectroscopy and IR imaging. However, probably the most significant use might come from long distance communication systems where the shift of the operating wavelength to the 2-4 μm region would give lower Rayleigh scattering and hence lower overall losses.

There are several fluoride materials used in fabricating IR optical fibers [11,12], but ZrF_4 (ZBLAN) is the most significant to us since this fiber has the lowest intrinsic loss with a value of 0.011 dB/Km and at present is probably the best candidate for low loss fiber.

The overall minimum loss in ZrF_4 based IR fibers can be estimated by combing the expected impurity concentrations with the absorption coefficients. Table 2-2 summarizes each of these and lists the expected loss at 2.55 μm. Figure 2-9 also illustrates these absorptions and shows that when combined with the intrinsic losses the minimum loss wavelength should be at 2.56 μm. The results suggest that absorption losses of about 0.02 dB/Km may be feasible and that overall losses of 0.03 dB/Km could be expected at 2.56 μm. This figure compares with a typical loss of 0.02 dB/Km at 1.55 μm in silica fiber so that factors of 6-7 improvement may be possible with IR fibers.

2.5 Chalcogenide IR Glass Optical Fibers:

Chalcogenide fibers had been proposed as ultra-low-loss optical fibers [12 through 16]. However, it has been clarified that they have a fatal disadvantage in transmission properties. This is because they exhibit a weak absorption tail which is attributed to a certain defect

IMPURITY	CONCENTRATION ppb	ABSORP. COEF. 2.55 μ m dB/Km/ppb * 10^3	LOSS 2.55 μ m dB/Km * 10^3
OH^-	2.0	< 1.0	< 1.0
Fe^{2+}	10 Fe = 0.1 Fe^{2+}	15.0	1.5
Cu^{2+}	2.0	3.0	6.0
CO^{2+}	0.1	17.0	1.7
Ni^{3+}	0.3	2.4	0.7
Ce^{3+}	5.0	-	-
Pr^{3+}	0.3	0.01	0.3
Nd^{3+}	0.3	22.0	6.6
Sn^{3+}	0.3	3.3	1.0
Eu^{3+}	0.3	2.5	0.7
Tb^{3+}	0.3	0.2	-
Dy^{3+}	0.3	1.6	0.5
	Rayleigh Scattering		7.9
	IR Edge		3.1
		Total	31.0

Table 2-2. Estimated Losses of ZrF_4 IR Fibers.

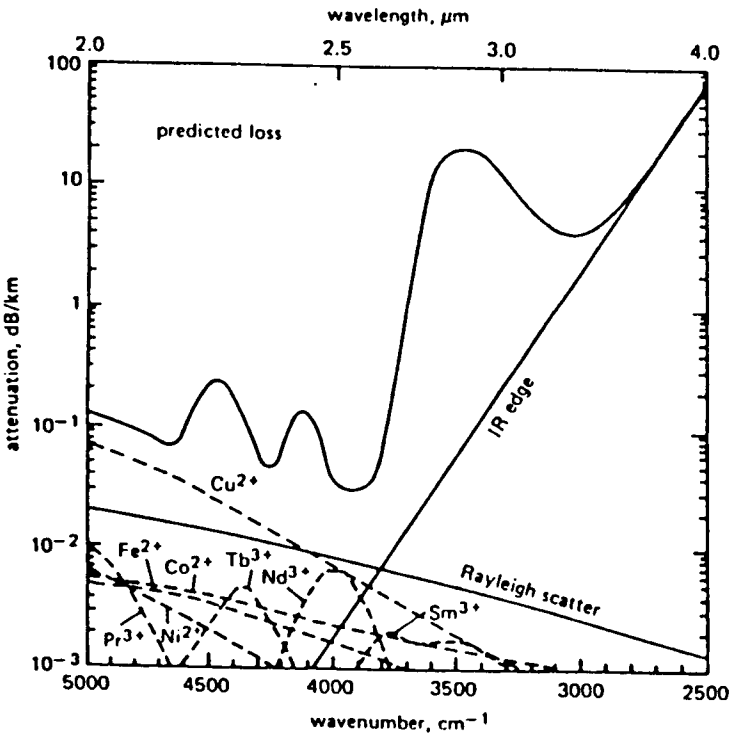

Figure 2-9. Predicted Minimum Losses in ZrF_4 Fibers.

associated with electrons. However, these fibers have broader window up to more than 10 μm.

Chalcogenide glasses that transmit in the 8-12μm waveband generally consist of two or more of the elements Ge, As, Se or those below them in the periodic table. The use of such glasses offer the advantages of speed and control normally associated with oxide fiber-drawing techniques, and yields fibers that are both flexible and chemically durable.

2.5.1 As-S Chalcogenide Fiber:

Arsenic sulphide glass fibers whose stoichiometric composition is As_2S_3 have a transmission window of 2-6μm. As-s fibers are drawn from perform with Teflon-FEP jacketing or from the melt using a double crucible. Distillation of raw material is generally made to remove hydrogen and oxide impurities. A glass ingot is formed by melting the mixture of purified As and S in a silica ampoule followed by rapid cooling.

The minimum loss of As-S fibers intended for optical communication has been realized to be 35 dB/Km at 2.4 μm as shown in Figure 2-10. Several absorptions due to impurities appear at 2.91 μm of OH and 4.03 μm of SH [17]. The minimum loss is strongly affected by weak absorption tail which depends on the synthesis process. This absorption is decreased by introducing hydrogen into the glass. However, As-S fibers are not applicable to telecommunications because of a relatively high loss due to undesirable weak absorption tail.

One of the current topics of interest concerning As-S fibers is power delivery for a CO laser whose oscillation wavelengths are around 5.3 μm. Such short distance power delivery is being developed for surgery and machining. A loss less than 100 dB/Km is adequate for these uses. Without forced cooling, transmission power density of 14 KW/cm has been achieved [16]. However, slight damage occurs at the output end due to the extremely high power.

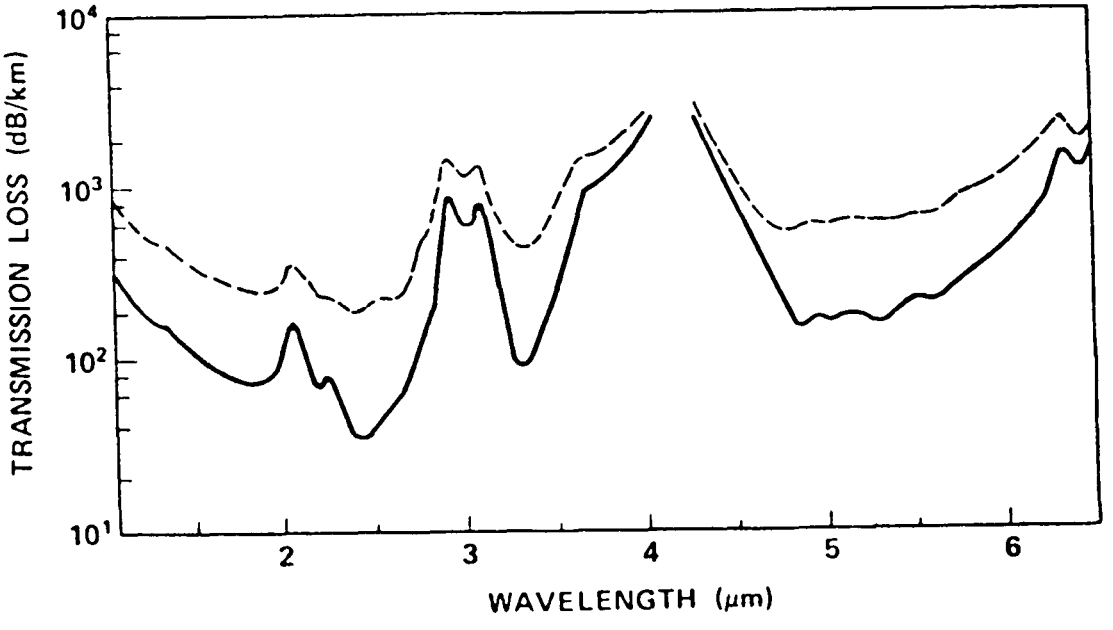

Figure 2-10. Transmission Loss for an As-S Glass Unclad Fiber (solid line) and an As-S Core-clad Fiber with a Δn of 2.3% (dashed line).

For remote sensing application areas, an As-S bundle fiber has been successfully developed for a length over 10 m [18]. The bundle fibers containing 200-300 cores shown in Figure 2-11 are fabricated by simultaneously drawing the preform bundle composed of small diameter rods. Each rod is drawn from the same ingot preform jacketed with a FEP tube. Imager transmitting bundle fibers are expected to have many applications, such as in the nuclear industry, in temperature measurements to room temperature, and in IR spectroscopy.

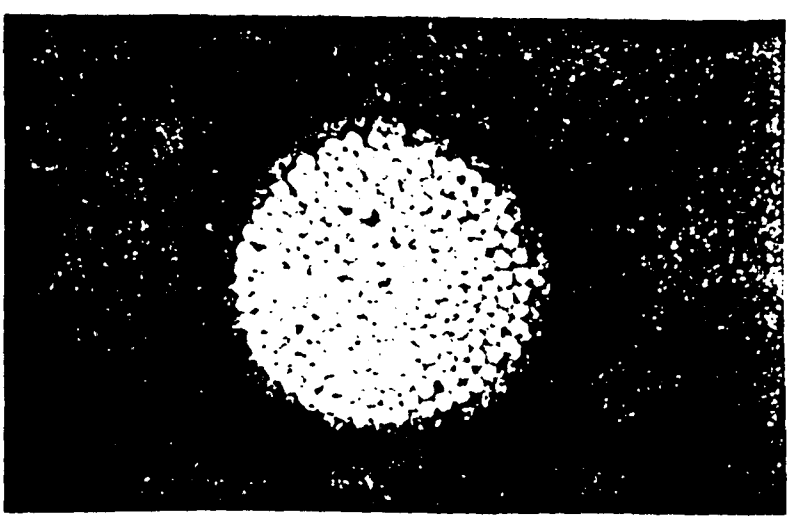

Figure 2-11. Photo of Cross Section of an As-S Image Guide Fiber. This bundle fiber is 200 μm in diameter including 200 cores of 90 μm diameter.

2.5.2 Zinc Selenide IR Optical Fibers:

ZnSe is a widely used infrared polycrystalline material which is transparent over a wide range of wavelengths from 0.6-14 μ m. It is currently used as windows for CO_2 lasers, as lenses in many military IR optical systems, and for color correctors. CVD incorporated manufacturers ZnSe by chemical vapor deposition (CVD) process to form solid, theoretically dense, high purity, polycrystalline ZnSe. The bulk absorption coefficient of CVD-ZnSe as measured by laser calorimetry at a number of different wavelengths is shown in Table 2-3. As can be seen, CVD-ZnSe has low bulk absorption over a wide wavelength range making it an excellent candidate for an IR waveguide. The absorption coefficient, α, at 10.6 μm changes from 5×10^{-4} to 1×10^{-3} cm^{-1} respectively as the temperature changes from 25 to 225°C, therefore, $d\alpha/dT$ is 4×10^{-6} cm^{-1} K^{-1} in this temperature range. Because of the small value of $d\alpha/dT$ and the low

Table 2-3. Bulk Absorption Coefficient of ZnSe.

Wavelength (um)	Bulk Absorption Coefficient (cm^{-1})	(dB/m)
1.319	0.0054*	2.3*
2.77	0.0007	0.30
3.8	0.0004	0.17
5.25	0.0004	0.17
10.6	0.0005	0.22

*Includes surface absorption

bulk absorption coefficient, the expected temperature rise of a ZnSe fibers operated at 10.6 μm does not influence the power transmission, even at 100 watts throughput.

In addition to its excellent optical properties, ZnSe has good mechanical properties for the construction of a fiber. For typical CVD polycrystalling ZnSe, the calculated minimum bend radius, r_m, for a 1 μm diameter uncladded fiber is 60 cm [19]. This is improved by either decreasing the grain size or by suitable cladding. In general, for polychrystalline materials, the smaller the grain size, the larger the fiber strength [20]. The flexural strength increases linearly as the reciprocal of the square root of the grain size. Since the bend radius decreases as the flexural strength increases, a smaller bend radius is realized by decreasing the grain size from the present value of 70 μm for typical CVD-ZnSe. The use of a flexible cladding on the fiber would also decrease the bend radius.

ZnSe is very inert and can withstand many corrosive environments such as moderately strong acids and bases. In addition, it is non-hydroscopic, non-flammable, and insoluble in alcohols, saline solutions and may other organic solvents. These characteristics and the excellent optical and mechanical properties make ZnSe a good choice for an IR optical fiber to be utilized in a mechanical environment.

A complete experimental investigations on halide (AgCl), KRS-5, and chalcogenide IR optical fibers available in our laboratory is shown in Chapter Four.

CHAPTER THREE

MODE ANALYSIS OF OPTICAL FIBERS

3.1 Introduction

The simplest way to understand the behavior of the optical power propagation in an optical fiber is to examine the appearance of modal fields in the planar dielectric slab waveguide. This waveguide is composed of a dielectric slab of refractive index n_1 sandwiched between dielectric material of refractive index $n_2 < n_1$, which we call the cladding. A cross sectional view of the slab waveguide looks the same as the cross-sectional view of an optical fiber cut along its axis. The order of a mode is equal to the number of field maxima across the guide. The order of the mode is also related to the angle that the ray congruence corresponding to this mode makes with the plane of the waveguide or the axis of a fiber; that is, the steeper the angle, the higher the order of the mode. The electric fields of the guided modes are not completely confined to the central dielectric slab (that is, they do not go to zero at the guide - cladding interface), but instead, they extend partially into the cladding. The fields vary harmonically in the guiding region of the refractive index n_1 and decay exponentially outside of this region. For low order modes the fields are tightly concentrated near the center of the slab or the axis of an optical fiber with little

penetration into the cladding region. On the other hand, for higher order modes the fields are distributed more toward the edges of the guide and penetrate further into the cladding region.

Solving Maxwell's equations shows that in addition to supporting a finite number of guided modes, the optical fiber waveguide has infinite continuum of radiation modes that are not trapped in the core and guided by the fiber but are still solutions of the same boundary-value problem. The radiation field basically results from the optical power that is outside the fiber acceptance angle being refracted out of the core. Because of the finite radius of the cladding, some of this radiation gets trapped in the cladding, thereby causing cladding modes to appear (but it is not true in the case of infrared optical fiber due to the lack of fabricating an uncladded optical fiber). As the core and cladding modes propogate along the fiber in the visible range, mode coupling occurs between the cladding modes and the higher order modes. This coupling occurs because the electric fields of the guided core modes are not completely confined to the core but extend partially into the cladding and likewise for the cladding modes. A diffusion of power back and forth between the core and cladding modes thus occurs, which generally results in a loss of power from the core modes. In practice, the cladding modes will be suppressed by a glossy coating which covers the fiber or they will scatter out of the fiber after traveling a certain distance because of roughness on the cladding surface.

In addition to bound and refracted modes, a third category of modes called leaky modes is present in optical fibers. These leaky modes are only partially confined to the core region, and attenuate by continuously radiating their power out of the core as they propagate along the fiber. This power radiation out of the waveguide results from a quantum mechanical phenomenon known as the tunnel effect.

Hybrid modes exist in the fiber if both electric and magnetic fields along the fiber axis are non-zero. These are designated as HE or EH modes, depending on whether the magnetic or electric field respectively makes a large contribution of the transverse field.

3.2 Modal Equation:

The eigenvalue equation for β can be achieved by first considering Maxwell's equations in order to derive the E and H field components in the fiber. Since the light propagation is along the Z axis of the fiber, then E and H fields have to be in the Z direction and are expressed in terms of Bessel functions as [21]

$$E_z \ (r<a) = A \ J_\nu \ (Ur) \ e^{j\nu\Phi} \ e^{j(\omega t - \beta z)} \tag{3.1}$$

$$H_z \ (r<a) = B \ J_\nu \ (Ur) \ e^{j\nu\Phi} \ e^{j(\omega t - \beta z)} \tag{3.2}$$

where A and B are arbitrary constants, and $e^{j(\omega t - \beta z)}$ is the time and z-dependent factors according to our assumption and $e^{j\nu\Phi}$ is a

periodic factor in ϕ with a period of 2π . Outside of the core both E and H fields along the fiber axis are expressed in terms of modified Besssel functions of the second kind.

$$E_z\ (r>a) = CK_\nu\ (Wr)\ e^{j\nu\Phi}\ e^{j(\omega t - \beta z)} \tag{3.3}$$

$$H_z\ (r>a) = DK_\nu\ (Wr)\ e^{j\nu\Phi}\ e^{j(\omega t - \beta z)} \tag{3.4}$$

with C and D being arbitrary constants.

The solutions for β must be determined from the boundary conditions. The boundary conditions require that the tangential components E_Φ and E_z of E inside and outside of the dielectric interface at r = a must be the same and, similarly, for the tangential components H_Φ and H_z. Therefore, from Eqs. (3.1) and (3.3) we have

$$E_{z_1} - E_{z_2} = A\ J_\nu\ (Ua) - c\ K_\nu\ (Wa) = 0 \tag{3.5}$$

the ϕ component is given as

$$E_\Phi = \frac{-j}{q^2}\left(\frac{\beta}{r}\frac{\partial E_z}{\partial \Phi} - \nu\omega \quad \frac{\partial H_z}{\partial r}\right) \tag{3.6}$$

inside the core

$$q^2 = u^2 = (K_1^2 - \beta^2)\ a^2 \tag{3.7}$$

where $K_1 = \frac{2\pi n_1}{\lambda} = \omega\sqrt{\varepsilon_1 \mu}$ while outside the core

$$W^2 = (\beta^2 - K_2^2)\ a^2 \tag{3.8}$$

with $K_2 = \frac{2\pi n_2}{\lambda} = \omega\sqrt{\epsilon_2 \mu}$ substituting Eqs (3.1) and (3.2) into Eq. (3.6) to find E_{ϕ_1}. Similarly Eqs. (3.3) and (3.4) into Eq. (3.6) to find E_{ϕ_2} yeild at r = a.

$$E_{\phi_1} - E_{\phi_2} = \frac{-j}{U^2} [A\, j\nu\, \beta J_\nu(Ua) - B\omega\mu U\, J_\nu'(Ua)] \qquad (3.9)$$

$$- \frac{j}{W^2} [C\, j\nu\, K_\nu(Wa) - D\omega\mu\, WK_\nu'(Wa)] = 0$$

where the prime indicates differentiation with respect to the agrument. Similarly, for the the tangential components of H and by using the following equation.

$$H_\phi = \frac{-j}{q^2} \left(\frac{\beta}{r} \frac{\partial H_z}{\partial \phi} + \omega\epsilon \frac{\partial E_z}{\partial r} \right) \qquad (3.10)$$

along with Eqs. (3.1), (3.2), (3.3), and (3.4) it is readily shown that at r = a

$$H_{z_1} - H_{z_2} = BJ_\nu(Ua) - D\, K_\nu(Wa) = 0 \qquad (3.11)$$

$$H_{\phi_1} - H_{\phi_2} = \frac{-j}{U^2} [B\, j\nu\, \beta J_\nu(Ua) + A\omega\epsilon_1\, U\, J_\nu'(Ua)]$$

$$- \frac{j}{W^2} [D\, j\nu\, \beta K_\nu(Wa) + C\, \omega\epsilon_2\, WK_\nu'(Wa)] = 0 \qquad (3.12)$$

Eqs. (3.5), (3.9), (3.11) and (3.12) are a set of four equations with four unknown coefficients A,B,C and D. A solution to these equations exists only if the determinent of these coefficients is zero:

$$\begin{bmatrix} J_\nu(Ua) & 0 & -K_\nu(Wa) & 0 \\ \frac{\beta\nu}{U^2} J_\nu(Ua) & \frac{j\omega\mu}{U} J'_\nu(ua) & \frac{\beta\nu}{W^2} K_\nu(Wa) & \frac{j\omega\mu}{W} K'_\nu(Wa) \\ 0 & J_\nu(Ua) & 0 & -K_\nu(Wa) \\ \frac{-j\omega\mu_1}{U} J'_\nu(Ua) & \frac{\beta\nu}{U^2} J_\nu(Ua) & \frac{-j\omega\epsilon_2}{W} K'_\nu(Ua) & \frac{\beta\nu}{W^2} K_\nu(Wa) \end{bmatrix} = 0 \qquad (3.13)$$

Evaluation of this determinant yeilds the following eigenvalue equation for β :

$$[\bar{Y}_\nu(U) + \bar{X}_\nu(W)][K_1^2 \bar{Y}_\nu(U) + K_2^2 \bar{X}_\nu(W)] = (\beta\nu)^2 \left(\frac{1}{U^2} + \frac{1}{W^2}\right)^2 \qquad (3.14)$$

where

$$\bar{Y}_\nu(U) = \frac{J'_\nu(Ua)}{UJ_\nu(Ua)} \quad \text{and} \quad \bar{X}_\nu(\omega) = \frac{K'_\nu(Wa)}{WK_\nu(Wa)}$$

rearranging Eq. (3.14), then

$$[\bar{Y}_\nu(U) + \bar{X}_\nu(W)][n_1^2 \bar{Y}_\nu(U) + n_2^2 \bar{X}_\nu(W)] = \left(\frac{\beta\nu}{Ka}\right)^2 \left(\frac{V}{UW}\right)^4$$

where $K = \frac{2\pi}{\lambda}$

To derive the characteristic equations for HE and EH MODES we define the following parameters [22]

$$N = \frac{\beta}{K} \quad , \qquad B = \left(\frac{W}{V}\right)^2 \quad , \quad \text{then}$$

$$(\bar{Y}_\nu + \bar{X}_\nu)(n_1^2 \bar{Y}_\nu + n_2^2 \bar{X}_\nu) = \frac{\nu^2 N^2}{(U^2 B)^2} \tag{3.15}$$

treat Eq. (3.15) as a quadratic equation. In $\bar{Y}_\nu(U)$ then

$$n_1^2 \bar{Y}_\nu^2 + (n_1^2 + n_2^2)\, \bar{X}_x\, \bar{Y}_\nu + n_2^2\, \bar{x}_\nu^2 - \frac{\nu^2 N^2}{(U^2 B)^2} = 0 \tag{3.16}$$

solving for $\bar{Y}_\nu(U)$, then

$$\bar{Y}_\nu = -\frac{(n_1^2 + n_2^2)\, \bar{x}_\nu(W)}{2n_1^2} \pm \left\{ \left(\frac{(n_1^2 + n_2^2)}{2n_1^2} \right)^2 - \frac{n_2^2 \bar{X}_2(W)}{n_1^2} + \frac{2_N^2}{n_1^2 (u^2 B)^2} \right\}^{1/2}$$

By rearranging the proceeding equation, we get

$$\bar{Y}_\nu(U) = -\frac{(n_1^2 - n_2^2)}{2n_1^2}\, \bar{X}_\nu(W) \pm \left\{ \left(\frac{(n_1^2 - n_2^2)}{2n_1^2}\, \bar{X}_\nu(W) \right)^2 + \frac{\nu^2 N^2}{n_1^2 (u^2 B)^2} \right\}^{1/2} \tag{3.17}$$

Also $\bar{Y}_\nu(U)$ is defined from the modal equation as:

$$Y_\nu = \frac{J_\nu'(U)}{U J_\nu(U)} = \pm \frac{J_{\nu+1}(U)}{U\, J_\nu(U)} \mp \frac{\nu}{U^2} \tag{3.18}$$

Let us define some of the parameters used befor in order to find the rest of the unknown parameters such as N and B

$$U^2 = a^2 (K^2 n_1^2 - \beta^2) \quad \text{OR} \quad \beta^2 = K^2 n_1^2 - \frac{U^2}{a^2}$$

and $W^2 = a^2(\beta^2 - K^2 n_2^2)$ or $\beta^2 = K^2 n_1^2 - \frac{W^2}{a^2}$

then $2\beta^2 = K^2(n_1^2 + n_2^2) + \frac{1}{a^2}(W^2 - U^2)$

or $\beta^2 = \frac{K^2}{2}(n_1^2 + n_2^2) + \frac{1}{2a^2}(W^2 - U^2)$ (3.19)

Also, we know that $V^2 = U^2 + W^2 = a^2K^2(n_1^2 - n_2^2)$ solving for K^2, then

$$K^2 = \frac{V^2}{a^2(n_1^2 - n_2^2)} \tag{3.20}$$

By substituting Eqs. (3.19) and (3.20) into

$$N^2 = \frac{2}{K^2} \quad \text{then}$$

$$N^2 = \frac{n_1^2 + n_2^2}{2} + \frac{(W^2 - U^2)(n_1^2 - n_2^2)}{2V^2}$$

or

$$N^2 = \frac{(n_1^2 + n_2^2)(W^2 + U^2) + (W^2 - U^2)(n_1^2 - n_2^2)}{2V^2}$$

$$N^2 = \frac{U^2 n_2^2 + W^2 n_1^2}{V^2} \tag{3.21}$$

combining Eqs. (3.17), (3.18) and (3.21) along with the fact that

$$B = \left(\frac{W}{V}\right)^2$$

then we get the characteristic equation for the HE modes (minus sign) [22,23]:

$$\frac{J_{\nu-1}(U)}{J_\nu(U)} = -\frac{(n_1^2+n_2^2)}{2n_1^2}\,U\,\bar{X}_\nu(W) + \left\{\frac{\nu}{U} - U\left[\nu^2\left(\frac{1}{U^2}+\frac{1}{W^2}\right)\left(\frac{1}{U^2}+\frac{n_2^2}{n_1^2}\frac{1}{W^2}\right)\right.\right.$$

$$\left.\left.+\left(\frac{n_1^2-n_2^2}{2n_1^2}\,\bar{X}_\nu(W)\right)^2\right]^{1/2}\right\} \qquad (3.22)$$

and for EH MODES (plus sign) [22,23]:

$$\frac{J_{\nu+1}(U)}{J_\nu(U)} = \frac{(n_1^2+n_2^2)}{2n_1^2}\,U\,\bar{X}_\nu(W) + \left\{\frac{\nu}{U} - U\left[\left(\frac{1}{U^2}+\frac{1}{W^2}\right)\left(\frac{1}{U^2}+\frac{n_2^2}{n_1^2}\frac{1}{W^2}\right)\right.\right.$$

$$\left.\left.+\left(\frac{n_1^2-n_2^2}{2n_1^2}\,\bar{X}_\nu(W)\right)^2\right]^{1/2}\right\} \qquad (3.23)$$

$$\text{where } \bar{X}_\nu(W) = \frac{K_\nu'(W)}{WK_\nu(W)} = \frac{-K_{\nu-1}(W)}{WK_\nu(W)} - \frac{\nu}{W^2} \qquad (3.24)$$

3.3 Graphical Solution of the Characteristic Equation:

In this section plots of U vs. V will be presented for both weakly guiding and an unclad infrared optical fibers for comparison. A graphic software called energraphics is used to plot these curves [24].

To be able to plot the U-V graph, one has to first plot the left and right hand sides of Eqs. (3.22) and (3.23) for HE and EH modes respectively.

Eqs. (3.22) and (3.23) are plotted in Figures 3-1 to 3-8 for a weakly guiding fiber in the visible range with the use of the following equation:

$$V = (U^2 + W^2)^{1/2} = 2\pi\ a/\lambda\ \ (n_1^2 - n_2^2)^{1/2} \qquad (3.25)$$

where index of refraction $n_1 = 1.48$ and $n_2 = 1.465$ are chosen to be constants.

Figure 3-1 represents the plot of left hand side (LHS) and right hand side (RHS) of Eq. (3.22) for HE modes. In order to plot this figure several parameters must be first calculated such as W and $\bar{X}_\nu(W)$. Values of V were calculated from Eq. (3.25) in order to be able to calculate W for each assumed U value by using several values of 2a and λ. Figure 3-1 shows five curves that correspond to five 2a and λ values, these are 2a = 4 μm, 5, 6, 8 and 10 μm where λ = .75 μm, .7, .633, .6 and .55 μm respectively. To calculate $\bar{X}_\nu$ (W) from Eq. (3.24), we first have to calculate K'_ν (W) and $K_\nu(W)$. $K_\nu(W)$ can be easily found from the modified Bessel's functions tables [25] for $\nu = 1$, where K'(W) can be calculated from the following recurrence relation:

$$K'_\nu\ (W) = -1/2\ \{K_{\nu+1}(W) + K_{\nu-1}(W)\} \qquad (3.26)$$

where again both $K_{\nu+1}(W)$ and $K_{\nu-1}(W)$ can be found from the modified Bessel's functions tables [25] for $\nu = 1$. With the assumed values of

U the RHS of Eq. (3.22) can be plotted easily. The LHS of Eq. (3.22) can be calculated for $\nu = 1$ from the Bessel's functions tables [25]. Finally, both sides of Eq. (3.22) are plotted for P = 1, where P represents the first zero of the mode. The intersection points of the LHS and RHS of Eq. (3.22) are mode solutions. These intersection points were collected along with the V values calculated from Eq. (3.25) and plotted in Figure 3-17 labeled as HE_{11} mode, which is the fundamental mode of the weakly guiding fiber.

Figure 3-2 is plotted using the same procedure described for plotting Figure 3-1. But instead of using Eq. (3.22), Eq. (3.23) is used to plot EH modes. Again the same parameters V and W were used to plot the RHS of Eq. (3.23). Both $\bar{X}_{\nu}(W)$ and the LHS of Eq. (3.23) are calculated using the tables of modified and Bessel's functions for $\nu = 1$. Some bumps occur at the V = 4.72 and 8.8 due to the rapid jump between the values. It is clear that as mode order increases the intersection points become less. The intersection points of the LHS and RHS of Eq. (3.23) are gathered and plotted versues V in Figure 3-17 represented by EH_{11} mode.

Figure 3-3 is also plotted for $\nu = 2$ using Eq. (3.22) for HE modes. It is clear in this figure that the upper portion of RHS curves of Eq. (3.22) are not complete because of the fact that lower portion of the curves are important where the intersections with the LHS of Eq. (3.22) occur. This mode is represented by HE_{21} in Figure 3-17.

Figure 3-4 is plotted for $\nu = 2$ using Eq. (3.23) for EH modes. But since EH modes are generally higher than HE modes then the LHS of Eq. (3.23) intersect with only the highest V values, which means less intersection occur as the mode becomes higher. Some bumps are noticed that occur at V = 4.72 and 8.8 that is due to the rapid jump between the points. This mode corresponds to EH_{21} in Figure 3-17.

Figure 3-5 shows the plot of Eq. (3.22) for $\nu = 1$ and p = 3. This figure corresponds to HE_{13} mode in Figure 3-18. The same V and W values used to plot Figures 3-1 and 3-4 were used to plot this figure. Bessel's functions tables were used to calculate $\overline{X}_{\nu}(W)$, $J_{\nu-1}(U)$ and $J_{\nu}(U)$ of Eq. (3.22). Since this figure represents a higher mode than the previously plotted HE modes, then less intersection points occur.

Figure 3-6 represents the plot of Eq. (3.23) for EH modes. Even in this case less intersection points occur because of the order of the mode. Several bumps are noticed because of the big difference between the values calculated. The corresponding plot for this mode is labeled as EH_{12} in Figure 3-18.

Figure 3-7 is the plot of LHS and RHS of Eq. (3.22) for $\nu = 2$ and p = 3. It can be seen from this figure that we barely have two intersection points, however, the intersection of the curve with V = 8.8 and the curve of the LHS of Eq. (3.22) is not clear because the software used to draw these curves connects the points by drawing straight lines. Therefore, the accuracy of reading the value of U at

that intersection will be less. This mode corresponds to the HE_{23} in Figure 3-18.

Figure 3-8 is plotted for $\nu = 2$ and $p = 2$. This figure shows two intersection points only. The intersection at $V = 8.8$ also is not clear for the same reason mentioned for Figure 3-7. This mode is represented by EH_{22} mode in Figure 3-18.

Similarly, Eqs. (3.22) and (3.23) are plotted in Figures 3-9 to 3-16 for a KRS-5 unclad infrared optical fiber with $n_1 = 2.37$ and $n_2 = 1$ and several values of 2a and in the infrared region.

Figure 3-9 is plotted for $\nu = 1$ and $p = 1$. To plot the RHS of Eq. (3.22) for the HE modes, one has to calculate V and then W from Eq. (3.25). W can be calculated by assuming several U values. V is calculated from Eq. (3.25) by using several values for 2a and λ where $n_1 = 2.37$ and $n_2 = 1$ are constants. Since this fiber is uncladded then the V number becomes larger from that of the weakly guiding fiber. Values used to evaluate V are $2a = 10\,\mu m$, 15, 25, and $40\,\mu m$ where $\lambda = 7\,\mu m$, 9, 10.6, and $13.5\,\mu m$. It is noticeable from Figures 3-9 that the LHS of Eq. (3.22) is plotted as a straight line that is because the scale has been expanded besides the natural behavior of the software itself that joins the points by a straight line. The LHS of Eq. (3.22) behaves like a tangent. Again Bessel functions were incorporated to calculate $\bar{X}_{\nu}(W)$ from Eq. (3.24) and (3.26). The intersection points of LHS and RHS of Eq. (3.22) are collected and then plotted for each V value. The corresponding U-V

plot of this figure is shown in Figure 3-17 indicated by a prime, that is HE_{11}'.

Figure 3-10 shows the plot of Eq. (3.23) for $\nu = 1$ and $p = 1$. The upper portion of the LHS of Eq. (3.23) is not plotted, since the important part is where the curve intersect with the other V curves for the RHS of Eq. (3.23). The same 2a and parameters to calculate V and then W in Figure 3-9 were also used. The EH_{11}' mode in Figure 3-17 correspond to the intersection points in Figure 3-10 along with the V values specified.

In Figure 3-11 a plot of Eq. (3.22) for $\nu = 2$ and $p = 1$ is shown. The plot of LHS Eq. (3.22) is shown as a straight line because the scale has been expanded to achieve better intersection points of the LHS and RHS of Eq. (3.22) and then better readings. To plot these curves, the same method was used as described previously to plot Figures 3-9 and 3-10, even Figures 3-1 through 3-8. The corresponding plot of this figure is shown in Figure 3-17 indicated by HE_{21}' mode.

Figure 3-12 shows the plot of the LHS and RHS of Eq. (3.23) for EH modes when $\nu = 2$ and $p = 1$. The normal procedure described before were used to plot this figure. The LHS of this equation behaves like a cotangent function. The intersection points were collected along with the corresponding V value and then plotted in Figure 3-17 shown as EH_{21}' mode.

Figure 3-13 is plotted for higher order HE modes, when $\nu = 1$ and $p = 3$. This figure represents the plot of LHS and RHS of Eq. (3.22).

Small bumps occur at V = 9.64 and 11.25, these are due to the jump between the values calculated. The intersection points are plotted versus V in Figure 3-18 for comparison with the HE_{13} mode of the weakly guiding fiber, the mode is HE_{13}'.

Figure 3-14 is plotted for $\nu = 1$ and p = 2. This figure shows the plot of LHS and RHS of Eq. (3.23) for EH modes. The intersection points of this figure versus V are plotted in the U-V graph shown in Figure 3-18 indicated by EH_{12}' mode.

In Figure 3-15 a plot of LHS and RHS of Eq. (3.22) for higher order modes are shown when $\nu = 2$ and p = 3. Again the LHS of Eq. (3.22) looks like a straight line, that is due to the expansion of the scale in order to achieve a better intersection with the RHS of Eq. (3.22). The intersection at V = 9.64 is not clear because points are being connected by small straight lines, which increase the percent error in reading the U values on the X axis where this intersection occurs. This mode is represented in Figure 3-18 by HE_{23}'. Small bumps occurred at V = 9.64 and 11.25 in Figure 3-15.

Figure 3-16 shows a plot of LHS and RHS of Eq. (3.23) for $\nu = 2$ and p = 2. Again at V = 9.64 it is difficult to read the intersection point because the LHS and RHS at V = 9.64 do not intersect correctly, which causes the percent error to increase when reading the U value at the intersection. This mode is represented by EH_{22}' in Figure 3-18.

Figures 3-17 and 3-18 correspond to lower and higher order modes of both weakly guiding (Figures 3-1 through 3-8) and a KRS-5 unclad infrared fiber (Figures 3-9 through 3-16). The cutoff line in both

figures is found using Table 3-1. This table shows both cutoff and far from cutoff conditions for both fibers. These conditions are calculated using Bessel's function tables and the method of extrapolation. An alternative method to find the cutoff conditions is to use Bessel function roots [26]. Both HE and EH modes of the weakly guiding and unclad infrared fibers are plotted on the same graph for comparison. It is evident that the V number in uncladded infrared fiber is larger from that of a weakly guiding fiber, because it is difficult to fabricate a clad infrared fiber, which makes the index of refraction of the cladding larger, or in other words, the difference in the index of refraction between the core and cladding becomes smaller and thereafter less modes will propagate in the fiber because the V number gets smaller. Another reason is the difficulty of fabricating a single mode infrared fiber that limits the number of propagating modes in the fiber to the fundametnal mode.

At low V values, modes of the infrared optical fiber overlap those of the weakly guiding fiber. As the mode order increases this behavior disappears as is shown in Figure 3-18 for higher order modes. The prime in both figures 3-17 and 3-18 corresponds to KRS-5 unclad infrared optical fiber.

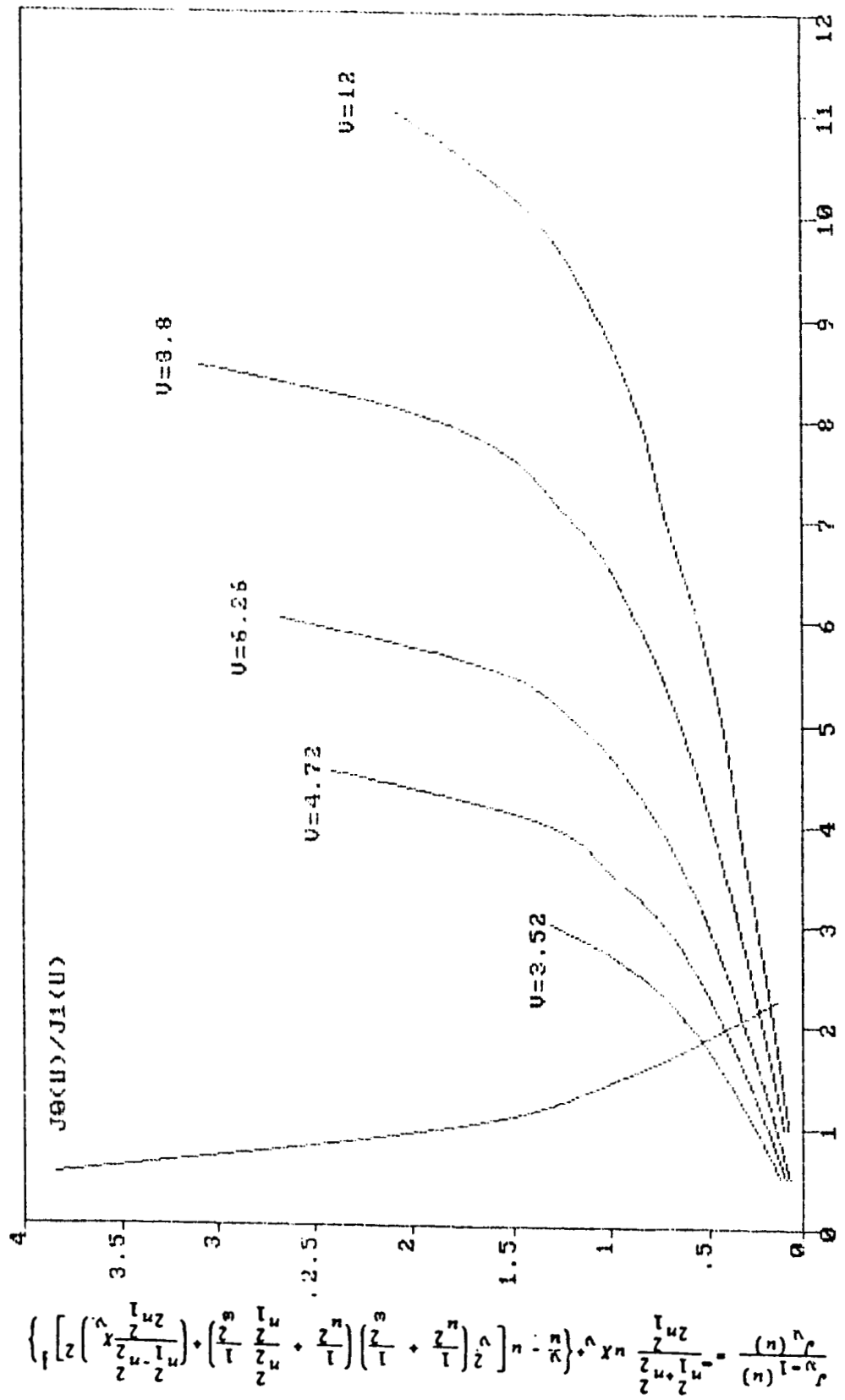

Figure 3-1. Plot of HE_{11} mode of a weakly guiding fiber. (Eq. 3.22 for ν=1,p=1).

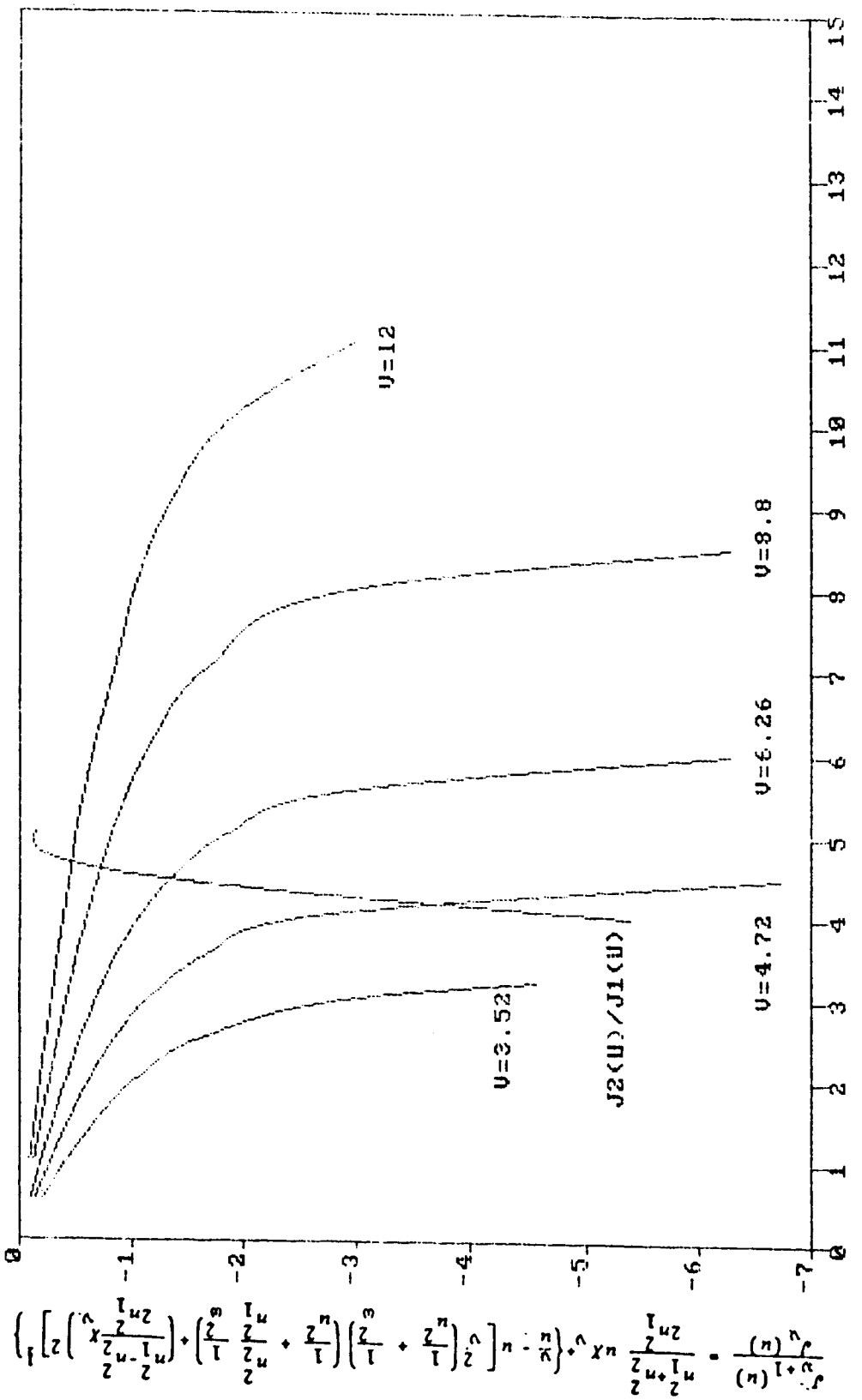

Figure 3-2. Plot of EH_{11} mode of a weakly guiding fiber (Eq. 3.23 for v=1, p=1).

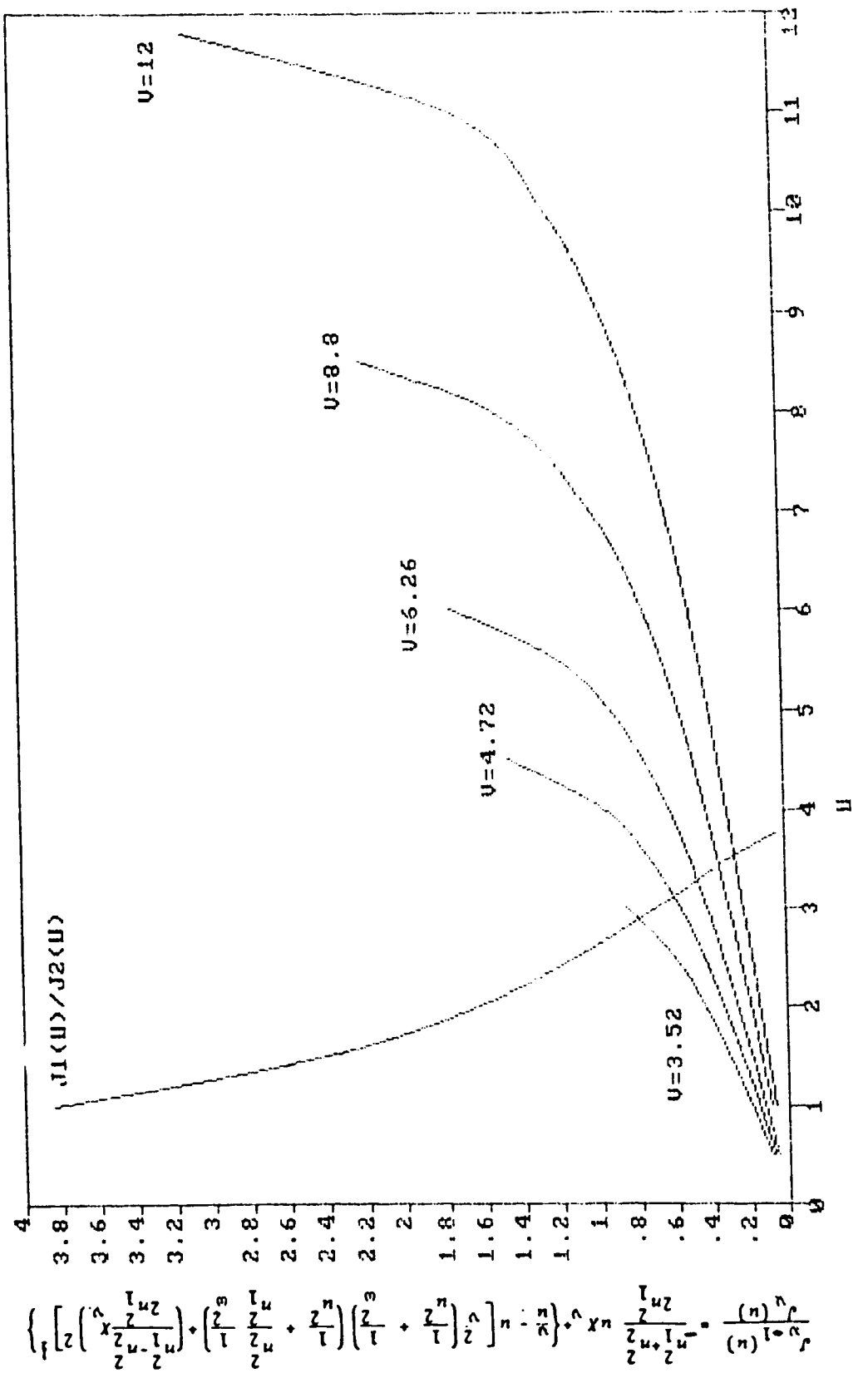

Figure 3-3. Plot of HE_{21} mode of a weakly guiding fiber (Eq. 3.22 for v=2,p=1).

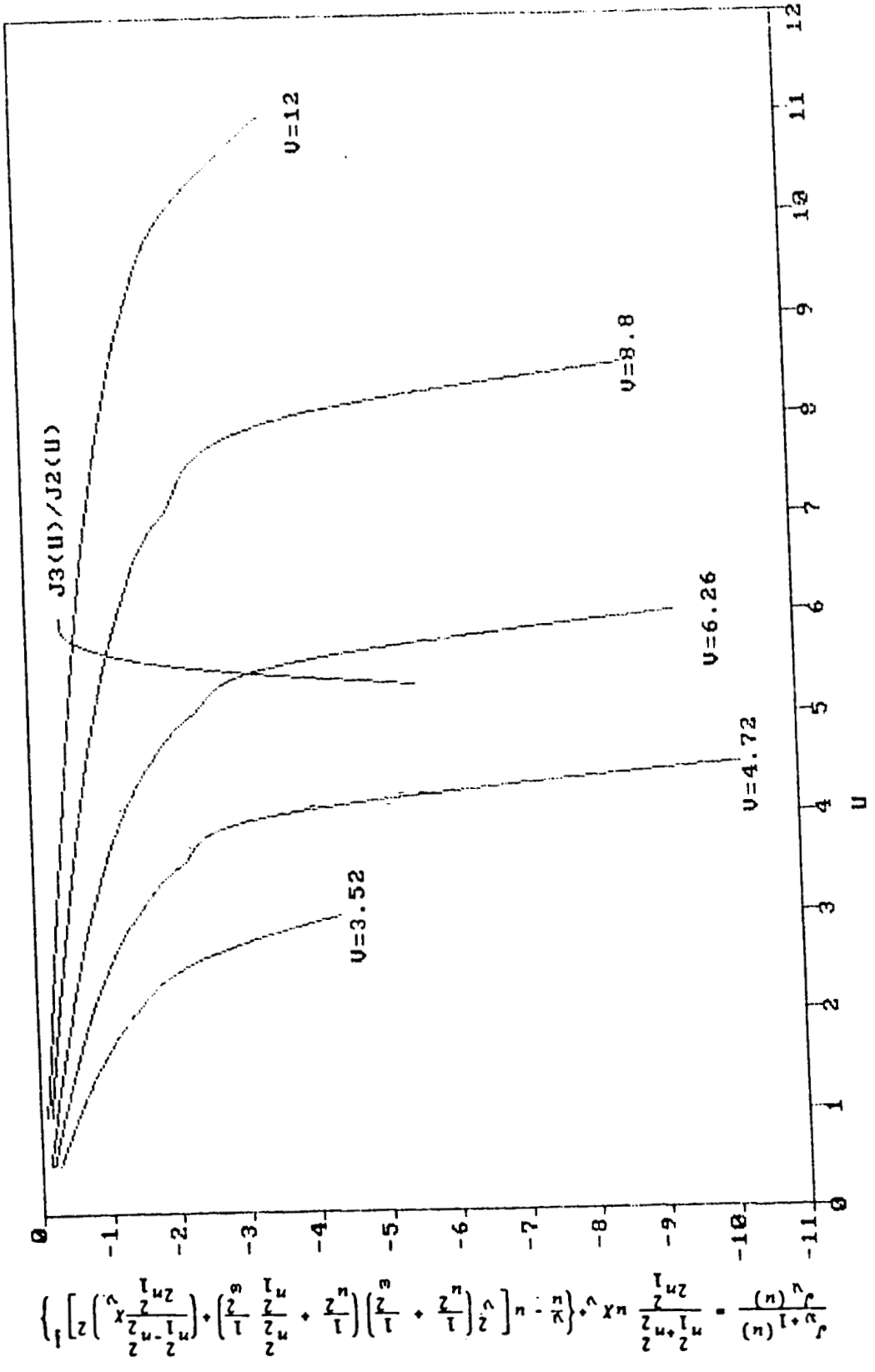

Figure 3-4. Plot of EH_{21} mode of a weakly guiding fiber (Eq. 3.23 for v=2, p=1).

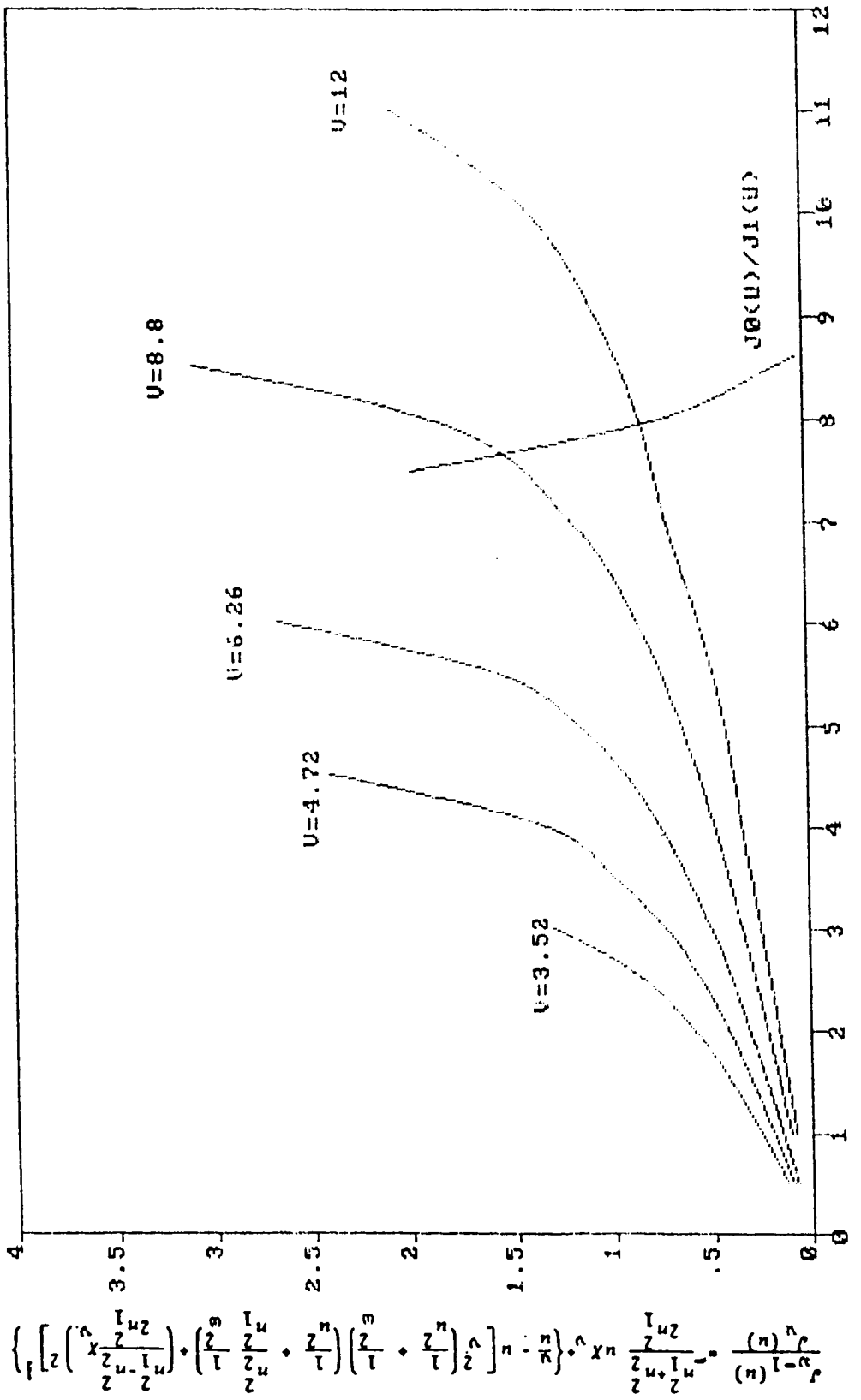

Figure 3-5. Plot of HE_{13} mode of a weakly guiding fiber (Eq. 3.22 for v=1,p=3).

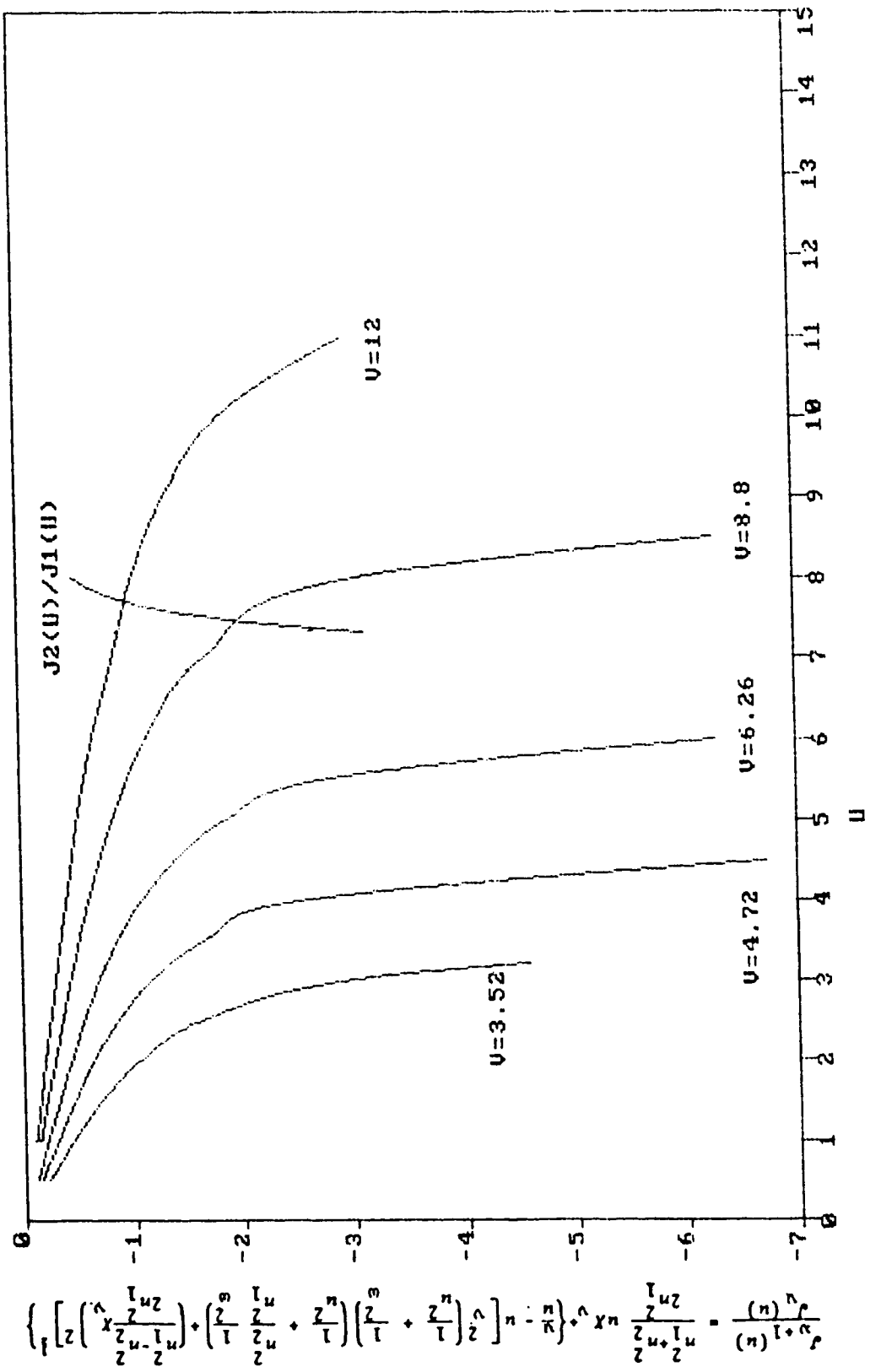

Figure 3-6. Plot of EH_{12} mode of a weakly guiding fiber (Eq. 3.23 for $\nu=1$, $p=2$).

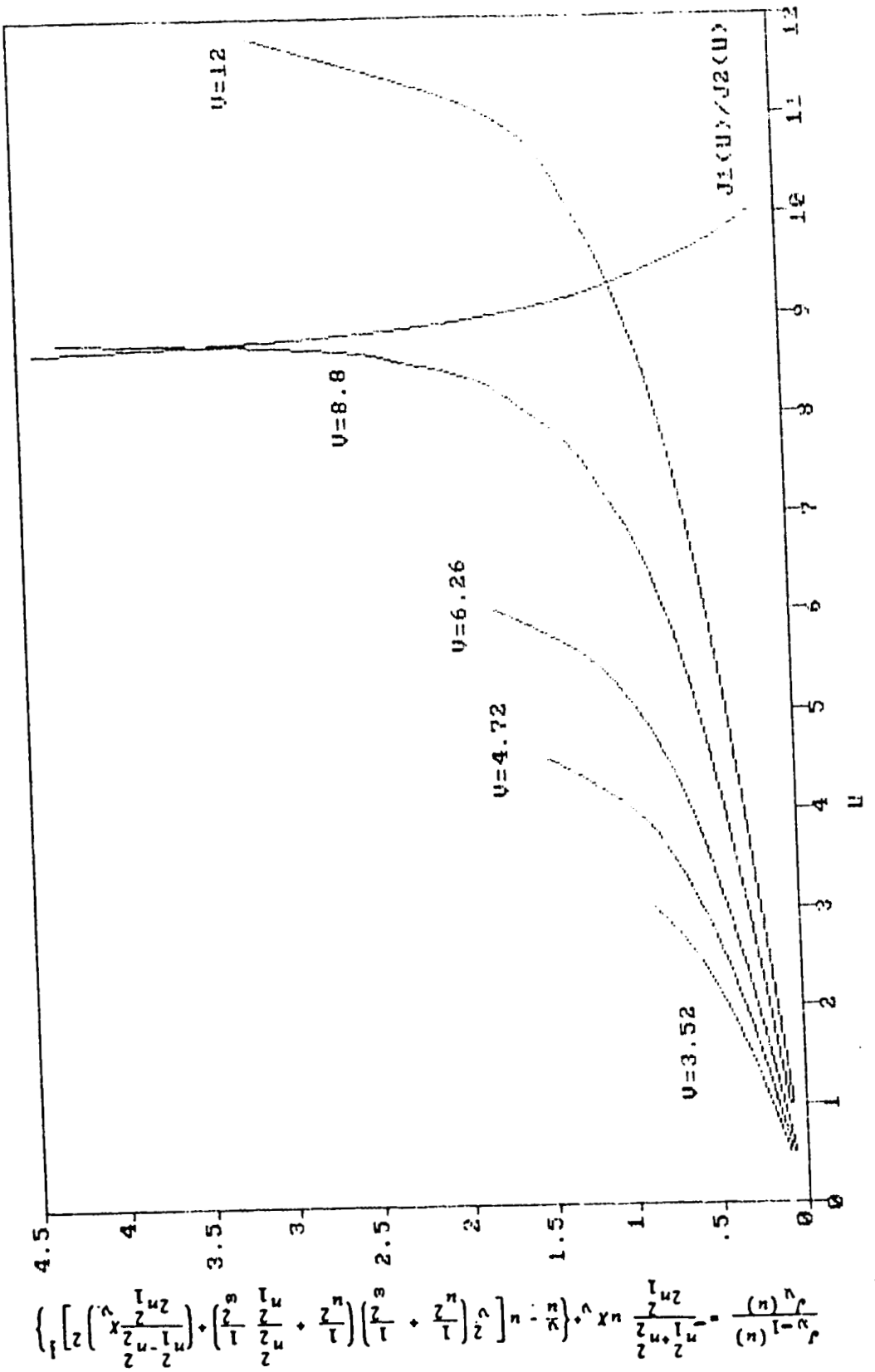

Figure 3-7. Plot of HE_{23} mode of a weakly guiding fiber (Eq. 3.22 for $\nu=2$, $p=3$).

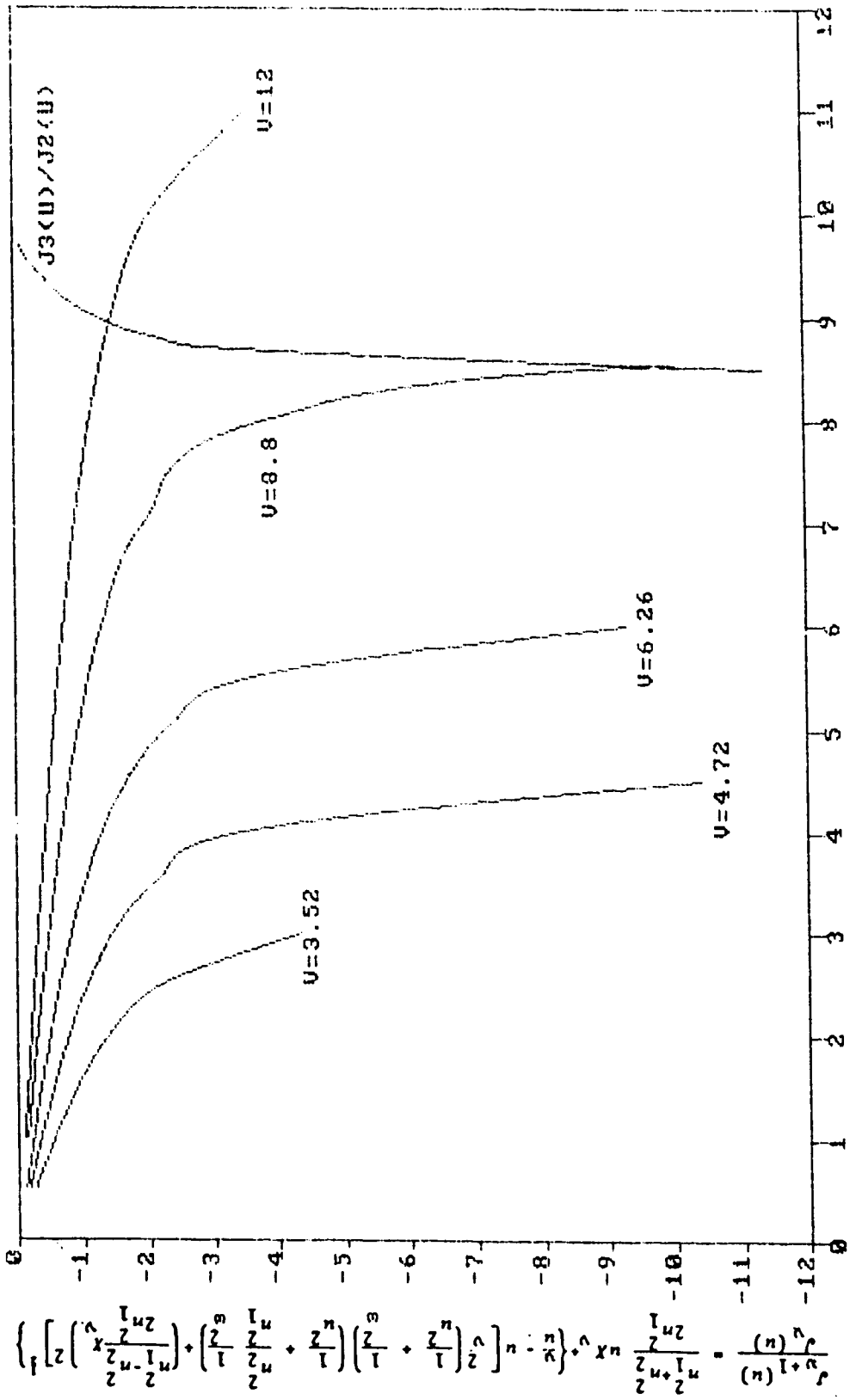

Figure 3-8. Plot of EH_{22} mode of a weakly guiding fiber (Eq. 3.23 for ν=2, p=2).

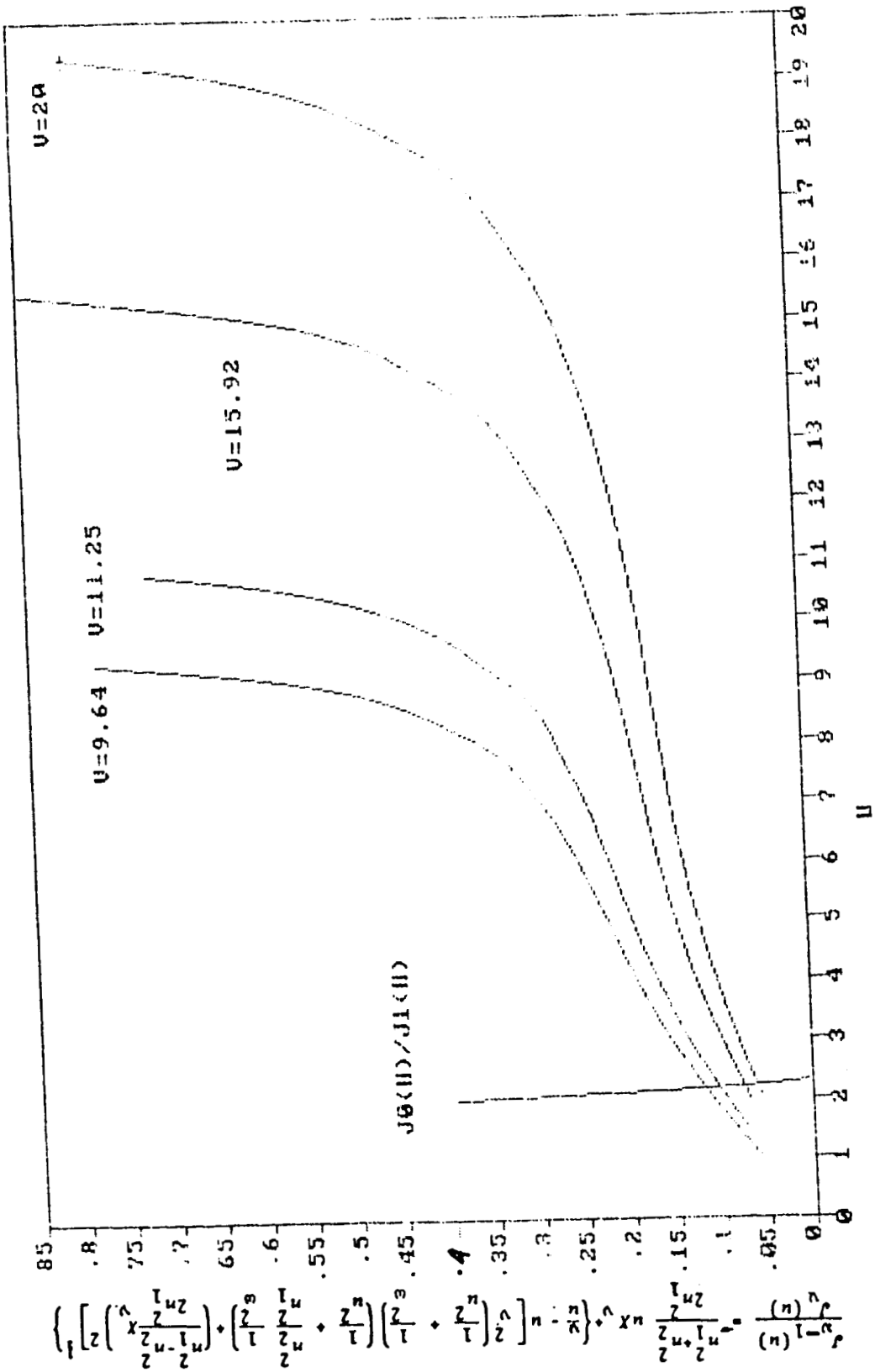

Figure 3-9. Plot of HE_{11} mode of an unclad fiber (Eq. 3.22 for v=1, p=1).

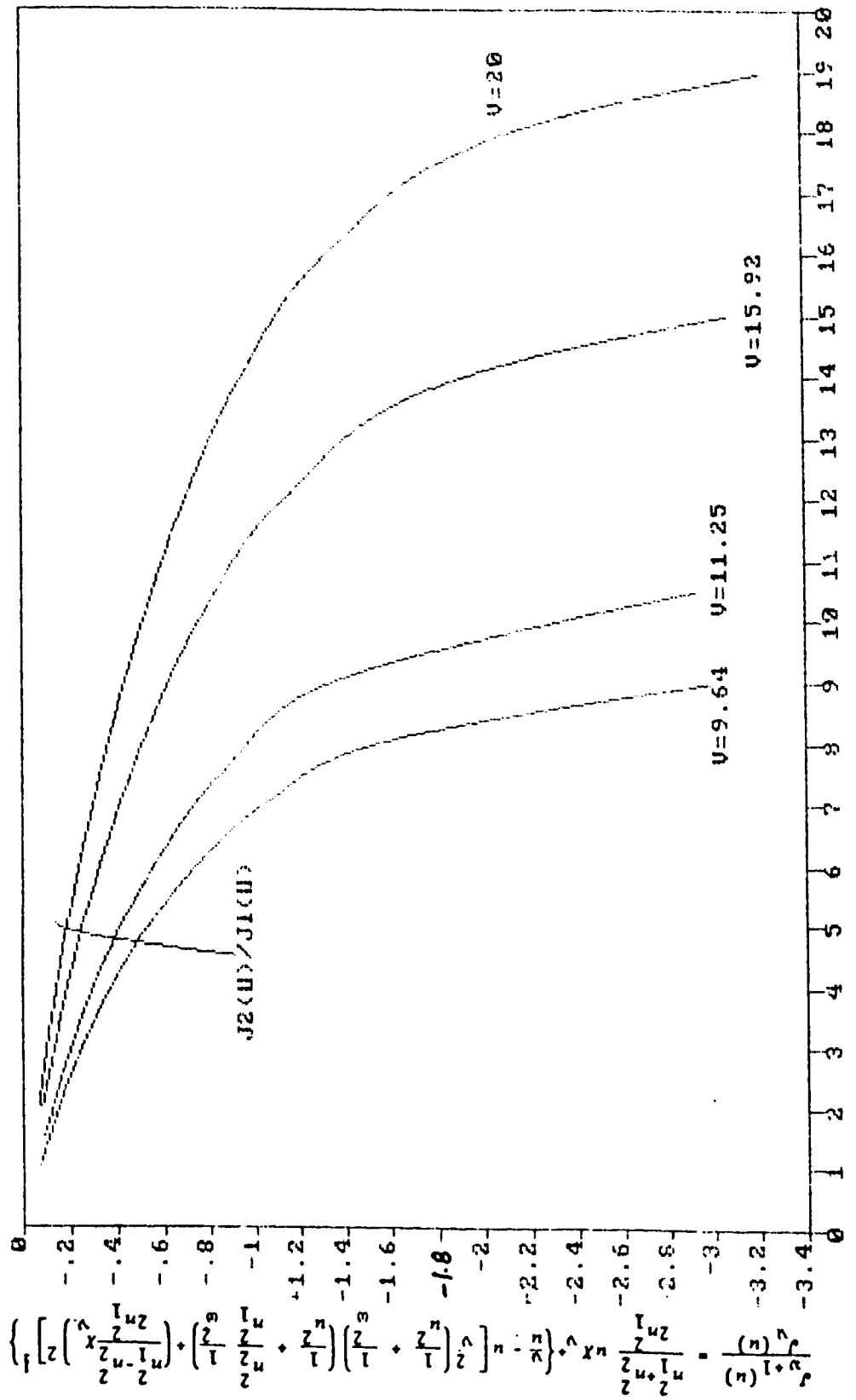

Figure 3-10. Plot of EH_{11} mode of an unclad fiber (Eq. 3.23 for ν=1,p=1).

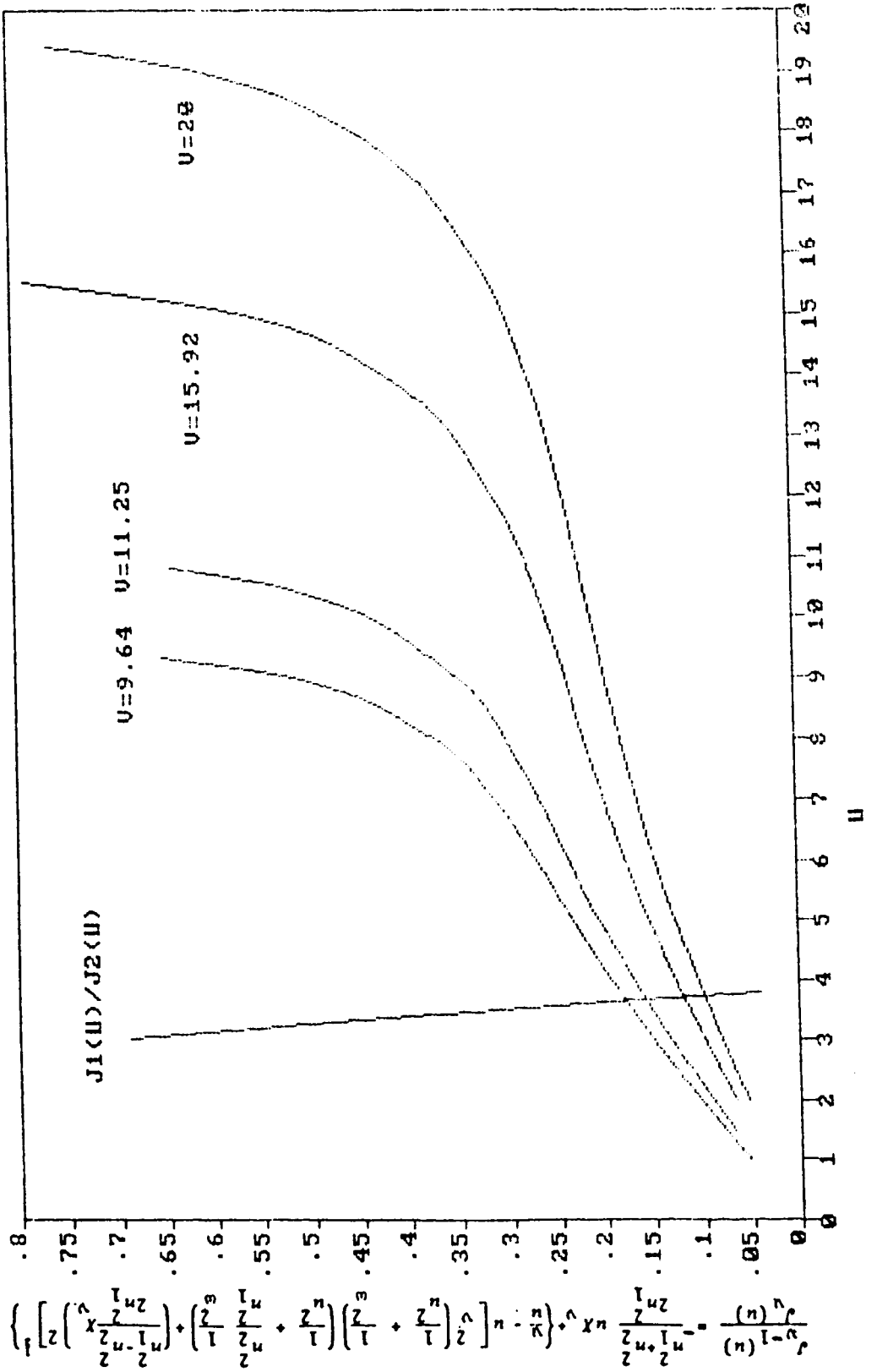

Figure 3-11. Plot of HE_{21} mode of an unclad fiber (Eq. 3.22 for ν=2, p=1).

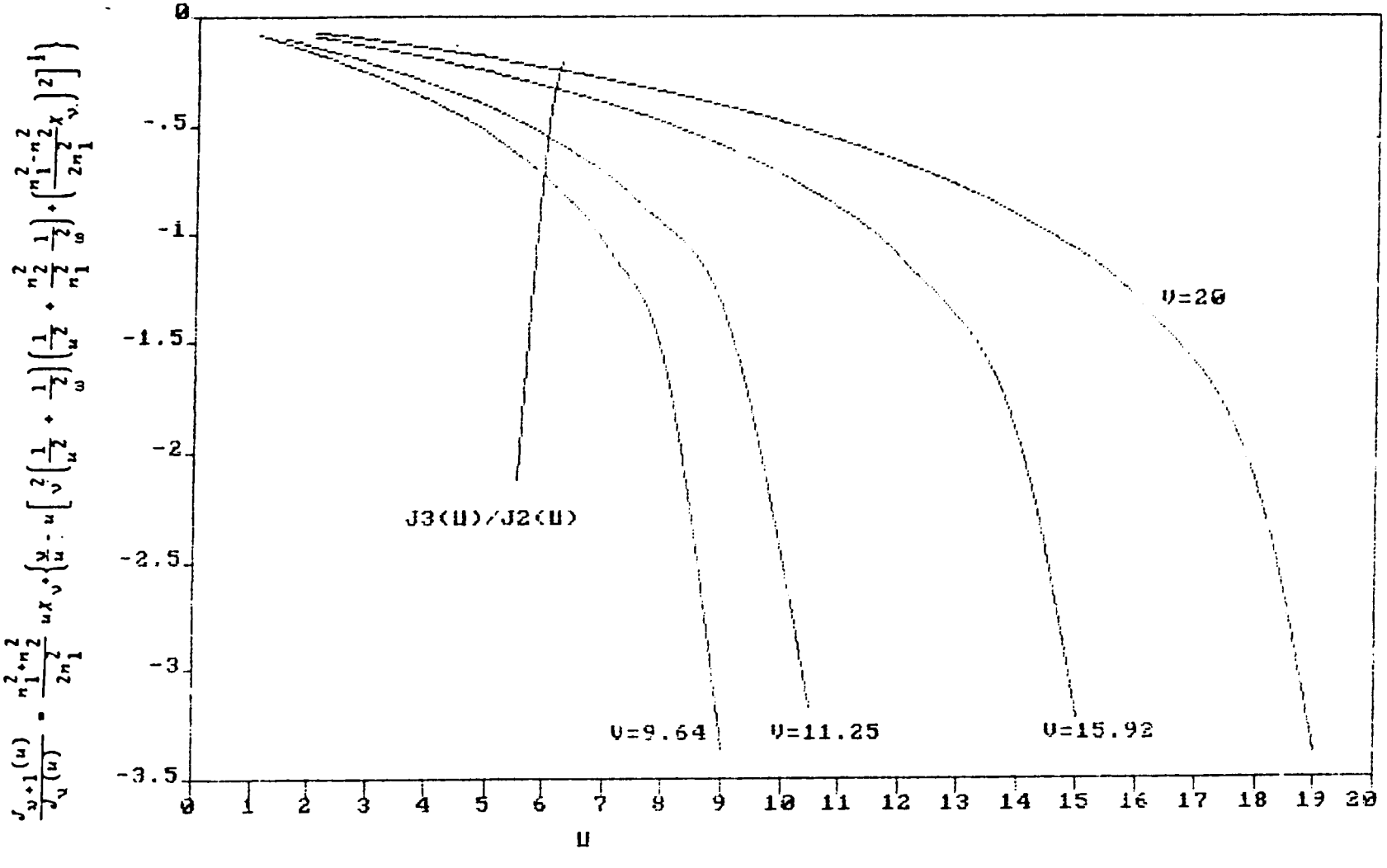

Figure 3-12. Plot of EH_{21} mode of an unclad fiber (Eq. 3.23 for $\nu=2$, $p=1$).

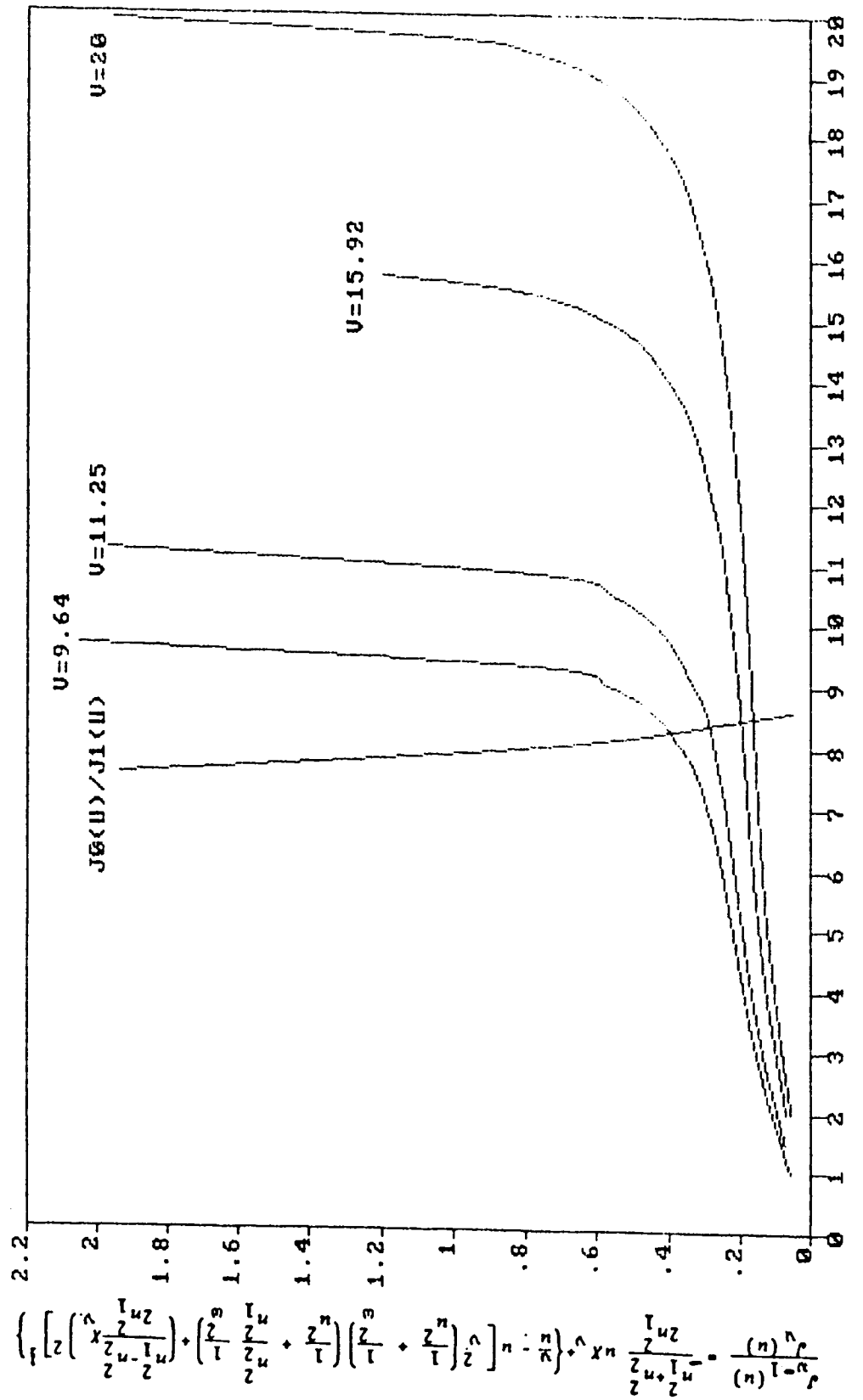

Figure 3-13. Plot of HE_{13} mode of an unclad fiber (Eq. 3.22 for v=1, p=3).

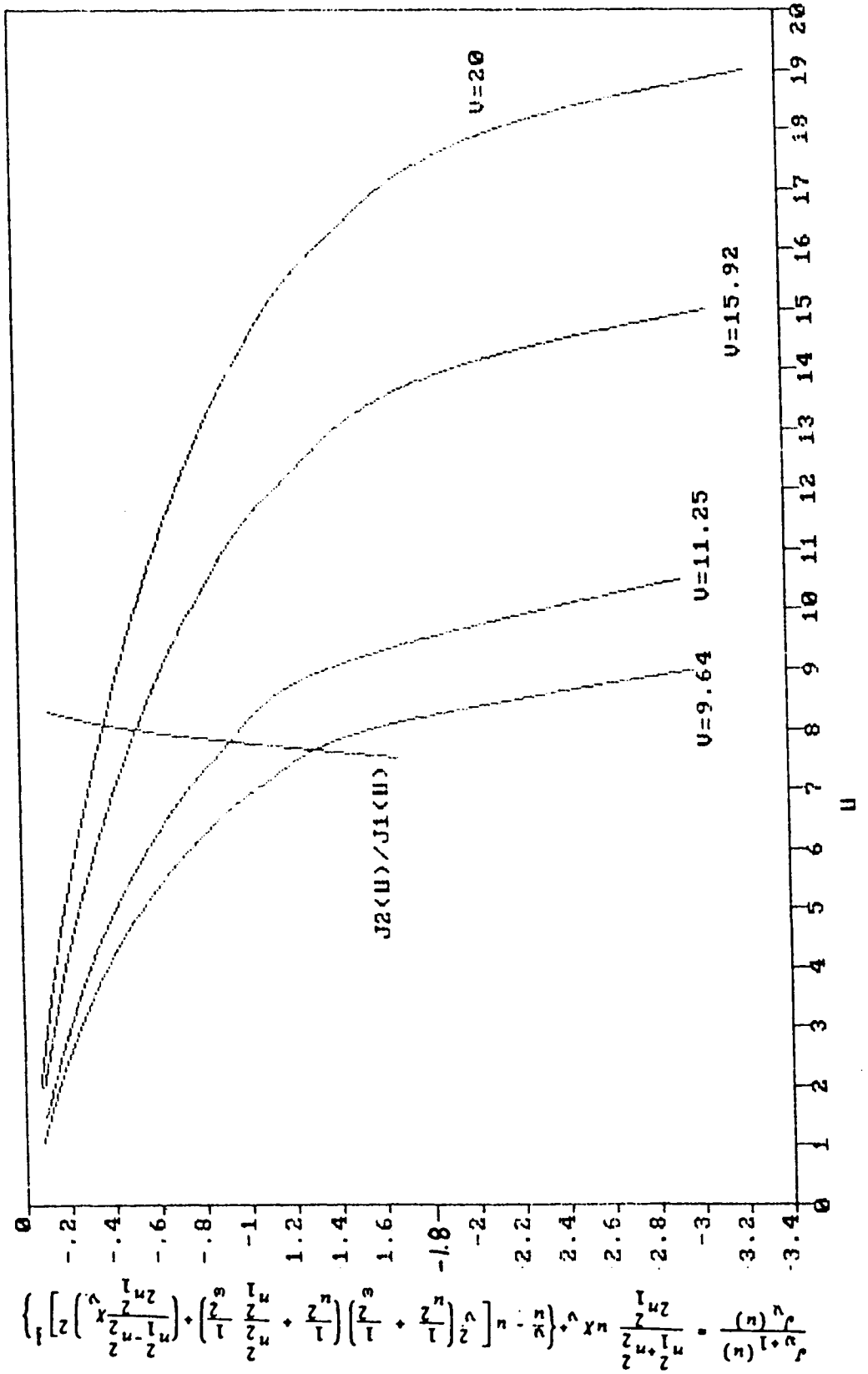

Figure 3-14. Plot of EH_{12} mode of an unclad fiber (Eq. 3.23 for v=1, p=2).

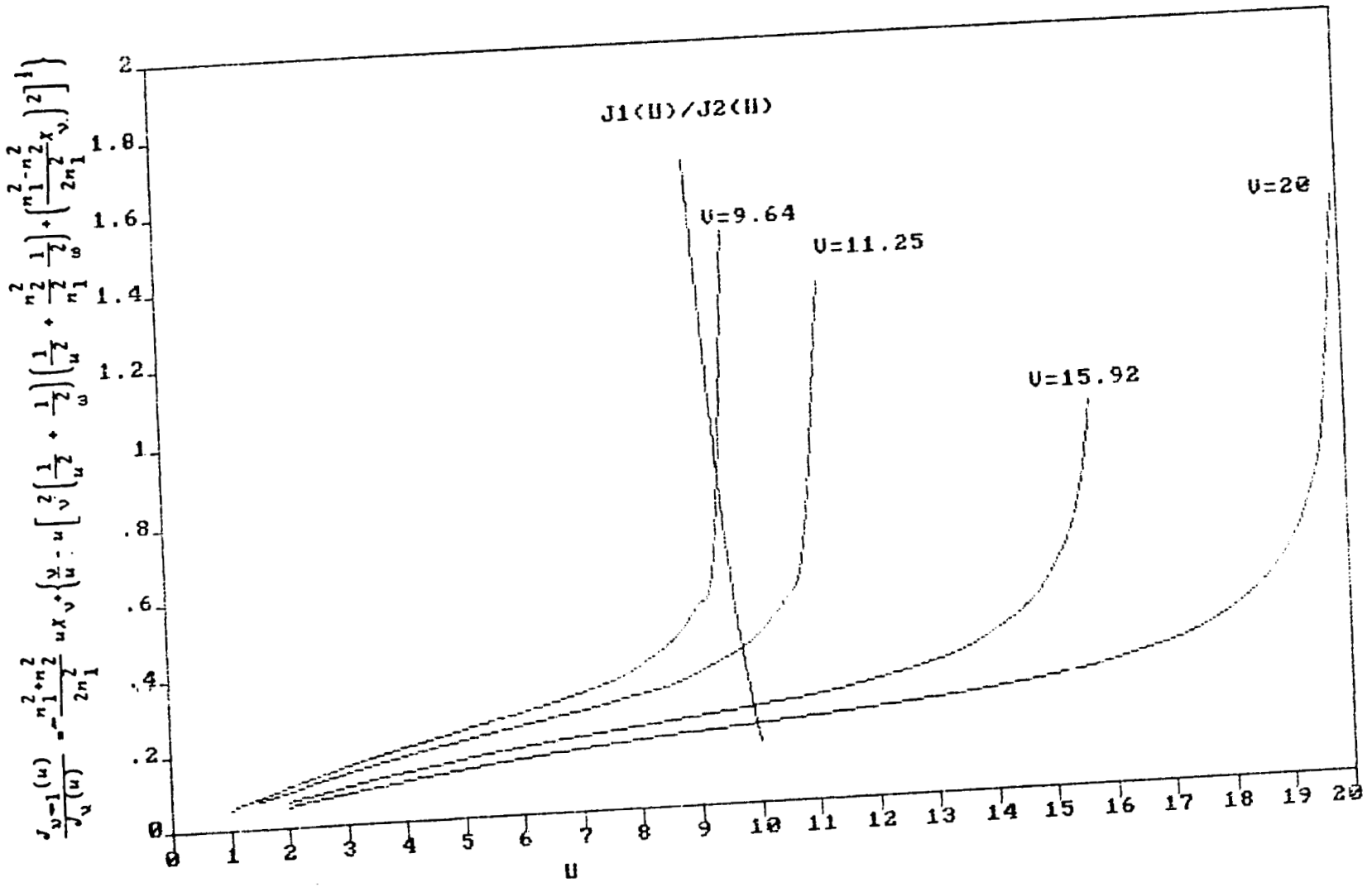

Figure 3-15. Plot of HE_{23} mode of an unclad fiber (eq. 3.22 for $\nu=2$, $p=3$).

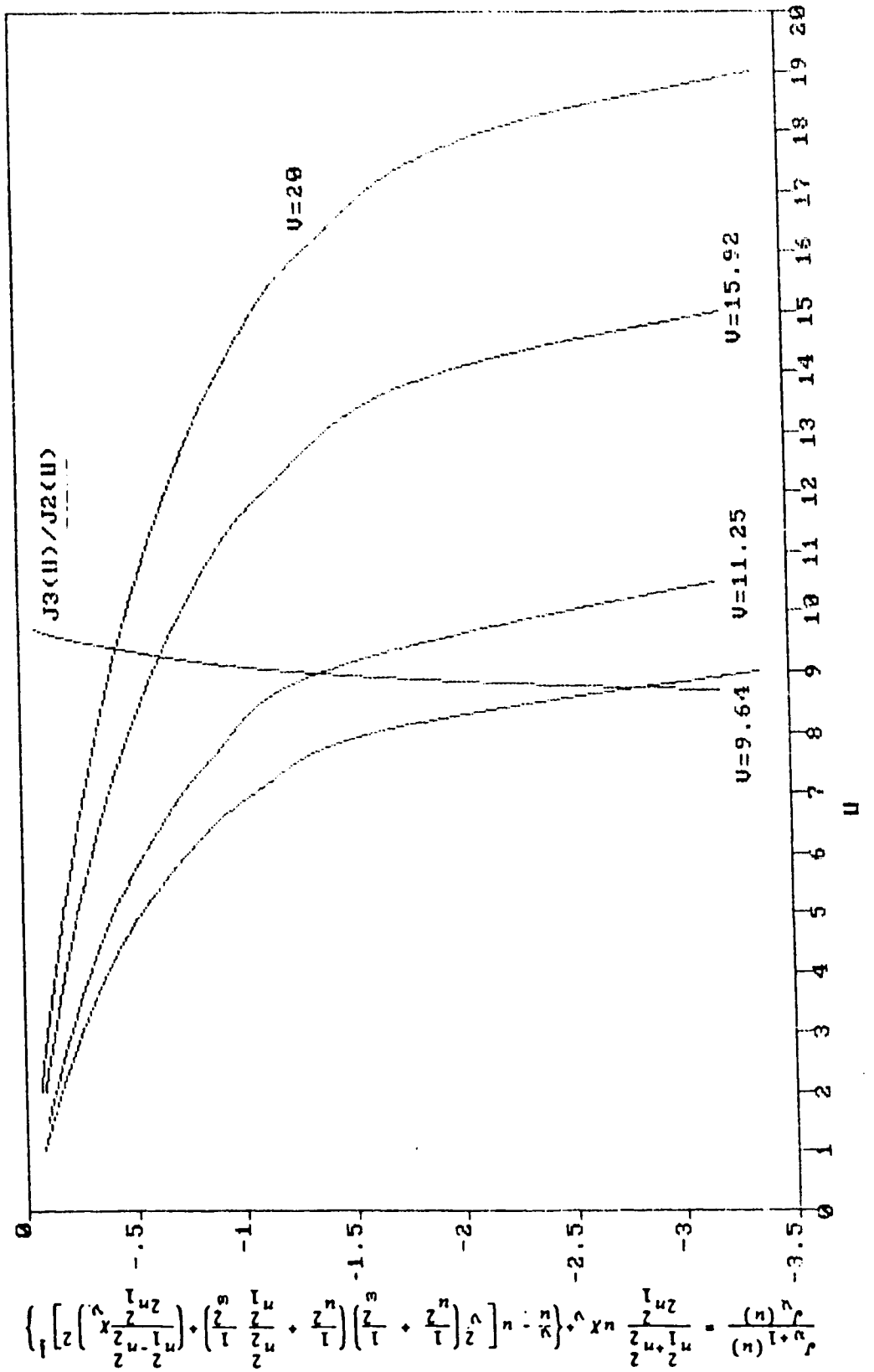

Figure 3-16. Plot of EH_{22} mode of an unclad fiber (Eq. 3.23 for v=2, p=2).

Table 3-1. Cutoff Conditions of HE and EH Modes.

Mode	*Cutoff* $W = 0$, $U = V$	$V = W = \infty$
HE_{1p}	$J_1(U) = 0$	$J_0(U) = 0$
EH_{vp}	$J_v(U) = 0$	$J_{v+1}(U) = 0$
HE_{vp} $(v > 1)$	$\frac{U}{(v-1)} \frac{J_{v-2}(U)}{J_{v-1}(U)} = \frac{-2\Delta}{1-2\Delta}$	$J_{v-1}(U) = 0$
Range of single-mode operation $0 < V < 2.405$		

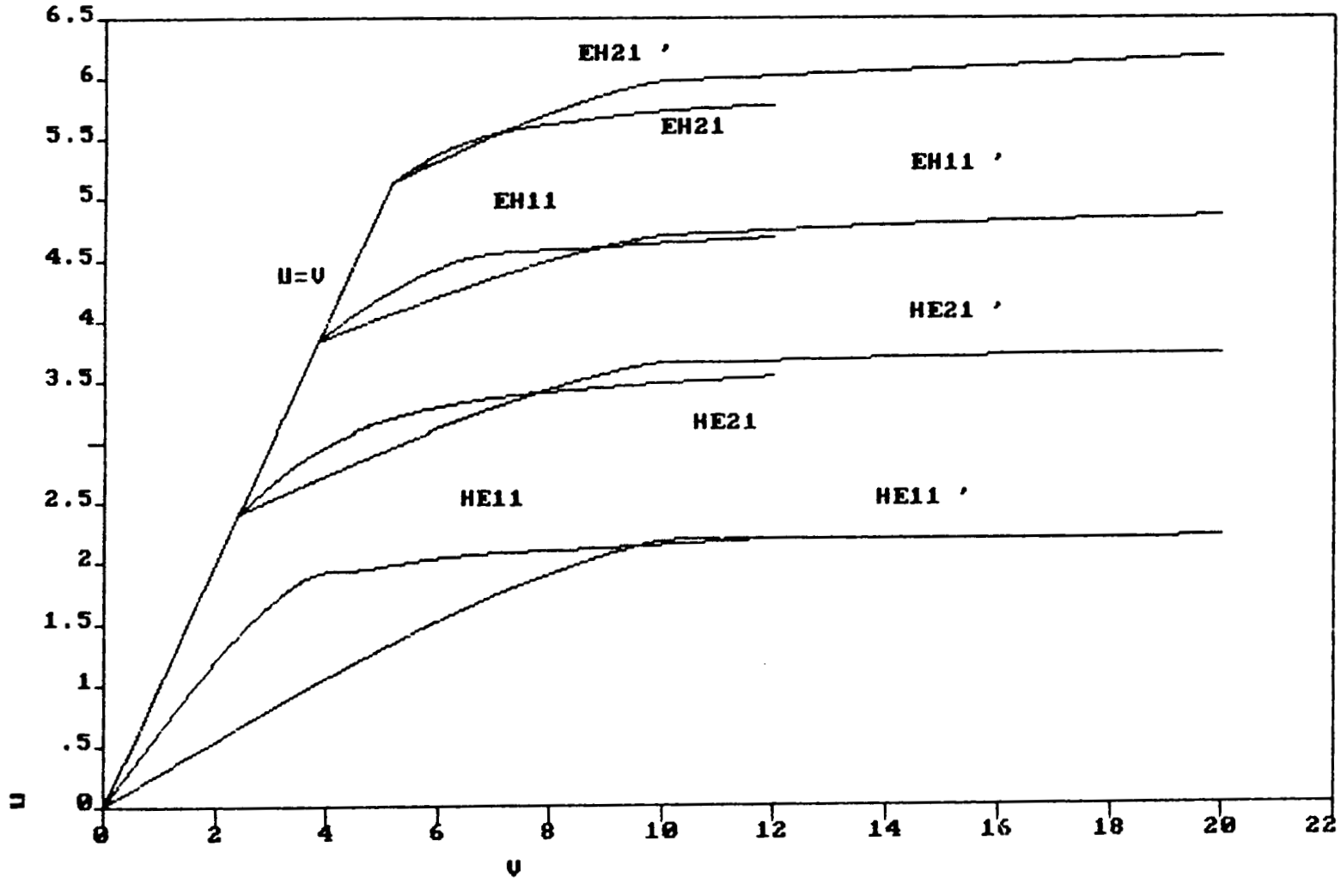

Figure 3-17. Numerical solution of HE and EH modes for weakly guiding and unclad infrared optical fibers.

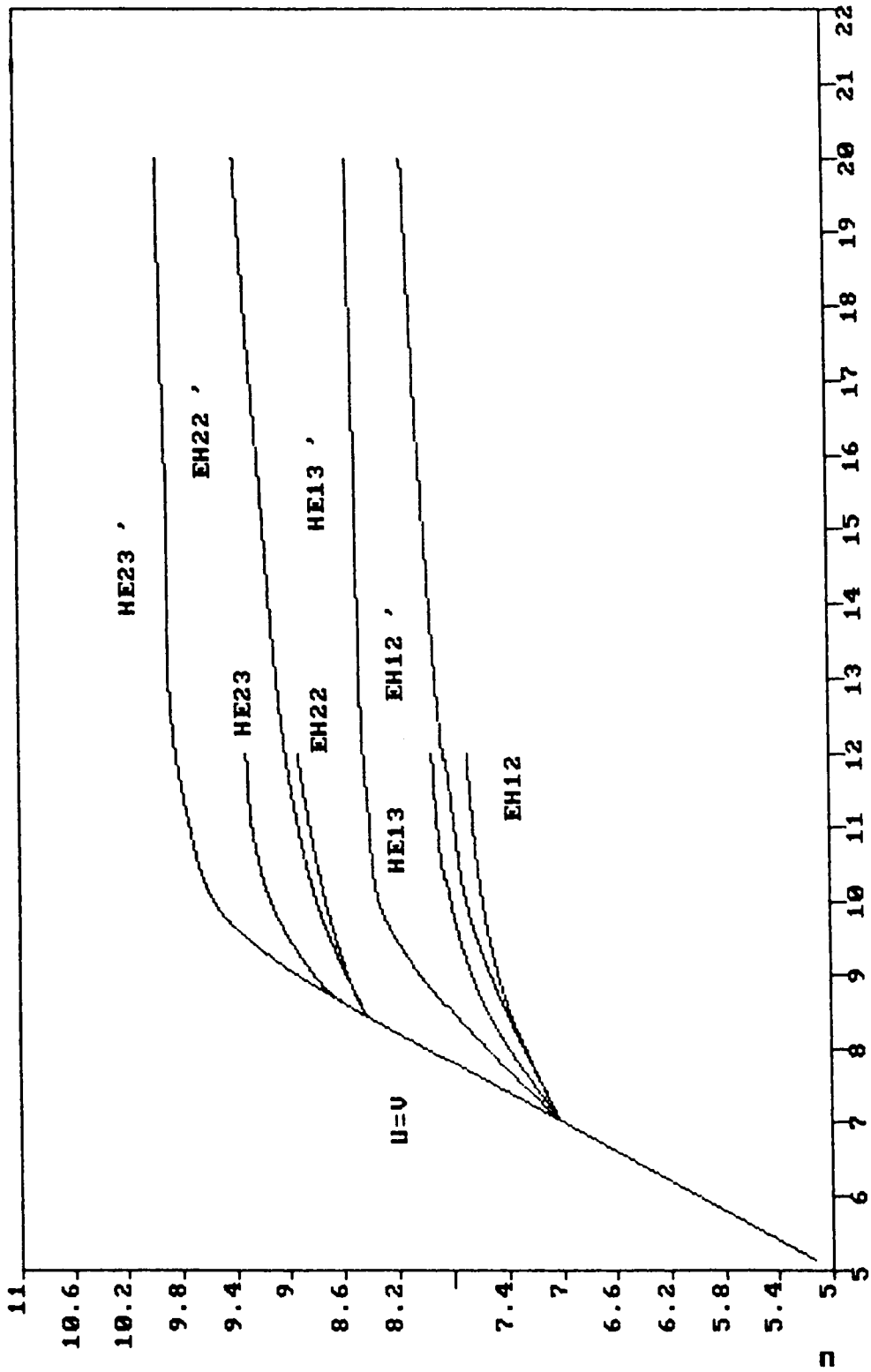

Figure 3-18. Higher order modes of weakly guiding and unclad infrared optical fibers.

CHAPTER FOUR

FIBER CHARACTERIZATION AND TESTING

4.1 Introduction

Since the current surge of activities in the research on IR fibers is the result of prospective application of these fibers in wide areas of medical practice, such as endoscopes and laser delivery system in surgery [4-7], initial requirements on fibers are therefor sufficient flexibility, power carrying capability, reasonably low loss, absence of toxicity, and chemical inertness for the purpose of replacing articulated arms and the use of natural body orifices for nonintrusive diagnostics and surgery. These can be satisfied with fibers of millimeter diameter and losses of fraction of a dB per meter. Fibers satisfying these conditions are now available. However, anticipating future pinpoint surgery with highly localized burns, the development of much smaller diameter and even single mode fibers is essential. Such requirements will conveniently match those in high speed IR communication systems which require fibers that have low loss, low dispersion and wide transparency band.

Table 4-1 shows pertinent fiber parameters. Those that concern our work are transparency band, brittleness, hardness, flexibility, stability or shelf life, and thermal behavior.

Table 4-1. Fiber Parameters

Property	Definition
Transparency Band:	The range of the spectrum permitting passage of radiation or particles.
Losses:	The actual power that is lost in transmitting a signal from one point to another through a medium.
Toxicity:	The kind and amount of poison or toxin possessed by a chemical substance.
Solubility:	The ability of a substance to form a solution with another substance.
Hygroscopicity:	The tendency of a material to absorb water from the atmosphere.
Refractive Index:	The ratio of the phase velocity of light in a vacuum to that in a specified medium.
Brittleness:	That property of a material manifested by fracture without appreciable prior plastic deformation.
Hardness:	The resistance of a metal or other material to indentation, scratching, abrasion, or cutting.
Flexibility:	The quality or state of being able to be flexed or bent repeatedly.
Crystal Structure:	The arrangement and interrelation of the parts of the crystal.
Photosensitivity:	The ability of the material to preserve its characteristics when illuminated with light.
Shelf-Life:	The time that elapses before stored materials or devices become inoperative or unusable due to age or deterioration.
Stability:	The capability of the material to retain its characteristics in an adverse environment.
Disperson::	The rate of change of refractive index with wavelength or frequency at a given wavelength or frequency.
Thermal Behavior:	The behavior of a property of a material in an adverse environment.

Transparency is the ability of the fiber to transmit optical signals over a specific range of the spectrum. The transparency band of an optical fiber is determined by the materials used to fabricate such a fiber. There are two types of IR materials usually used in fabricating IR optical fibers, and these are heavy metal polycrystalline and chalcogenide glass optical fibers. Polycrystalline fibers have wider transparency band as compared to chalcogenide glass fibers.

Transparency band is significant to us, because a fiber that transmits over a wide range of the spectrum is compatible with the tunable diode laser (TDL) that has a wavelength tunability range from 3 μm to 30 μm. Therefore it is necessary to select a material having a MID to FAR infrared window. This is done by choosing a material that has as large a band gap as possible in order to restrict the electronic band edge limited by Rayleigh scattering and OH ions (resulting from the fabrication of IR fibers) to high photon energies of the short wavelength side, and phonon bands should be located at a sufficiently long wavelength so that multiphonon absorption that occurs when incident light of sufficient photon energy is absorbed by a valence electron and moves into the conduction band will be minimized in the mid and far IR. This usually calls for heavy atoms and weak bonding forces. Since anions are usually the lighter of the constituent atoms, it is possible to predict that the transparency of a compound will depend on the atomic weight of the anions it contains.

Thus, an increase in IR transmission is to be expected with a progression down the VIB or VIIB groups of the periodic table.

The utilization of still heavier groups is, to some extent, counter productive, since the weaker bonding that occurs due to the existance of weak interaction between atoms to form molecules would result in too deleterious an effect on mechanical properties. Thus, heavy covalent materials tend to be weak and brittle, often water-soluble materials. Clearly such properties are imposing intolerable constraints upon mass fiber production processes. There is therefore a need for some degree of compromise between conflicting optical and mechanical performance characteristics.

The relative merits of glass or crystalline states are complex and again involve conflicting mechanical and optical parameters. Generally speaking, it appears to be harder to synthesize a glass as cut off wavelengths increase since those materials which are glass formers become weaker, less stable and more difficult to fabricate. This effect is illustrated in Figure 4-1 [29] where the IR transmission spectra of a number of potential glass fiber materials are shown. Table 4-2 shows the transmission range of crystalline IR fibers. Silica and other mechanically strong glasses cut off in the near IR whereas ionic flourides having slightly decreased strengths, transmit into the mid IR. Classical chalcogenides are far weaker having typical Vickers hardness numbers around 200 but transmitting

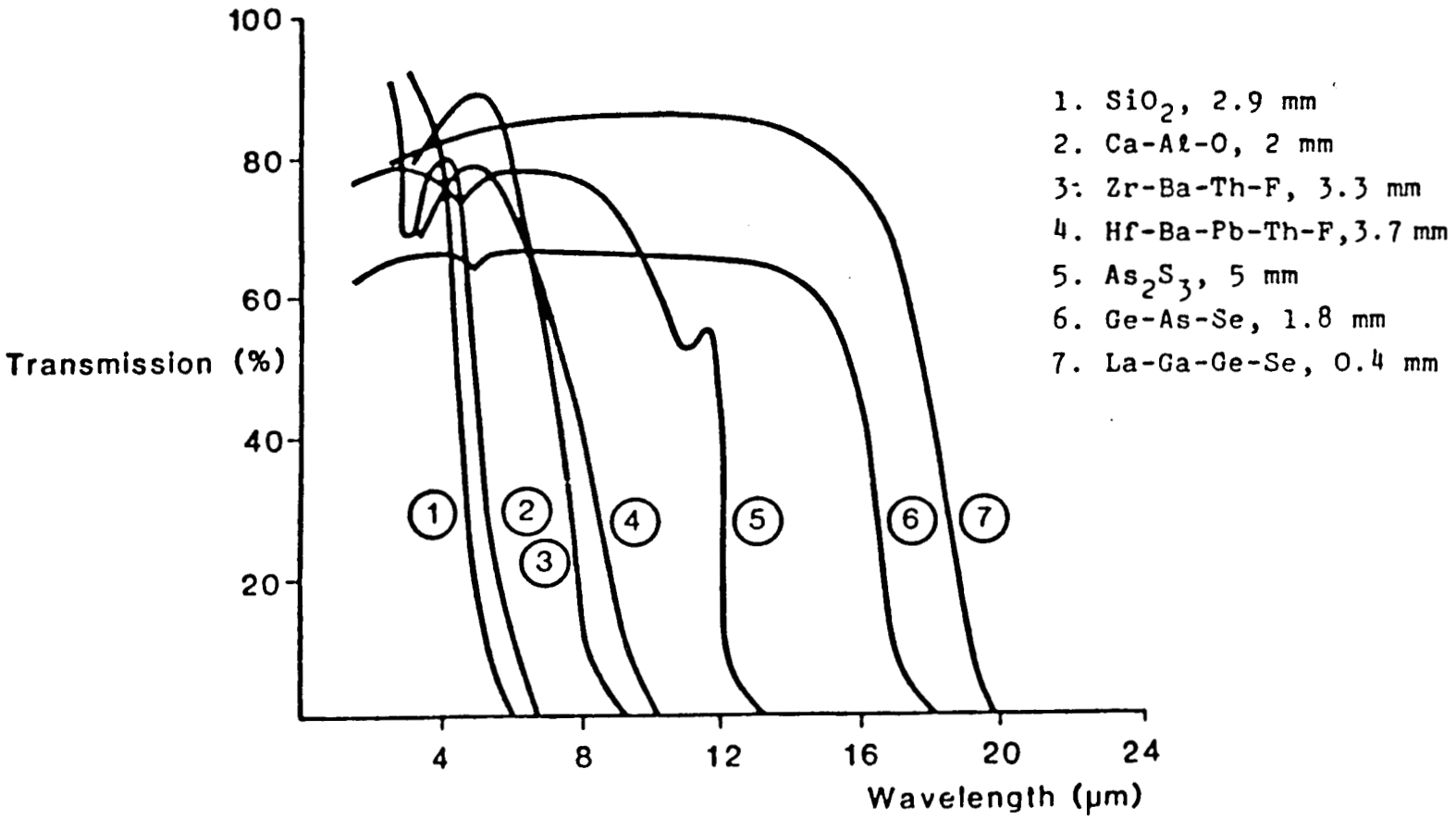

Figure 4-1. Infrared transmission spectra of a number of potential fiber materials.

Table 4-2. Transmission Range of Crystals.

Material	Wavelength (microns) 0.1–0.2	0.2–5	5–10	10–20	20–30	30–35	35+
Quartz		X					
LiF	X	X					
CaF_2	X	X	X				
SrF_2		X	X				
BaF_2		X	X				
NaCl		X	X	X			
KCl		X	X	X			
NaI		X	X	X			
KBr		X	X	X			
AgCl		X	X	X			
TlCl		X	X	X	X		
KRS-6		X	X	X	X		
AgBr		X	X	X	X		
TlBr		X	X	X	X		
CsBr		X	X	X	X	X	
KRS-5		X	X	X	X	X	
CsI		X	X	X	X	X	X

across the whole MID IR waveband, and rare-earth-modified chalcogenides are transparent to around 20 μm but are only able to be formed in very small amounts by rapid quenching techniques.

Trade-offs of the properties will exist: for example, KRS-5 (thallium chlorobromide) is less water-soluble than pure TlCl but, considering flexibility, it is harder than either TlCl or TlBr. Specifically, KRS-5 is relatively insoluble in water and non-hygroscopic, Table 4-3 shows the solubilities of crystals in water. However, thallium containing compounds such as KRS-5 are toxic since they contain a heavy metal.

Table 4-3. Solubility of crystals in water.

Material	g/100g of Water	Material	g/100g of Water
Quartz	Insoluble	KRS-6	< 0.32
AgBr	12×10^{-6}	TlCl	0.32
AgCl	1.5×10^{-4}	KCl	34.7
CaF_2	1.31×10^{-3}	NaCl	36.0
SrF_2	1.17×10^{-2}	KBr	65.2
KRS-5	$<4.76 \times 10^{-2}$	CsI	85.5
TlBr	4.76×10^{-2}	CsBr	124.0
BaF_2	0.12	NaI	185.0
LiF	0.27		

Hardness and brittleness are important mechanical properties of IR fibers, as they represent the "tensile strength." Hardness is defined as the resistance of a metal or material to indentation, scratching, abrasion, or cutting. It is measured in MOH. This is an arbitrary scale used to describe the hardness of several mineral substances on a scale of 1 through 10.

Tensile strength is defined as the maximum stress a material subjected to a stretching load can withstand without tearing. It is measured in N/m^2 or Kg/mm^2. Tensile strength depends strongly on the fiber grain size. Yield and ultimate strength are greater for small grain size fibers, decreasing as grain size increases. The bending yield point and tensile strength were determined from the lateral bending of samples [30]. It was established that the character of the deformation of the samples is dictated by the orientation of their longitudinal axis, and the nature of their fracture is dictated by the orientation of the planes in each sample as shown in Table 4-4 [30]. Table 4-5 shows the compressive yield point and tensile strength of KRS-5 and KRS-6 crystals [30]. Compressive yield point is defined as the point at which the fiber begins to crack with further compression. Just as in the bending case, the nature of the compressive deformation is determined by the crystallographic orientation of the sample. Microhardness is defined as the hardness of microscopic areas of a metal or alloy. Microhardness for the same materials are listed in Table 4-6 [30].

Brittleness is that property of a material manifested by fracture without appreciable prior plastics deformation. KRS IR optical fibers are very brittle as compared to other IR fibers such as polycrystalline silver halide and glass chalcogenide. Because the molecular compounds of KRS-5 consist of two or more stable species held together by weak forces.

Table 4-4. Bending yield point and tensile strength of KRS-5 and KRS-6 single crystals.

Crystal	Crystallographic orientation: Longitudinal axis	Plane A	Plane B	Yield point, kg/mm^2	Tensile strength, kg/mm^2
KRS-5	{100}	{100}	{100}	-	12.3
	{100}	{110}	{110}	-	12.1
	{110}	{100}	{110}	4.1	-
KRS-6	{100}	{100}	{100}	-	11.0
	{100}	{110}	{110}	-	10.8
	{110}	{100}	{110}	3.2	-

Table 4-5. Compressive yield point and tensile strength of KRS-5 and KRS-6 crystals, kg/mm^2.

Crystal	KRS-5			KRS-6		
Crystallographic orientation	[100]	[110]	[111]	[100]	[110]	[111]
Our data	(24)*	7	6	(5.2)*	3.2	1.4
From data of [13]	-	-	-	-	1.31	-
From data of [14]	(18.2)*	-	-	-	-	-

* Tensile strength values are enclosed in parentheses, yield point values are not.

Table 4-6. Microhardness of KRS-5 and KRS-6 crystals.

Crystal	Orientation	Microhardness, kg/mm^2		
		Our data[a]	From data of [1][b]	From data of [15][a]
KRS-5	[100]	36.2	39.8	39.4
	[110]	32.5	33.2	38.0
	[111]	27.9	-	40.8
KRS-6	[100]	30.1	38.5	-
	[110]	26.8	29.9	-
	[111]	25.4	-	-

[a] 10 g load for 15 seconds

[b] From Knupp

Flexibility is an important practical consideration for optical fibers. It is defined as the quality or state of being able to be flexed or bent repeatedly. Materials with high elasticity modulus are very flexible. This is caused by the lack of dislocations in the material's atomic structure. Dislocations are lattice defects quite unique in that their movement produces the plastic deformation of crystals, and that the mechanical properties of crystals are largely determined by the behavior of dislocations in crystals. In addition, width to length ratio would affect the flexibility of the fiber. Modulus of elasticity is defined as the ratio of the increment of some specified form of stress to the increment of some specified form of strain. Flexibility is measured by bending the fiber in various degrees. A flexible fiber can be bent without any fracture. The degree

of flexibility depends on the atomic structure of the material. Glass fibers do not contain dislocations in their atomic structure, since dislocations exist in crystals only caused by defects and larger percentage of covalent bonds than ionic bonds exist in glass structure than in crystal structure. The presence of dislocations will interrupt the atomic regularity. Thus, halides are more flexible compared to glass fibers since they exhibit dislocations in their atomic structure. It has been observed that the flexibility of certain crystalline fibers can be enhanced at elevated temperatures; KRS-5 becomes "plastic-like" at 250^{0}C to 350^{0}C. Because at this temperature range the elasticity is high enough for KRS-5 (ThBr) to become very flexible. This fiber can be bent into almost any arbitrary configuration, which it retains after it cools to room temperature [32].

One of the interesting properties of optical fibers is stability (long shelf life). Stability is defined as the capability of the material to retain its characteristics in an adverse environment, for example, extreme temperature. Fibers with short shelf life is of little practical use. Stability occurs due to the growth of grain size of the fiber resulting from the temperature gradient.

Extrusion is used to produce optical fibers. Extrusion is normally done on preform near the melting point so that the material flows freely as shown in Figure 4-2. Melting point is defined as the temperature at which a solid of a pure substance changes to a liquid. The melting temperatures of selected IR crystals are listed in Table 4-7. A concern with preformed crystal (polycrystalline materials) is long term grain

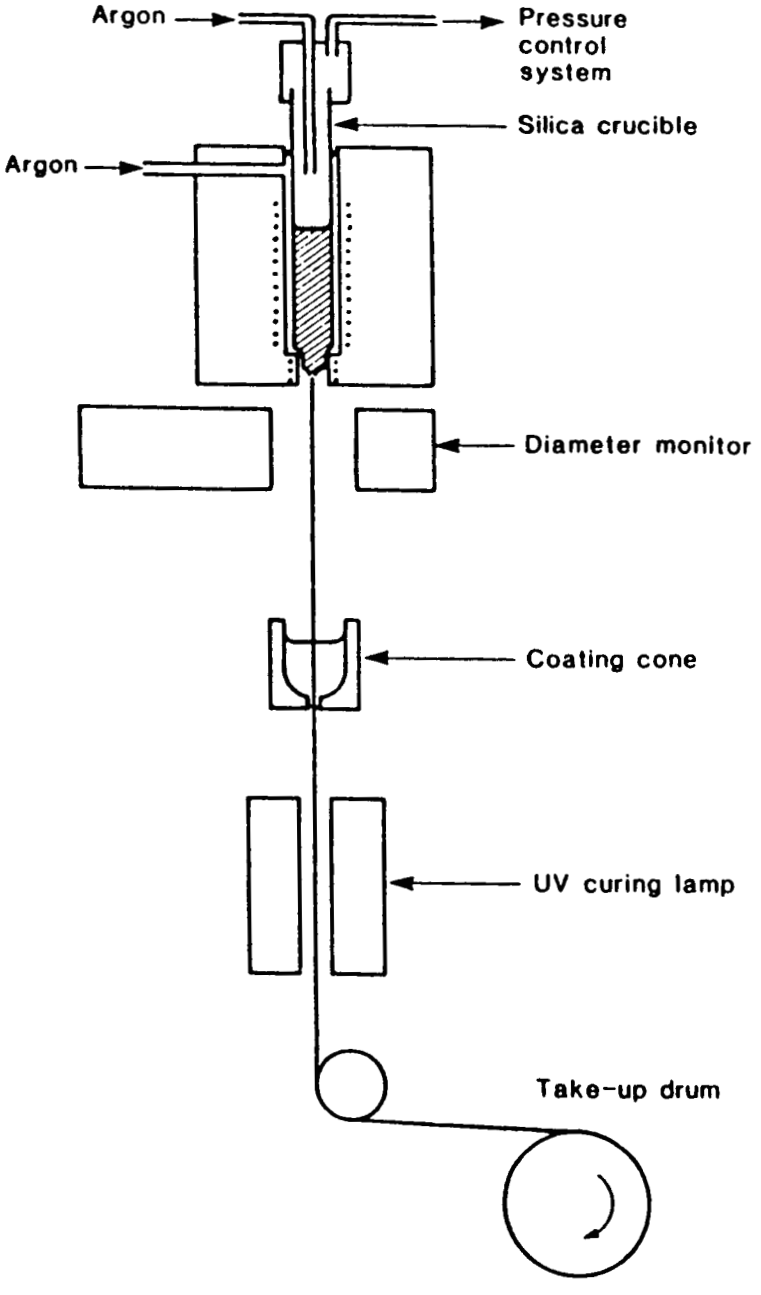

Figure 4-2. Setup of fiber drawing

size growth since the grain size is a function of the extrusion temperature. Therefore, mechanical properties such as tensile strength will be related to extrusion temperature. For example, the higher the temperature, the larger the grain size, the lower the tensile strength. For this reason it is very important for us to test IR optical fibers at LN_2 temperature since these fibers will be butted to the tunable diode laser (TDL), which is cooled with the same temperature.

Table 4.7. Melting points of selected optical crystals

Material	Temperature (^{o}C)	Material	Temperature (^{o}C)
Quartz	1610	CsBr	636
SrF_2	1450	CsI	621
CaF_2	1360	TlBr	460
BaF_2	1280	AgCl	455
LiF	942	AgBr	432
NaCl	801	TlCl	430
KCl	776	KRS-6	423
KBr	730	KRS-5	414
NaI	651		

4.2 Data on Commercial IR Fibers

There have been several experimental infrared materials demonstrating transmission in the midrange infrared (8-12 μm). now, for the first time, materials are becoming available for actual use in industrial applications, sensors, and applications where flexibility is important. Clad and unclad fibers of heavy metal silver and thallium halide polycrystalline and chalcogenide glass are being marketed in sheathed, single fiber form.

Silver halide fibers (AgCl) of 0.1 mm diameter have been drawn using extrusion method by Asahi Glass [33]. Table 4-8 shows some of the data supplied to us. Figure 4-3 illustrates the attenuation versus wavelength for this fiber [33].

Table 4-8. Data of silver halide fiber (AgCl).

Length:	Max. 300 cm (100 cm normal)
Diameter:	Fiber - 1 mm, cable - 6 mm
Usage Temp.:	-10° $-60^{\circ}C$ (for more than $60^{\circ}C$, cooler is needed)
Minimum Bending Radius:	3 cm (static), 20 cm (repeating)
Strength:	13 kg
Focus Lense:	Silicon Crystal (dia. 8 mm, f=10mm)
Infrared Sensor:	For consideration.

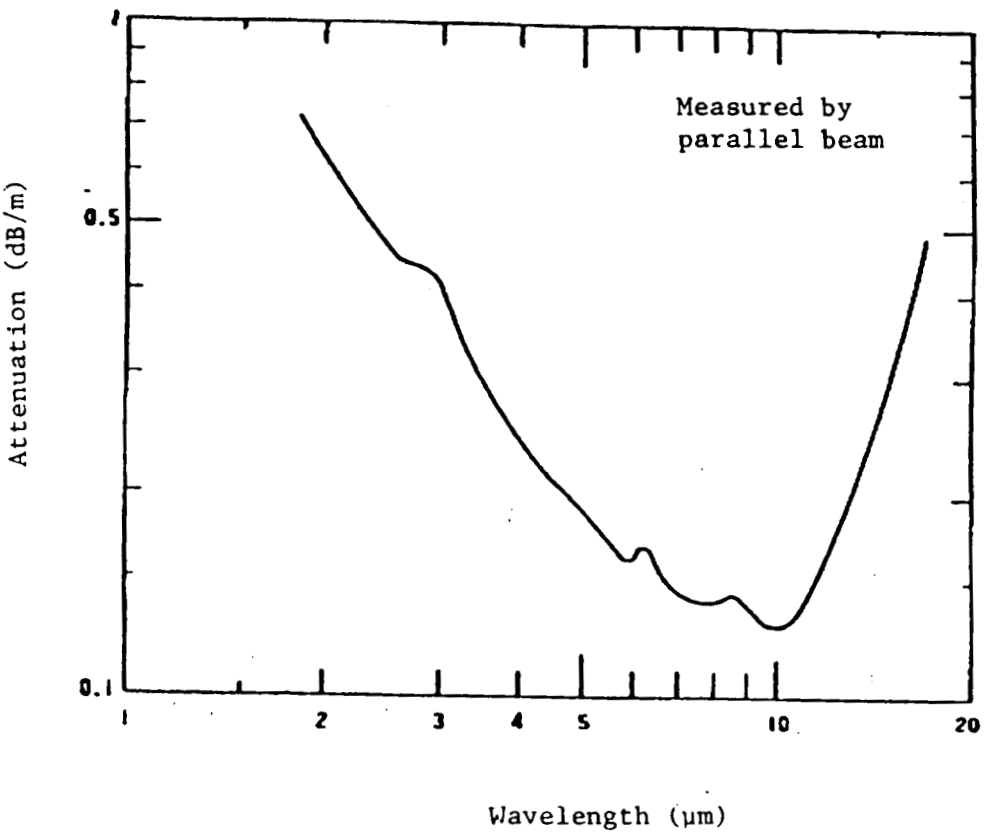

Figure 4-3. Attenuation versus wavelength of silver halide (AgCl).

Data have been provided by Asahi Glass on some of the important properties of this fiber, such as thermal effect, hygroscopicity, and bending. Figure 4-4 illustrates the transmission versus time of AgCl IR fiber at 60°C. Where Figure 4-5 shows the transmission versus time at 60°C and 90% moisture [33].

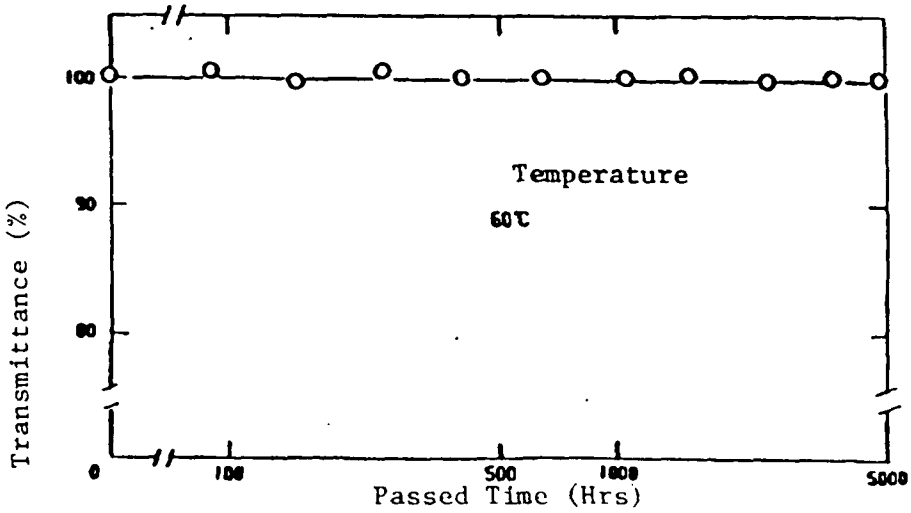

Figure 4-4. Transmission versus time at 60°C.

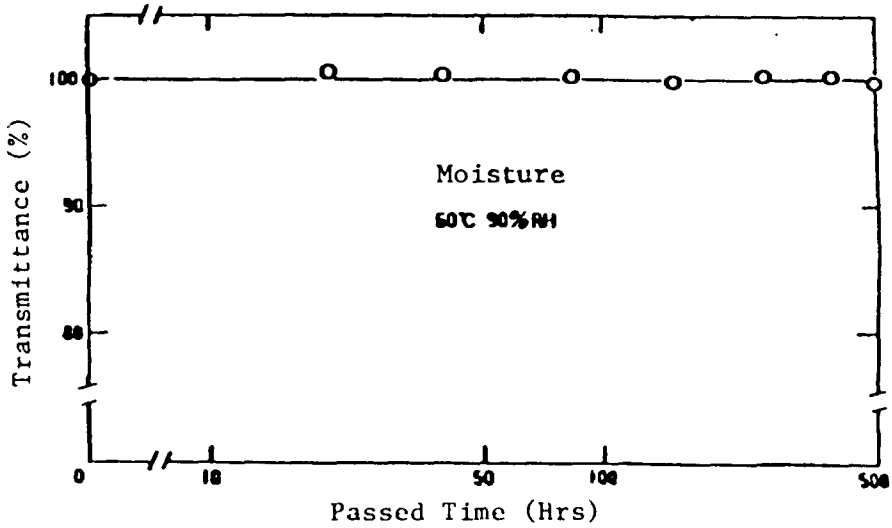

Figure 4.5. Transmission versus time at 60° and 90% moisture.

Figure 4-6 shows the transmission at various degrees of bending. Figure 4-7 illustrates the loss of transmission at various bending number [33]. This is the number of times the fiber is bent versus the corresponding loss of transmission.

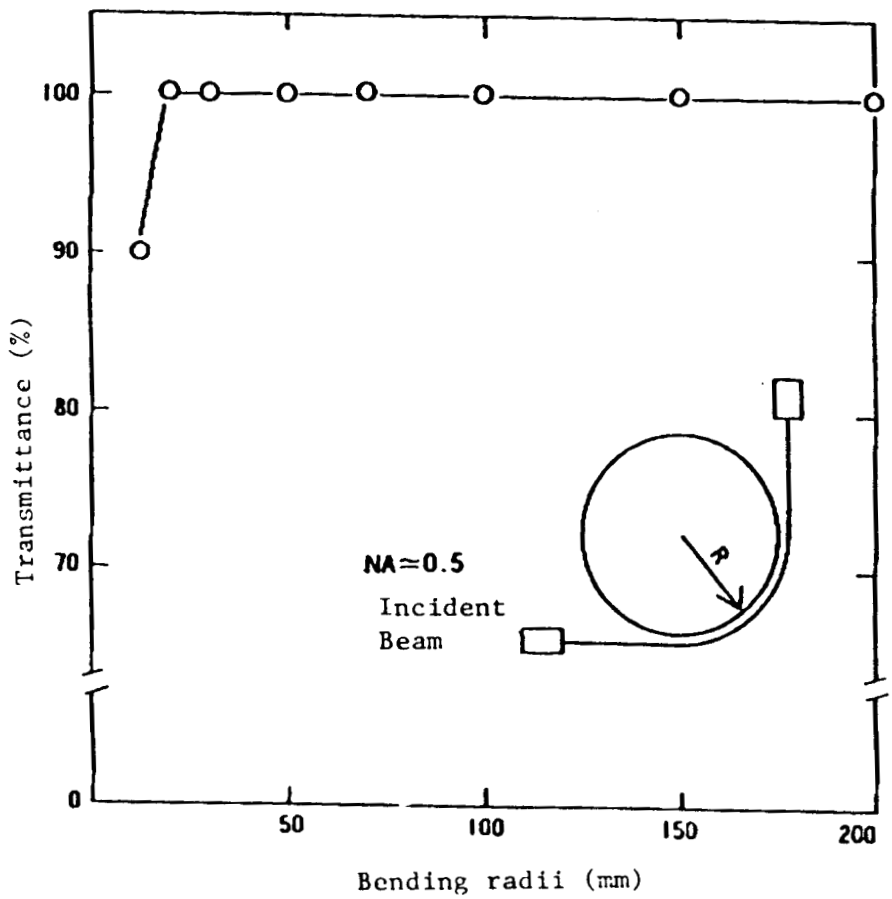

Figure 4.6. Tramsmission versus bending radii of silver halide (AgCl) fiber.

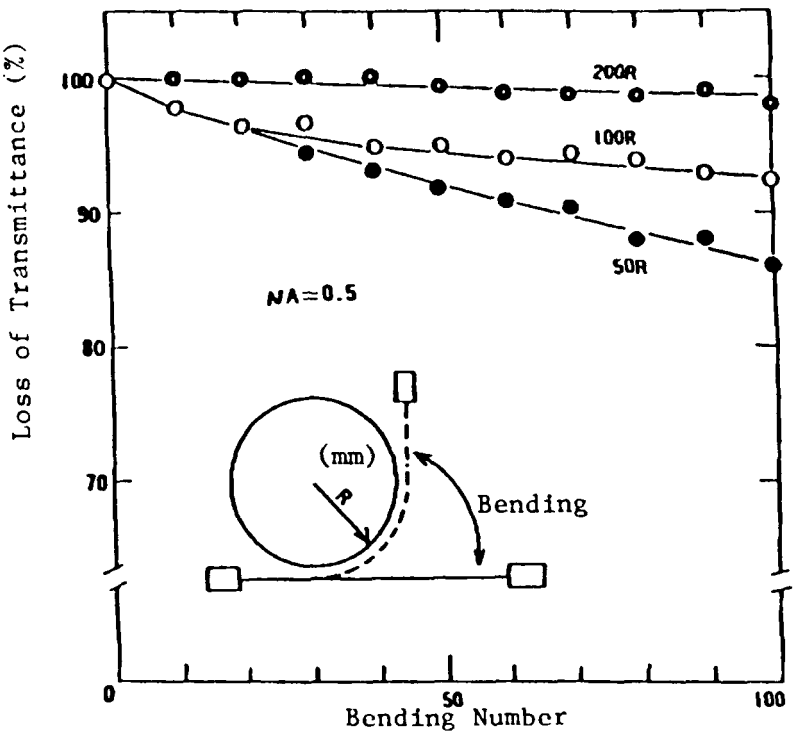

Figure 4.7. Transmission versus bending number of silver halide (AgCl) fiber.

Clad chalcogenide fiber can now be drawn from extruded rod and tube combinations. Focusing on the Ge-Sb-Se glass system, the cladding is constructed using a slight compositional modification. An effective cladding must exhibit a lower refractive index and reduced coefficient of thermal expansion while maintaining a similar viscosity for drawing. This is accomplished through precise compositional modification of the Ge-Sb-Se glass systems. Some of the typical physical properties of this fiber are listed in Table 4-9 [34]. Table 4-10 shows some of the data of Ge-Sb-Se fiber supplied to us by "Galileo Electro-Optics Corporation" [35].

The cladding establishes a new level of strength potential that can be developed through an outside compressive stress. The most popular cladding material is Teflon. This material exhibits outstanding and

Table 4-9. Physical properties of Ge-Sb-Se glass fiber.

Density	4.67 g/cm^2
Coefficient of thermal expansion	15×10^{-6} /K
Modulus of elasticity	22×10^3 N/mm^2
Knoop hardness (50 gram load)	150 kg/mm^2
Poisson's ratio	0.25
Thermal conductivity	301×10^{-3} W/m K
Refractive index @ 22°c and 10.5 μm	2.598
Lower annealing temperature (at n = $10^{14.6}$ d Pas)	240°C

Table 4-10. Data of Ge-Sb-Se chalcogenide glass optical fiber.

FEATURES:	
Material:	Chalcogenide Glass
Spectral Response:	6 micron to 11 microns
Index of Core Material:	2.6 at 10 microns
Numerical Aperture:	Greater than 0.4
Operating Temperature:	200° Centigrade (maximum)
Attenuation:	Less than 10 db/meter
CO_2 Laser Transmission:	Under investigation
Fiber Diameter:	300 microns
Core/Clad Ratio:	0.6

mechanical, chemical, and physical properties. These fibers exhibit an average tensile strength of 103×10^6 N/m^2 measured in Newton per unit area with the highest recorded tensile strength of 227×10^6 N/m^2. Strength can be strongly affected by surface conditions of the fiber.

The attenuation of present 300 μm fiber produced by Galileo Electro-Optics [35] is shown as a function of wavelength in Figure 4-8, with a range of 6-8 dB/m. Continuing development is expected to significantly lower the present losses. Because these materials possess a refractive index of 2.6, proper surface finishes are required to minimize reflection losses.

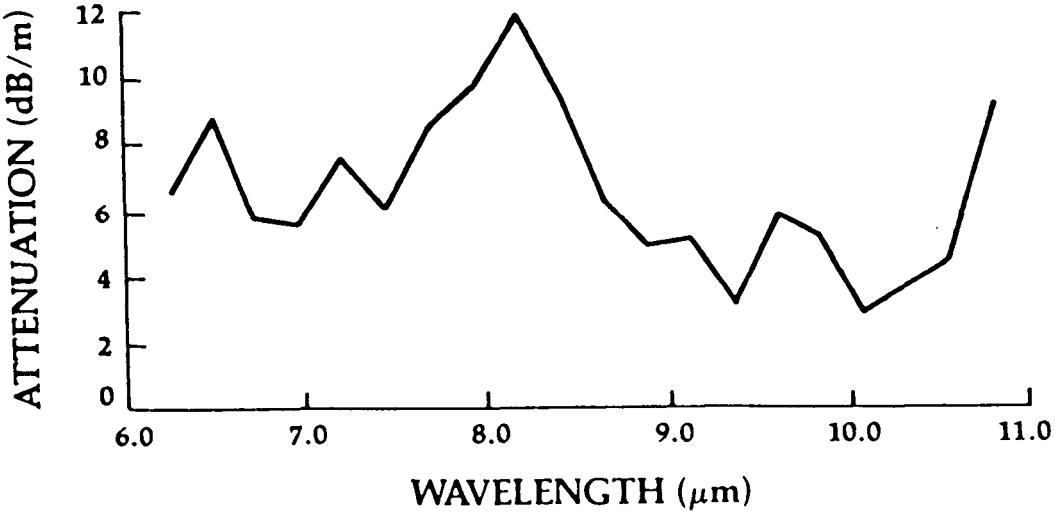

Figure 4-8. Attenuation versus wavelength of Ge-Sb-Se chalcogenide glass fiber.

Another type of IR chalcogenide glass fibers based on As-Ge-Se-Te materials have been fabricated by "Compagnie Lyonnaise de Transmissions Optiques" [36]. These fibers are suitable for transmitting optical signals in the infrared wavelength region ranging from 5.5 to 11 microns. They are particularly useful in a wide range of applications. Table 4-11 shows the characteristics of this fiber.

Table 4-11. Characteristics of As-Ge-Se-Te chalcogenide glass optical fiber.

Typical Fiber Characteristics	
Core diameter	200 μm
Outside diameter	400 μm
Core material	As Ge Se Te
Cladding material	polypropylen, PTFE
Attenuation	- Less than 2 dB/m in a large part of the range 5.5-10 μm - Between 4 and 5 dB/m at 10.6 μm (limited by the multi-phonic absorption)
Power density accepted	5 to 10 KW/cm^2
Minimum radius of curvature	1 centimeter
Temperature range	[-50°C + 125°C]
Cable Characteristics	
Cable type AM 60 (outside diameter about 3 mm)	
Unit lengths available: 1, 2, 5 meters	
Minimum radius of curvature: 5 centimeters	
Temperature range: [-50°C + 125°C]	
Maximum tensile load: 20 daN	

C-2

4.3 Procedure of Testing in our Laboratory

We have been able to obtain only a limited number of IR fibers of different material category and of less than a foot of useful length such as polycrystalline silver halide, KRS-5 and chalcogenide glass. Standard loss measurement were setup and performed on these fibers. Thermal shock, mechanical durability and flexure measurements were also made. Table 4-12 shows some of the data supplied to us along with the fiber samples by sources.

A schematic of the test setup used is shown in Figure 4-9 and the actual setup in Figure 4-10. The fiber was mounted on a fiber holder bent to avoid direct detection from the CO_2 laser radiation. The output end of the fiber was aimed at the optimum detection area of the detector. The fiber was aligned first with the CO_2 laser using low power HeNe laser as a beam splitter as alignment aid. Fiber loss measurements was based on the cut back method [37]. Since the number of fibers we had were few, and fiber length was short, all tests were performed and data gathered before the cut back technique was used.

The CO_2 laser beam was first chopped and then directed toward the entrance tip of the fiber. The transmitted radiation was detected at the exit end of the fiber, pre-amplified and then fed into an oscilloscope. Fibers were tested at LN_2 temperature by immersing them in an LN_2 bath. Fiber loss was measured before and after the immersion for the straight section and one with a 90 degree bend. The bending radius was varied by wrapping the fiber around a

cone-shaped glass flask with a narrow neck and a wide base. Its mounting on a vertical jack provided the necessary vertical motion for the flask, and thus a variable wrapping radius for the fiber.

Several unclad IR optical fibers were tested at room temperature. The transmitted signal of the CO_2 laser was detected for comparison with those transmitted through the IR fibers and considered as a reference signal is shown in Figure 4-11. The transmitted signal detected for silver halide fiber using HgCdTe IR detector is shown in Figure 4-12. The fiber length was 5 inches while the core radius was 500 microns.

The KRS-5 IR fiber of 8 inches was tested. The transmitted signal through the fiber was detected and is shown in Figure 4-13. Fiber radius was 250 μ m.

$Ge_{15}As_{10}Se_{75}$ glass fiber was tested at room temperature ($75^{o}F$). A bundle of three fibers of the same kind and equal lengths (11 inches) were used to facilitate the focusing and alignment problem. The transmitted signal through this fiber was detected and is shown in Figure 4-14. Figure 4-15 demonstrates the flexibility of a one foot $Ge_{15}As_{10}Se_{75}$ glass fiber and 4 cm bending radius. The transmission versus wavelength of this fiber is shown in Figure 4-16 [38].

As_2S_3 glass fiber was tested at room temperature ($75^{o}F$). Again a bundle of three identical fibers were used in the test to facilitate the focusing and alignment problem. The length of these fibers is 8 inches. The transmitted signal through this fiber was

detected and is shown in Figure 4-17. This fiber however is very flexible and the flexibility of it is shown in Figure 4-18 for 2 cm bending radius. The transmission versus wavelength of this fiber is shown in Figure 4-19 [38].

The transmission properties are studied for silver halide, KRS-5 and chalcogenide IR optical fibers at LN_2 temperature. The index of refraction of silver halide was 2 and for KRS-5 was 2.4. Where for both $Ge_{15}As_{10}Se_{75}$ and As_2S_3 chalcogenide glass fibers were 4.48 and 2.39, respectively. The index of refraction of liquid nitrogen was 1.2503 at $-190^{o}C$.

Silver halide (AgCl) IR optical fiber was tested at LN_2 (liquid nitrogen) temperature (77k). The transmitted signal was detected using HgCdTe detector and is shown in Figure 4-20. By comparing this result with the measurement done at room temperature (304K) shown in Figure 4-12, it is clear that the signal detected at LN_2 temperature decreased by 50% for a 5 inches long and 500 microns core radius fiber.

KRS-5 (TlBrI) IR optical fiber was also tested at LN_2 temperature (77K). The transmitted signal was detected and is shown in Figure 4-21. The transmission also decreased by 50% from that when the same fiber was tested at room temperature shown in Figure 4-13. The length of this fiber is 5 inches long while the core radius is 250 microns.

An 11 inch long $Ge_{15}As_{10}Se_{75}$ glass fiber was tested at LN_2 temperature (77K). The output signal shows a 75% transmission of this fiber, which means that the transmission decreased by 25% for

the same fiber tested at room temperature shown in Figure 4-14. The transmitted signal of this fiber at LN_2 temperature is shown in Figure 4-22.

The transmission property of AS_2S_3 IR glass fiber at LN_2 temperature (77K) was investigated. The fiber was capable of transmitting 75% which means a 25% reduction in the transmission from that when the same fiber was tested at room temperatures. The transmitted signal of this fiber at LN_2 temperature is shown in Figure 4-23.

By comparing between the detected signals of the unclad IR fibers tested at room temperature and those tested at LN_2 temperature, we notice that cleaner signals are achieved without any noise or vibration effect. This is because different fiber holder was used for the case when IR fibers were tested under LN_2 temperature. The effect of fiber holder is considered here, because fibers that are not held properly will tend to vibrate. This vibration will cause the noise noticed in some of these signals.

Data supplied by sources and some of our results are presented in Table 4-13.

The purpose of testing the metallic pipe is to compare its transmission property with those of the IR optical fiber for further applications to TDL LHS system integration.

A flexible metallic pipe was tested at room temperature ($75^{o}F$) using 10.6 microns CO_2 laser. The transmitted signal of this pipe

is shown in Figure 2-24. The hollow metallic pipe was slightly bent when tested to avoid direct exposure of laser beam to the detector. This caution is considered because the laser beam might damage the detector, since this detector is very sensitive to laser radiation.

4.4 Results

The detected signal of silver halide fiber (Figure 4-12) has shown great transmission. However, this may be due to the short length of the fiber. The signal detected has not shown noise which occurs due to vibration of the fiber.

The detected signal of KRS-5 fiber (Figure 4-13) showed a larger amplitude compared to silver halide fiber. However, KRS-5 fiber showed noise in its output signal. This is due to the vibration of the fiber and test set up. Especially since an optical table was not used. The optical table can preserve the stability of the setup.

The same fiber holder was used for testing both silver halide and KRS-5 fibers. The fiber holder was changed for testing chalcogenide glass fibers, since these fibers have smaller core diameters than both silver halide and KRS-5 fibers.

The detected signal of $Ge_{14}As_{10}Se_{75}$ glass fiber (Figure 4-14) showed a large noise. This is caused by the vibration of the fiber, since this fiber has a smaller diameter than halide fibers, it vibrates easily. Also this fiber has shown a great drop in the transmission. This is due to poor alignment and focusing of the laser source and the fiber.

In Figure 4-17 the shape of the detected signal of As_2S_3 chalcogenide glass fiber has changed. This is due to the change in modulation frequency of the chopper.

Both Figure 4-20 and 4-21 show less noise in the detected signal of silver halide and KRS-5 fibers, respectively when tested at LN_2 temperature. Because less vibration of these fibers occurred. Since proper fiber holder was used and both ends of the fiber were properly fixed, the detered signal for both fibers was dropped to 50% from that when tested at room temperature, because of the frigid temperature of LN_2.

In Figure 4-22 the detected signal of $Ge_{15}As_{10}Se_{75}$ glass fiber showed a large loss. This is due to poor alignment of the laser source and the fiber.

The shape of the detected signal of As_2S_3 chalcogenide glass fiber in Figure 4-23 was changed. Because the modulation frequency of the chopper was changed to get optimum signal of the fiber.

The detected signal of the hollow metallic pipe shown in Figure 4-24 illustrates several spikes and a large loss. This is due to poor alignment and focusing of the laser source and metallic pipe, and instable motorized translation stage used to hold the pipe in the experiment. It is clear that the signals of IR fibers are larger than that of the metallic pipe.

Table 4-12. Data supplied by sources.

Property	Fiber			
	Halide (AgCl)	KRS-5	Chalcogenide ($Ge_{15}As_{10}Se_{75}$)	Chalcogenide (As_2S_3)
Transparency (μ m)	0.6-20	--	0.9-15	0.7-10
Losses (dB/m)	5	0.4	10-16	10-16
Toxicity	No	Yes	No	No
Hygroscopicity	Yes	--	--	--
Refractive Index	--	2.4	2.48	2.39
Crystal Structure	PC	PC	--	--
Photosensitivity	Yes	No	No	No
Brittleness	No	--	Yes	Yes
Flexibility	Yes	--	--	--
Diameter (μ m)	--	500	--	--

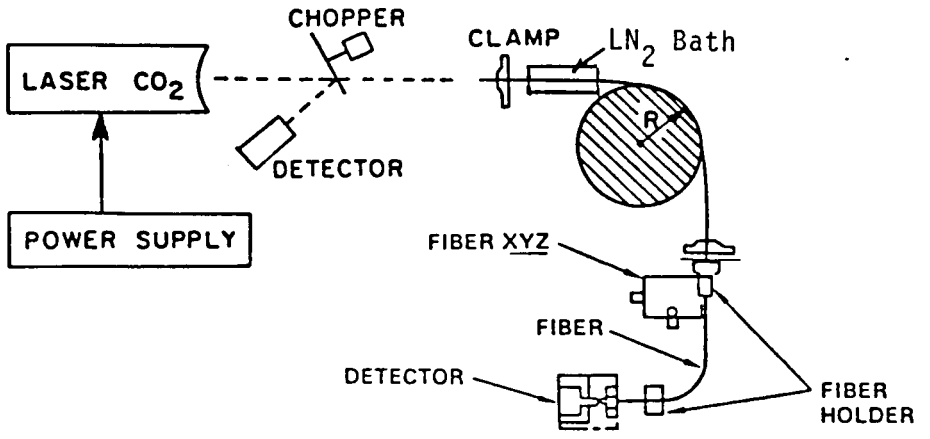

90 Degree bending

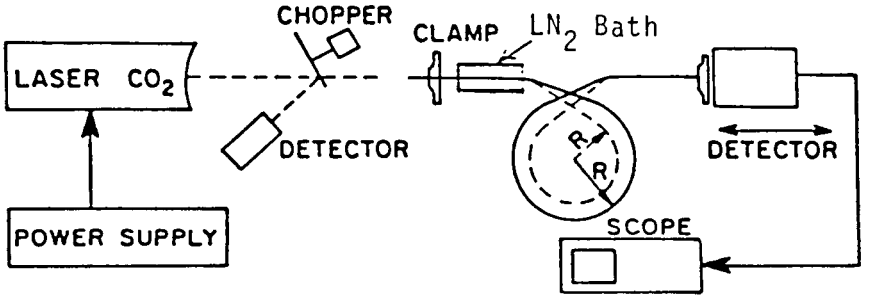

180 Degree bending

Fig. 4.9. Schematic of test setup.

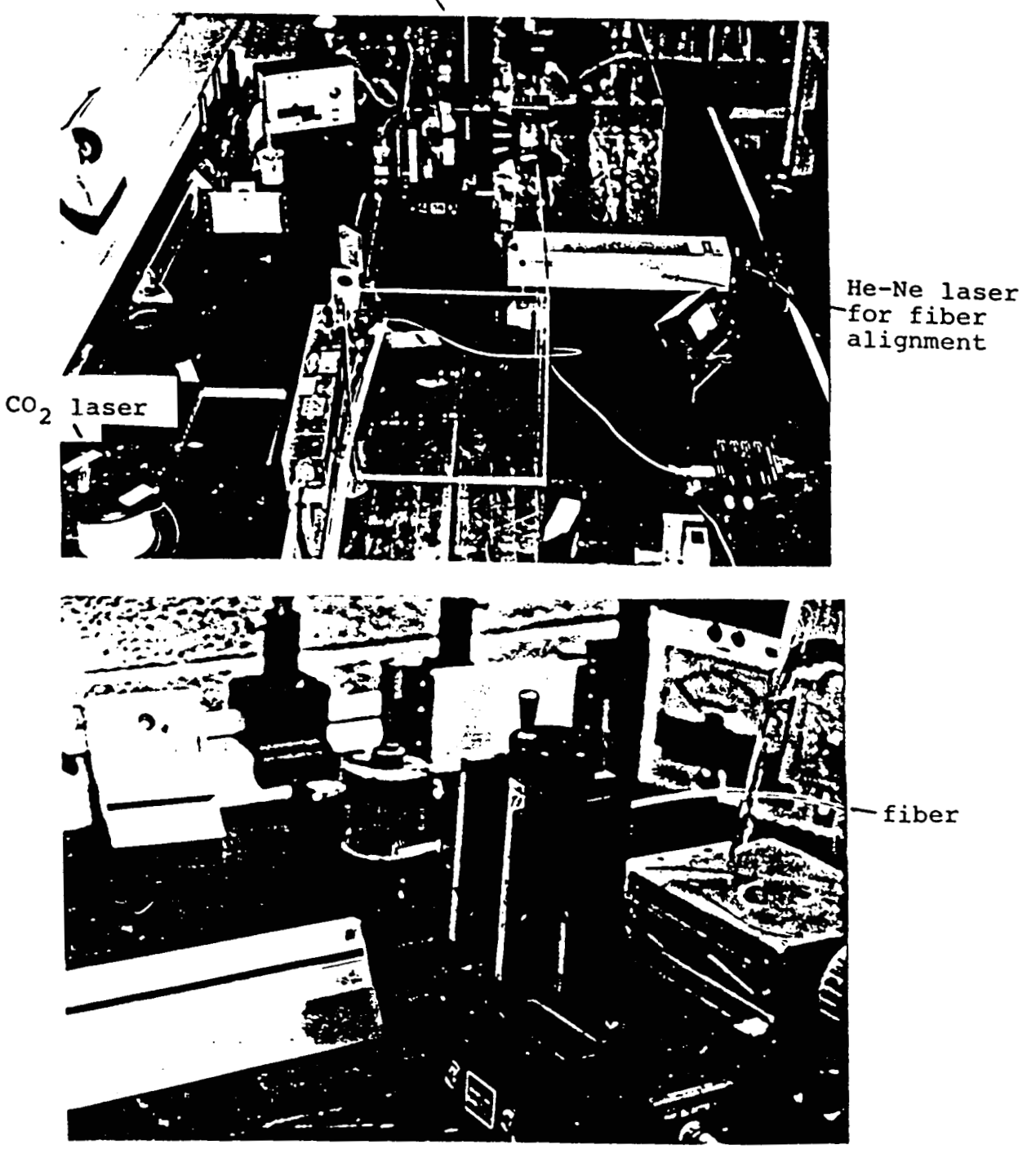

Figure 4-10. Actual test setup.

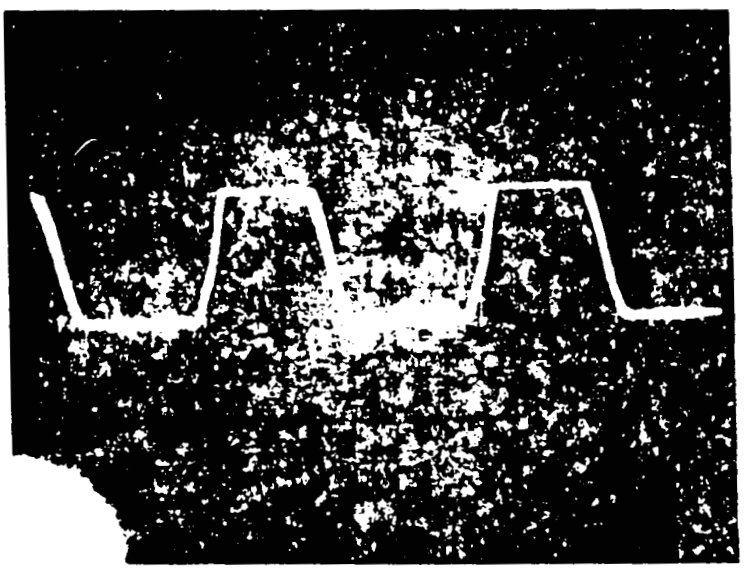

2 V/DIV

Figure 4-11. Transmitted signal of Co_2 laser.

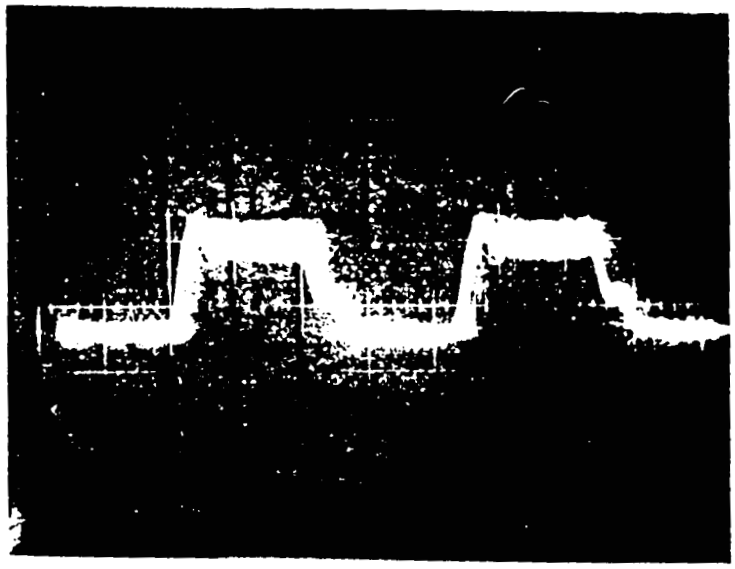

0.2 V/DIV

Figure 4-12. Transmitted signal of silver halide at room temperature (75°F.)

Figure 4-13. Transmitted signal of KRS-5 at room temperature (75°F).

0.2 V/DIV

Figure 4-14. Transmitted signal of $Ge_{15}As_{10}Se_{75}$ chalcogenide glass fiber at room temperature ($75^{o}F$).

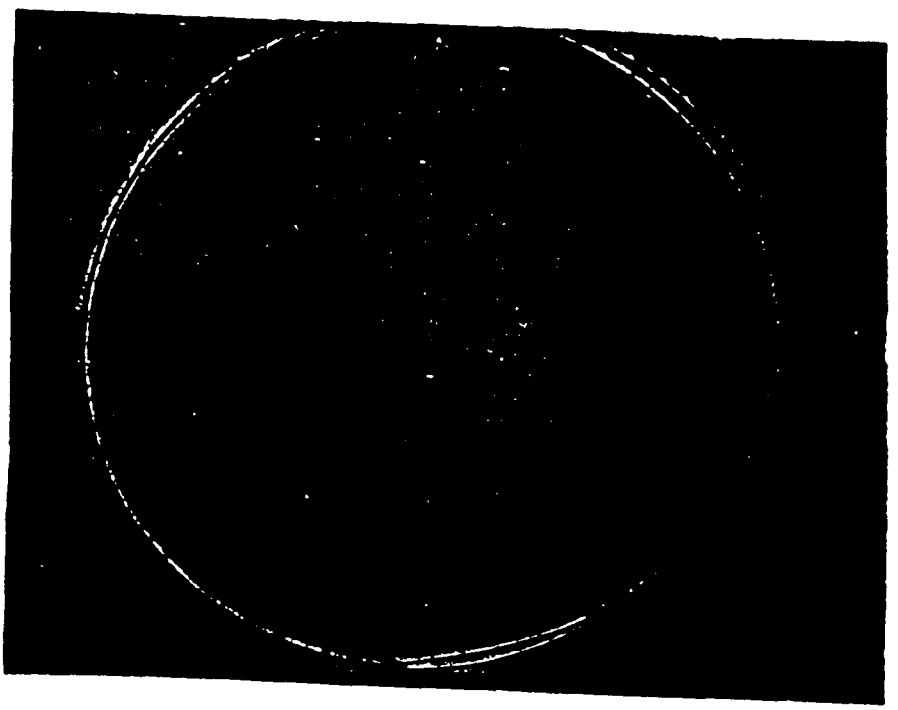

Figure 4-15. Sample of $Ge_{15}As_{10}Se_{75}$ chalcogenide glass fiber at room temperature (75°F).

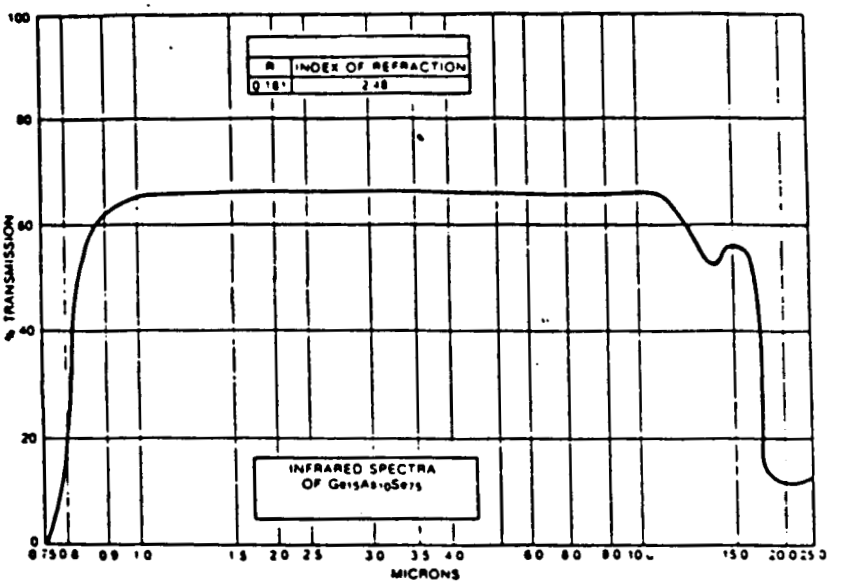

Figure 4-16. Transmission versus wavelength of $Ge_{15}As_{10}Se_{75}$ glass fiber.

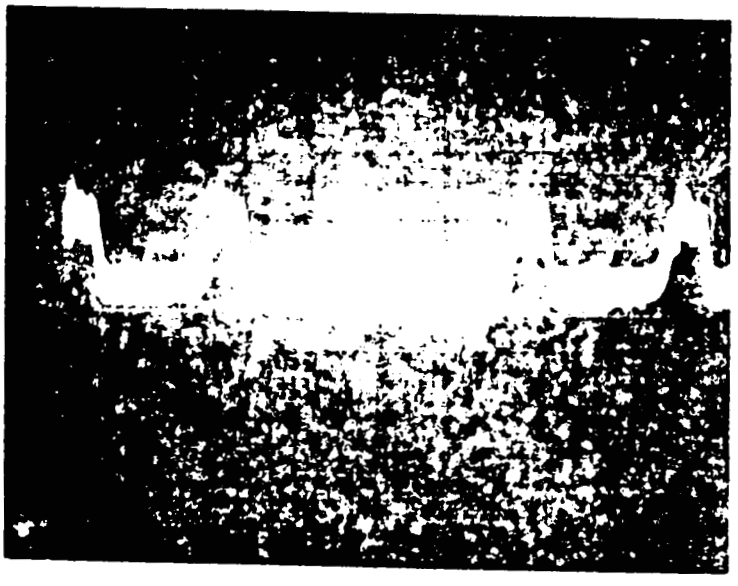

0.2 V/DIV

Figure 4-17. Transmitted signal of As_2S_3 chalcogenide glass fiber at room temperature (75°F).

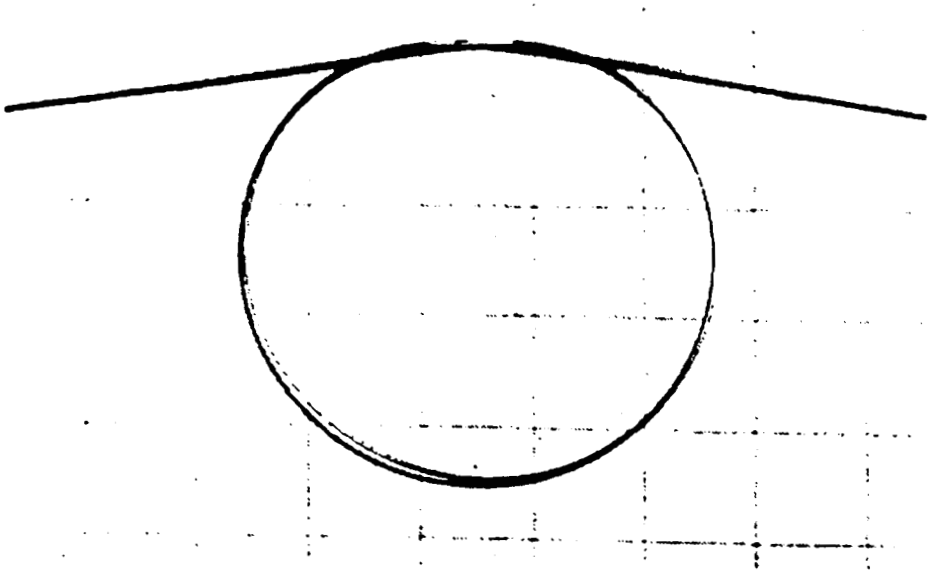

Figure 4-18. A sample of As_2S_3 chalcogenide glass fiber shows also the flexibility.

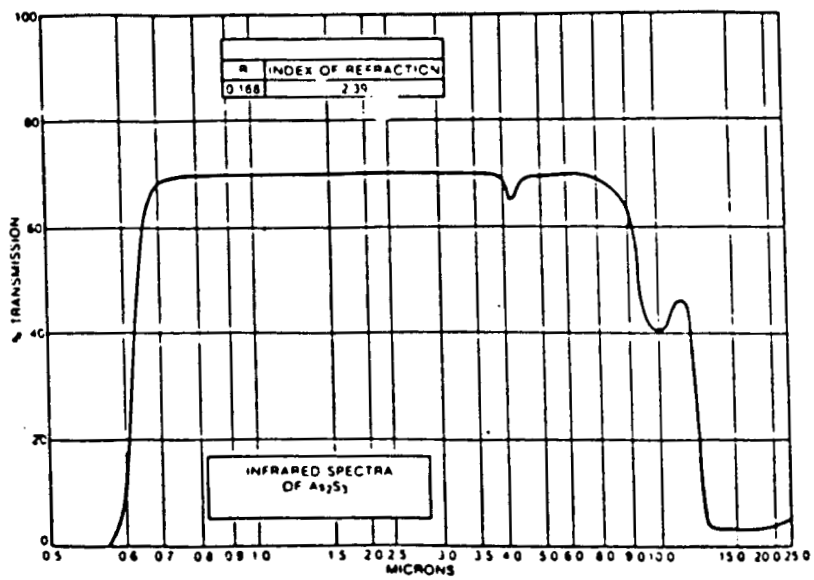

Figure 4-19. Transmission versus wavelength of As_2S_3 glass fiber.

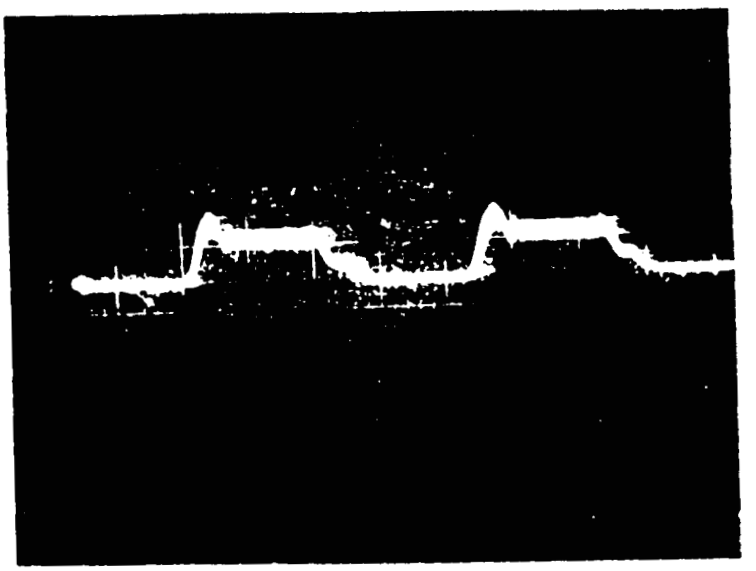

Figure 4-20. Transmitted signal of silver halide at LN_2 temperature (77 k).

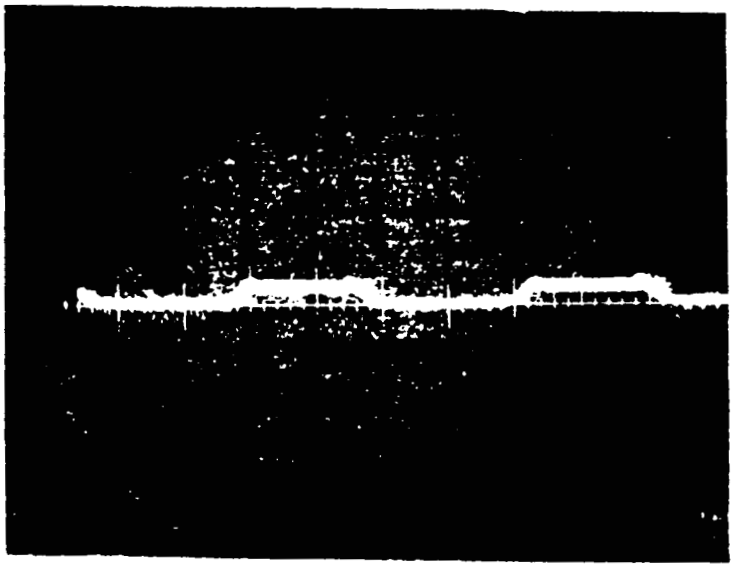

2V/DIV

Figure 4-21. Transmitted signal of KRS-5 fiber at LN_2 temperature (77 k).

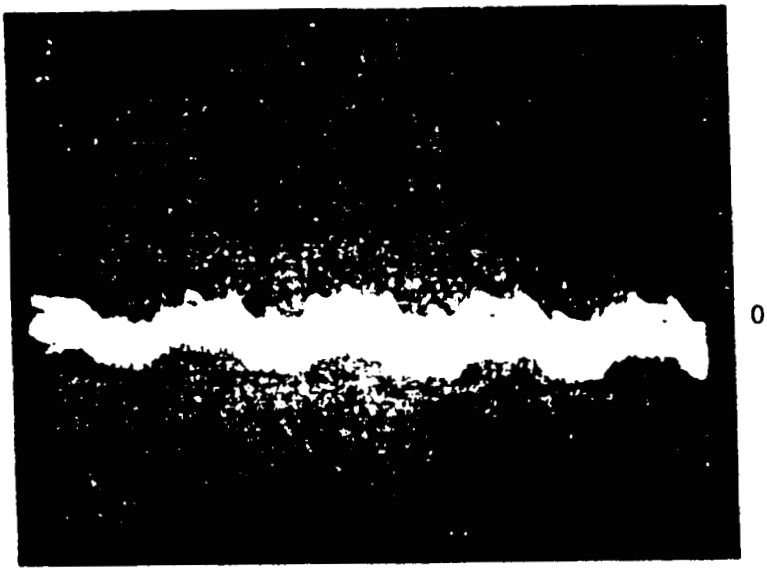

Figure 4-22. Transmitted signal of $Ge_{15}As_{10}Se_{75}$ chalcogenide glass fiber at LN_2 temperature (77 k).

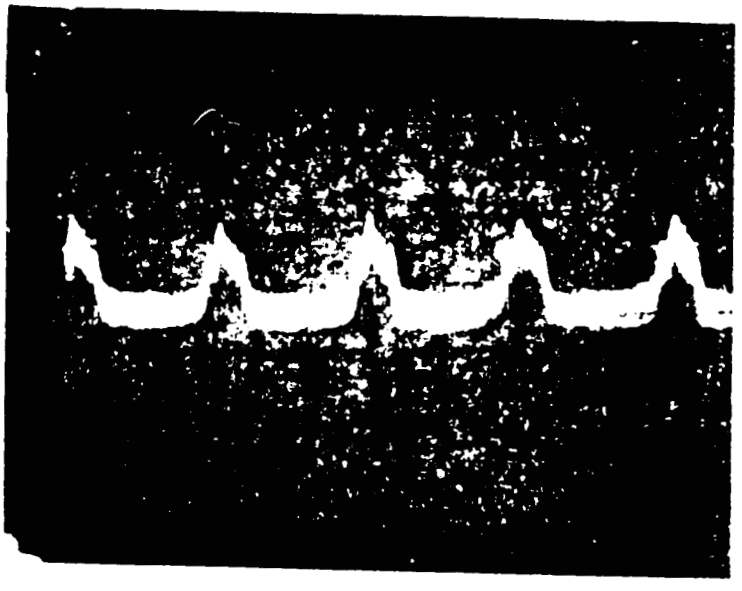

Figure 4-23. Transmitted signal of As_2S_3 chalcogenide glass fiber at LN_2 temperature (77 K).

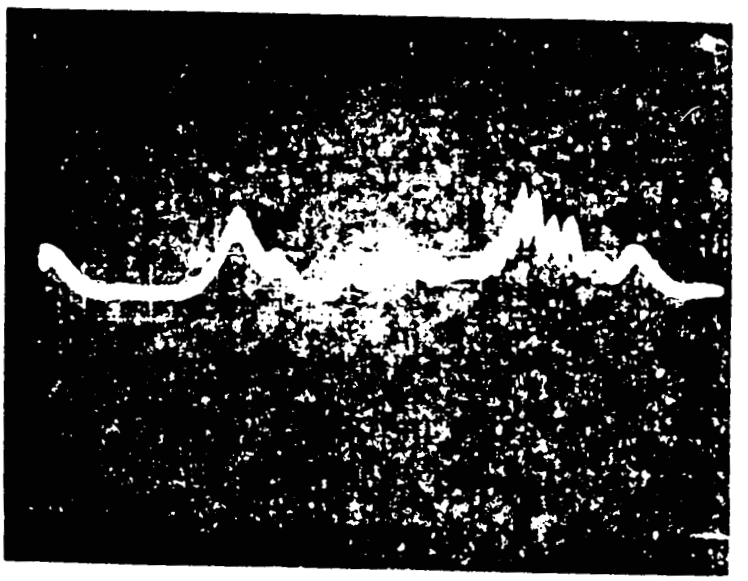

0.1 V/DIV

Figure 4-24. Transmitted signal of a hollow metallic pipe.

Table 4-13. Data supplied by sources and some of our results from measurements of IR optical fibers.

Property	IR Fiber				
	Silver Halide (AgCl)	Chalcogenide Glass KRS-5	Chalcogenide Glass ($Ge_{15}As_{10}Se_{75}$)	Chalcogenide Glass (As_2S_3)	Chalcogenide Glass * [35] ($Ge_{28}Sb_{12}Se_{60}$)
Transmission Range (μm)	0.6-20	0.2-35	0.9-15	0.7-10	5-10
Losses (dB/m)	0.7	0.12	10-16	10-16	6-8
Toxicity	No	Yes	No	No	No
Solubility (g/100)	1.5×10^{-4}	5×10^{-2}	--	5.17×10^{-5}	--
Diameter (μm)	1000	500	360	340	300
Mode	Multimode	Multimode	Multimode	Multimode	Multimode
Absorption Coefficient (cm^{-1})	9×10^{-5}	8×10^{-4}	--	--	--
Refractive Index	1.98	2.4	2.48	2.39	2.598
Tensile Strength (Kg/mm^2)	13	3.8	Good	Good	160
Hardness	2(MOH)	2-3(MOH)	171(Kg/mm)	2-3(MOH)	150(Kg/mm)
Flexibility	3 cm	No	Yes	Yes	Yes
Crystal Structure	PC	PC	Glass	Glass	Glass
Photo-sensitivity	No	No	No	No	No
Transmission at LN2 Temp.	50%	50%	75%	75%	--

* Commercial

CHAPTER FIVE

SYSTEM INTEGRATION

5.1 Introduction

A few integrated CO_2 laser systems with hollow piping and fibers have been reported and are in the market. The Laakmann hollow pipe F-75 flexible fiber delivery system is an example with a 75 cm long hollow tube of a 2 mm diameter and an 85% transmission when straight and a 60% transmission with a 90 degree bend. Obviously this size delivery system cannot provide a few-mode or single-mode transmission, highly desirable or even absolutely necessary in IR broadband and coherent communication systems.

We are in the process of fabricating a hollow pipe compatible with a rigid waveguide-package lens units for high level of adaptability to tunable diode laser (TDL) front end and HgCdTe or metal-oxide-metal (MOM) diode receiving end. An illustration of such an arrangement is shown in Figure 1-3.

This system is proposed for coupling into hollow pipes of extremely small dimension. Direct butting between TDL and fiber is assumed, unless such butting is not possible in practice. In this case, the arrangement shown in Figure 1-3 can be used for remote TDL to fiber input coupling.

The entire fiber-TDL-detector integrated system will be tested and upgraded continuously as improved fibers become available. It is anticipated in a more distant future TDL can be housed in miniature refrigerators or are free from them completely with high temperature laser diodes.

5.2 Analysis of System Integration:

The integrated system consists of a tunable diode laser mounted in a miniature hollow metallic waveguide. The cleaved coupled cavity (C^3) of the TDL is directly clamped to the coupling unit as shown in Figure 5-1. A plano-convex lens made of either ZeSe or Ge is mounted in front of a bi-convex lens such that the first lens will collimate the diverging laser beam as the second lens focuses the laser beam as shown in Figure 5.2. A third plano-concave lens is used to convert the converging laser beam into a collimated beam. The laser beam passing through the plano-concave lens is directed to the input end of the hollow metallic pipe for waveguiding. Alternatively, an IR optical fiber can be used. The output end of the waveguide illuminated some type of IR lenses that were used to guide the laser beam. The first lens is a plano-convex used to direct the diverging beam; the second lens is a bi-convex used to collect the laser beam and then focuses it into the active area of the MOM room temperature detector. This detector is also mounted in a metallic waveguide. The MOM diode package is shown in Figure 5-3.

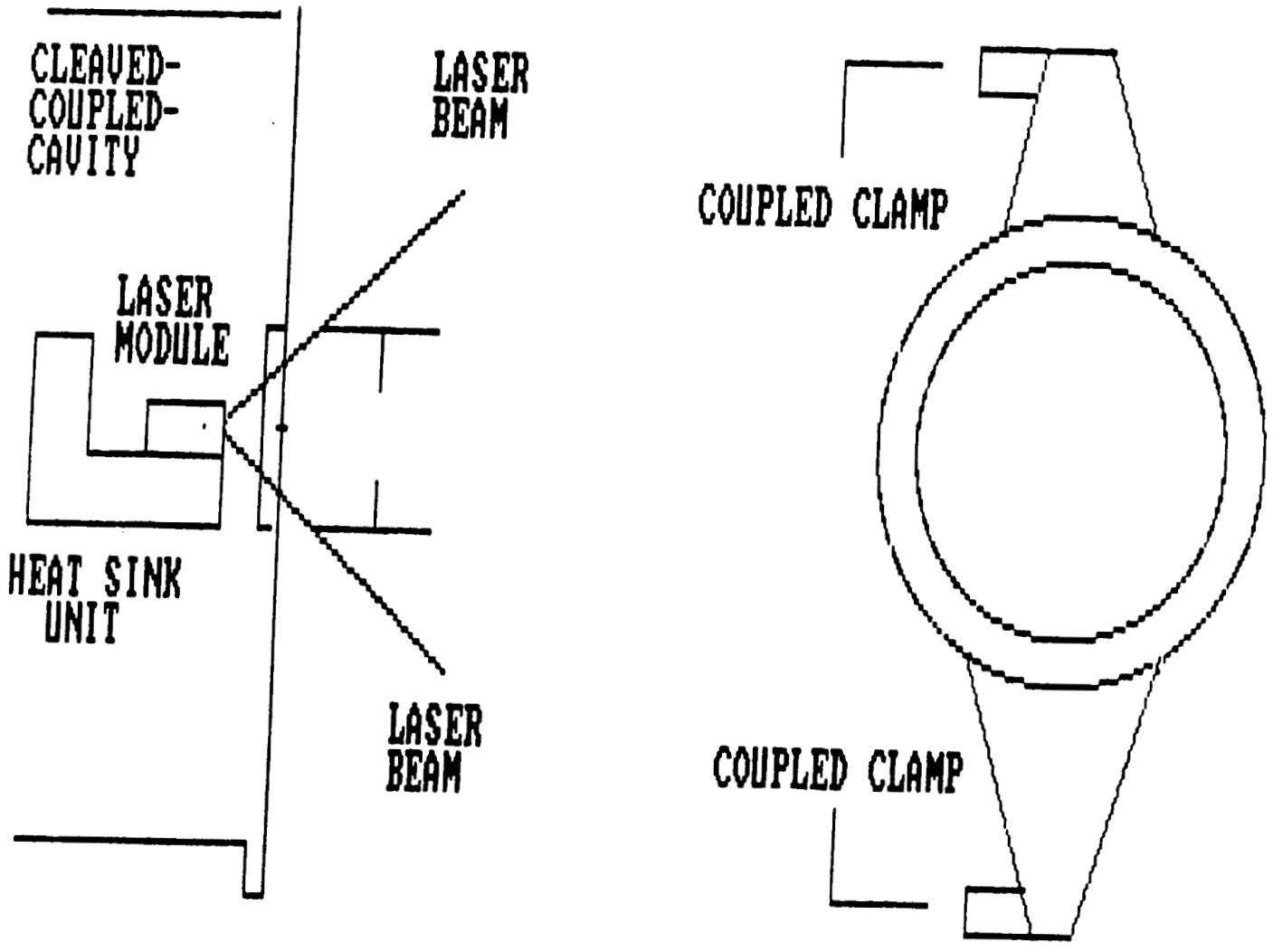

Figure 5-1. Clamping of the Cleaved Coupled Cavity of the TDL to the Coupling Unit.

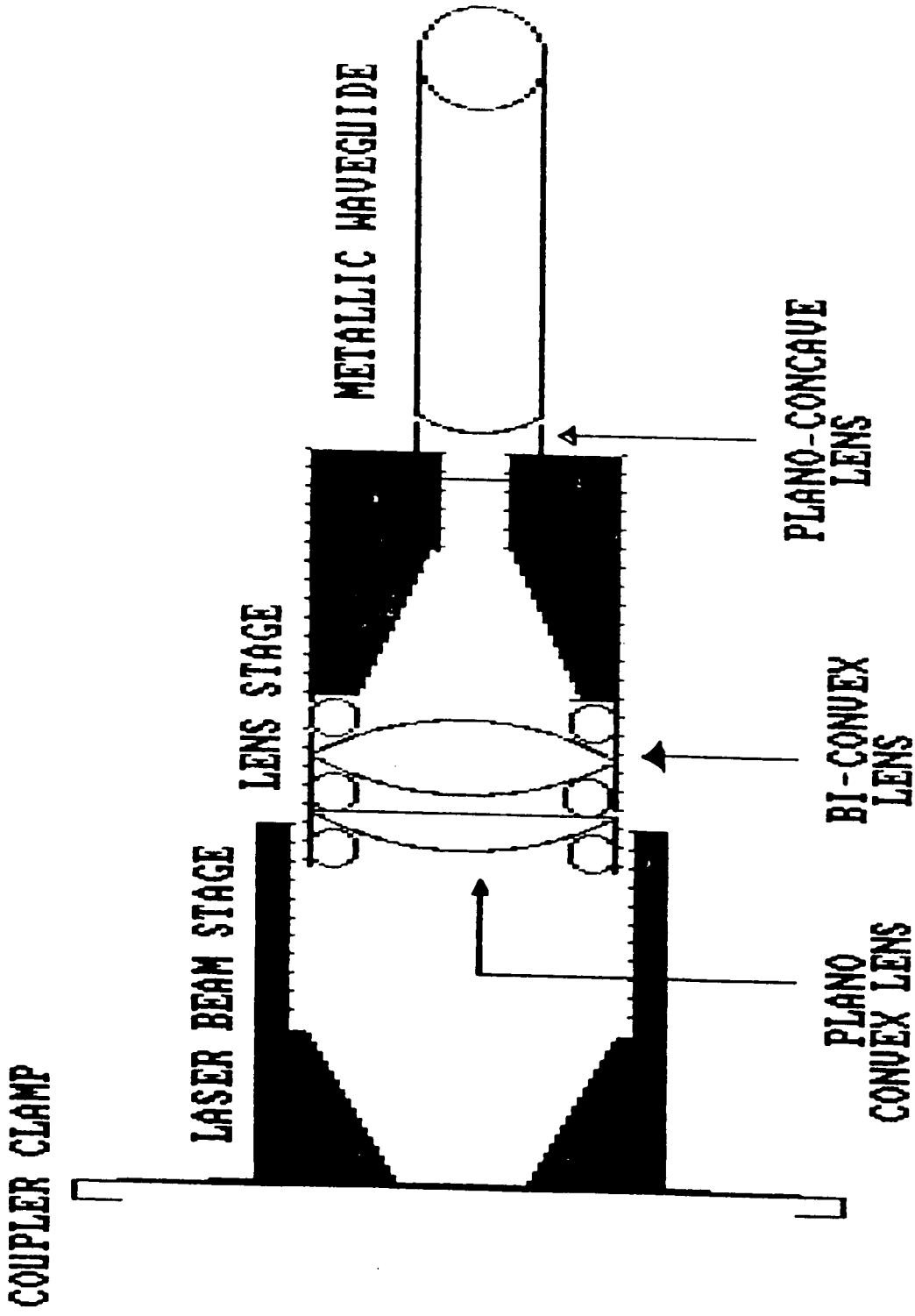

Figure 5-2. Beam Guidance by IR Lenses.

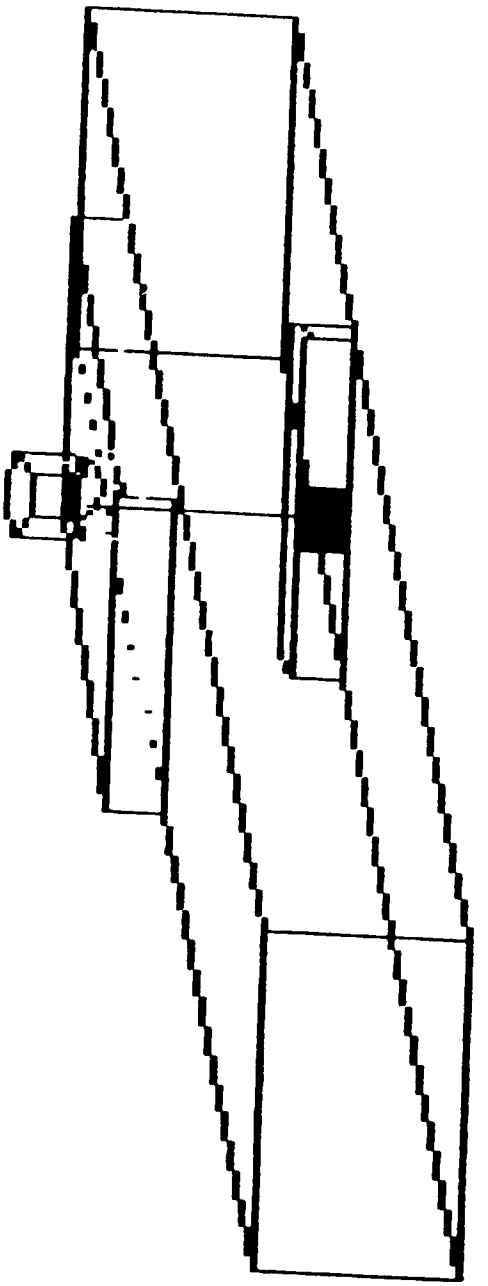

Figure 5-3. MOM Diode Packaging.

CHAPTER SIX

CONCLUSION

It has been shown that laser system integration and packaging is possible with the reduction or replacement of optical components such as lenses and mirrors by fibers (see Figure 1-3). Future system development is based on improved IR fibers and tunable diode lasers such as room temperature TDL to eliminate the required cryogenic environment, and clad IR optical fibers to reduce attenuation and number of modes.

Several types of unclad crystalline and glass optical fibers were tested both at room and LN_2 temperatures for transmission. It was noticed that the transmission of both KRS-5 and silver halide fibers had decreased by 50% when tested at LN_2 temperature from their room temperature values. The transmission of both chalcogenide glass fibers at LN_2 had been reduced by 25% from that tested at room temperature. These IR fibers are dimensionally compatible with the TDL and MOM room temperature detector.

Signal transmission detection for unclad optical fibers in our laboratory showed poor results due to the vibration of those fibers. Besides, weak signals were detected for unclad chalcogenide glass fibers possibly due to the misalignment of these fibers. Improved alignment of both the CO_2 laser and fiber and accurate equipments will result in better measurements.

Theoretical Mode analysis was performed to show the difference between weakly guiding and unclad IR optical fibers. As expected it was found that more modes propagate in the uncladded optical fibers compared to the weakly guiding fibers due to large V numbers in the unclad optical fibers. These large V numbers occur because the difference in the index of refraction of fiber core and cladding (n=1 for air) is large compared to the weakly guiding fiber ($\Delta \simeq 0.01$). Since unclad optical fibers support tremendous amount of modes, then they are not desired in communications.

Future work calls for the improvement of infrared fibers in many aspects, such as fiber fabrication process and most importantly, the suitable clading. Current IR fibers are cladded with "TEFLON." However, some fibers such as KRS-5 can be cladded with KRS-6 since the index of refraction of these compounds are closely matched. Fabricating a single mode IR fiber will be a great achievement in the field of optical communications due to their high bit rate, wide bandwidth, and ultra-low loss.

REFERENCES

1. C. Yu, "Beamshaping and polarization control properties of flexible hollow metallic rectangular pipes in the Mid infrared," Proc. IEEE, Vol. 67, pp. 965-966, 1979.

2. C. Yu and A. Niczad, "Field enhancement and increased island array selectivity of discontinuous MIM film diode," Proc. 10th Intern. Conf. on infrared and MM waves, pp. 135-136, Orlando, Florida, Dec. 1985.

3. U. Kubo and Y. Hashishin, "Flexible hollow metal light guide for medical CO_2 laser," SPIE, Vol. 494, pp. 79-83, 1984.

4. A. Katzir, "Fiber optic techniques in medicine and biology," SPIE, Vol. 576, pp. 2-7, 1985.

5. D. Gal, et al., "Silver halide fibers for surgical applications of CO_2 laser," SPIE, Vol. 494, pp. 71-75, 1984.

6. D. Gal , et al., "Reconalization of occluded arteries using CO_2 lasers and infrared optical fibers," SPIE, Vol. 576, pp. 36-38, 1985.

7. S.M. Fry, "IR fibers in medicine: Applications and specifications," SPIE, Vol. 618, pp. 40-45, 1986.

8. A.Sa'ar, F. Moser, S. Akselrod, and A. Katzir, "Infrared optical properties of polycrystalline silver halide fibers," Appl. Phys. Lett. 49 (6), pp. 305-307, Aug. 11, 1986.

9. S. Kachi, K. Nakamura, M. Kimura, and K. Shiroyama, "Reduction of the scattering loss of polycrystalline fibers," SPIE, Vol. 484, pp. 128-132, 1984.

10. G.G. Devyatykh, "Research in KRS-5 and chalcogenide glass fibers," SPIE, Vol. 484, pp. 105-109, 1984.

11. P.W. France, S.F. Carter, M.W. Moore and J.R. Williams, "Ultimate realistic losses of ZrF_4 based IR fibers," SPIE, Vol. 618, pp. 51-57, 1986.

12. H. Iwaski. "Development of IR optical fibers in Japan," SPIE, Vol. 618, pp. 2-9, 1986.

13. M.A. Pickering and R.L. Taylor, "ZnSe optical fiber for CO_2 laser medical applications," SPIE, Vol. 576, pp. 16-23, 1985.

14. M. Wehr and C. LeSergent, "Properties of Telluride based chalcogenide glass fibers for thermal infrared transmission," SPIE, Vol. 618, pp. 130-139, 1986.

15. N.J. Pitt, G.S. Sapsfore, T.V. Clapp, R. Worthington and M.G. Scott, "Telluride glass fibers for transmission in the 8-12 micrometers waveband," SPIE, Vol. 618, pp. 124-129, 1986.

16. T. Arai and M. Kikuchi, "CO laser power delivery by As2S3 IR glass fiber with Teflon cladding," SPIE, Vol. 576, pp. 24-31, 1985.

17. T. Kanamori, et al., IEEE/OSA J. lightwave technology, LT-2, pp. 607, 1984.

18. M. Saito, et al., Appl. Opt., 24, p. 2304, 1985.

19. For typical CVD ZnSe, the flexural strength and Young's modulus are 8,000 and 9.75 x 10 psi respectively. These values were used in calculating the minimum bend radius.

20. J.A. Harrington, SPIE, Vol. 266, p. 10, 1981.

21. G. Keiser, Optical Fiber Communications. McGraw-Hill, pp. 31-33, 1983.

22. H.G. Uger, Planar Optical Waveguides and Fibers Claredon Press, Oxford, pp. 313-325, 1980.

23. N.S. Kapany and J.S. Burke, Optical Waveguides Academic Press, pp. 113-117, 1972.

24. Energraphics Version 1.3 Enertronics Research, Inc., 1983, 1984.

25. M. Abramowitz and I.A. Stegun, Handbook of Mathematical Functions Dover, pp. 355-429, 1972.

26. J. Gowar, Optical Communication Systems Prentice-Hall, pp. 122-127.

27. Galileo Electro-Optics Corp., Sturbridge, Massachusets 01518.

28. Radiant Communication Corp., East Haniver, NJ 07936.

29. S. Mitachi and T. Manabe, Japan J. Appl. Phys., 19 (6), L313, 1980.

30. I.S. Lisitskii and Partners, "The mechanical properties of KRS-5 and KRS-6 single crystals," Sov. J. Opt. Technology, Vol. 43, No. 4, April 1976.

31. D.A. Pinnow et al., Appl. Phys. Lett., 33(1), p. 28, 1978.

32. D.J. Krus, D.R. Cope, "Crystal materials for infrared fibers," SPIE. Vol. 266, pp. 72-77, 1981.

33. Asahi, Japan.

34. P. Prideaux and P. White, "Infrared component design and application," Fifth Infrared Information Exchange Meeting, New Orleans, October 29-31, 1985.

35. Galileo Electro-Optics Corp., Galileo Park, Sturbridge, MA 01518.

36. Compagnie Lyonnaise De Transmissions Optiques 35, rue Jean-Jaures B.P. 20-95871, Benzons Cedex, France.

37. P. Klocek, R. Beni, J.C. O'Connell, and C.P. Van Vloten, "Measurement system for attenuation, numerical aperture (NA), dispersion, and optical time-domain reflectometry (OTDR) in infrared (IR) optical fibrs," SPIE Vol. 618, pp. 151-152, 1986.

38. J.A. Harrington, Hughes Research Labs, Malibu, CA 90265.